

**Port x-link assessment**

A portion of the X<sub>o</sub> 582 ring frame bulkhead and portside sill fitting, which has a lug that supports the port x-link, was recovered and inspected. The lug broke near its base mainly because of a bending load caused by the x-link and the forebody yawing to the left (figure 2.2-45). This yawing motion was identified by the yielding on the outboard flange of the clevis on the aft end of the port x-link (figure 2.2-46).

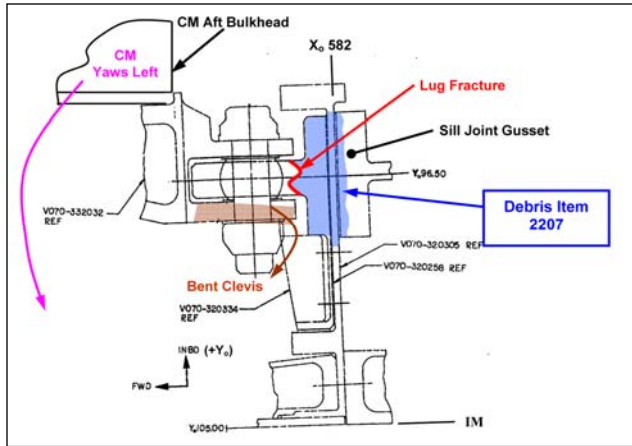


Figure 2.2-45. How the port x-link failed, cross-section view looking down.

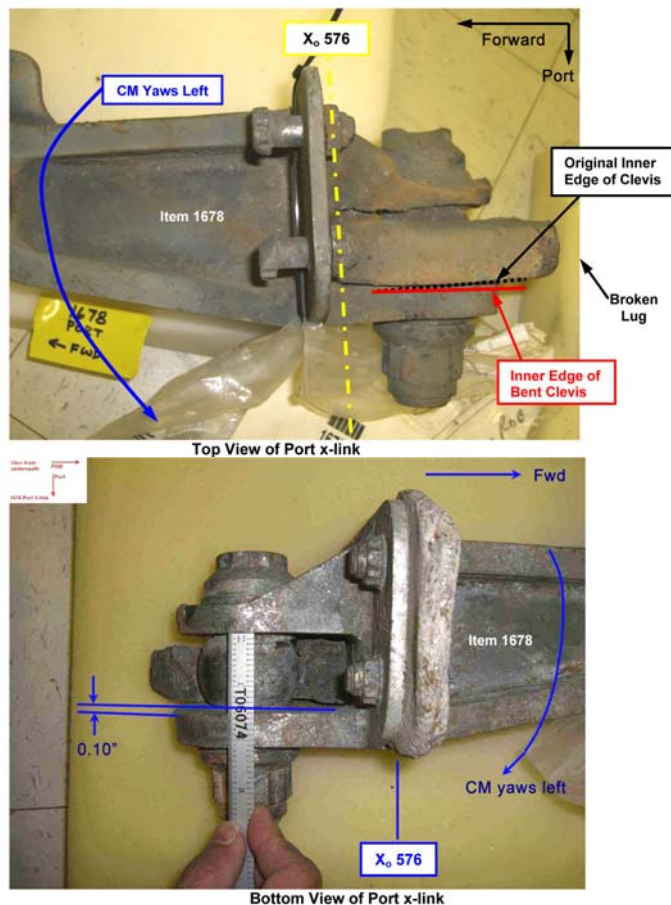


Figure 2.2-46. Views of the port x-link with about a 0.10-inch yield on the outboard side of the clevis.

As shown in figure 2.2-47, the outboard upper bolt head was gouged and deformed by an impact from the broken lug, which remained in the port x-link clevis. This indicates that the forebody not only yawed to the left but also shifted to the left when it moved away from the midbody.



**Figure 2.2-47. Columbia Reconstruction Database debris item no. 2207, which includes the remainder of the lug fitting that supports the aft end of the port x-link.**

This implies that when this lug failed, the port x-link was still attached to the CM and the lug still had the structural support of the midbody sill or a large portion of the portside midbody/sill attached. On the portside, the FF and x-link separated from the midbody sill on the *forward* side of the X<sub>o</sub> 582 ring frame bulkhead. The remaining part of the portside X<sub>o</sub> 582 ring frame bulkhead and the sill joint gusset experienced little heat erosion (figures 2.2-48 and 2.2-49). These two items were found at longitude 94.0W and 94.3W, which are in the central portion of the midbody debris field (figure 2.2-16). It is possible that they stayed with the portside midbody sill, which is one of the heaviest parts of the midbody shell. No ballistic assessment was performed to confirm or deny this theory.

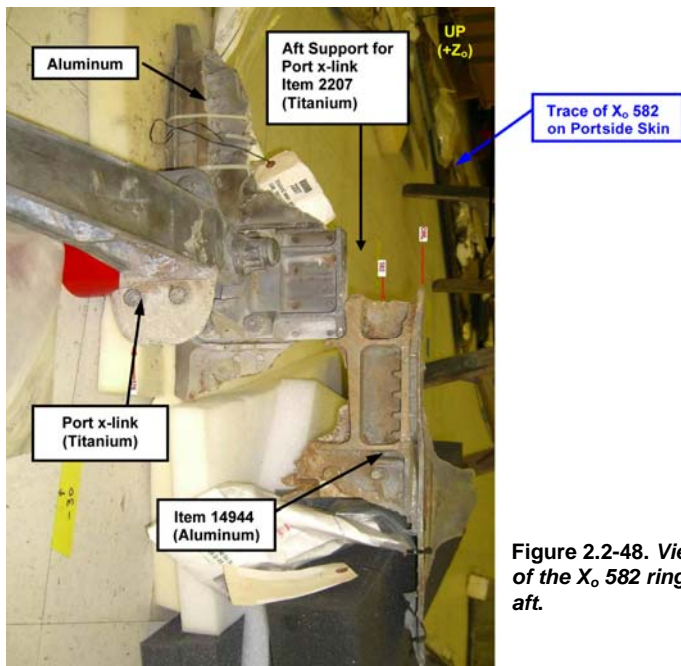


Figure 2.2-48. View of the port x-link and a portion of the X<sub>0</sub> 582 ring frame bulkhead debris items, looking aft.

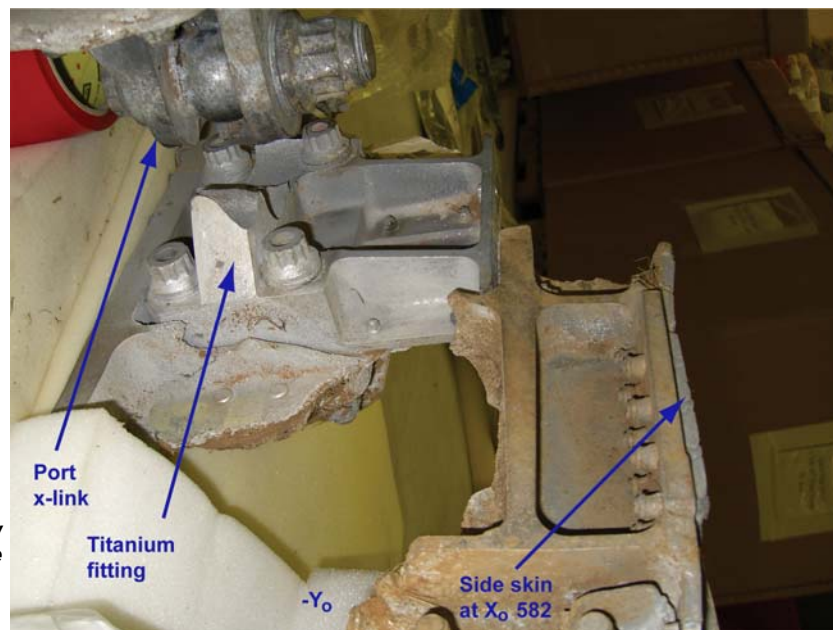


Figure 2.2-49. View looking up and aft at the port x-link.

These pieces provided a more subtle understanding of the separation event between the forebody and the midbody.

The conclusion was that the forebody separation started *aft* of the X<sub>0</sub> 582 ring frame bulkhead on the starboard-side sill area, and then spread across the fuselage along the aft portion of the X<sub>0</sub> 582 lower ring frame bulkhead. The breakup progressed toward the portside sill while the forebody yawed to the left and pitched down, causing the portside lug fitting to fail by bending to the portside. This resulted in failure at the X<sub>0</sub> 582 ring frame bulkhead on the portside of the bulkhead, leaving a portion of the bulkhead with the midbody.

Immediately after the CE, the starboard CM x-link pulled forward through the X<sub>o</sub> 582 ring frame bulkhead as soon as the CM began to move forward inside the FF shell. The CM port x-link was unsupported by midbody structure after the CE and was only attached to the CM. Interestingly, the starboard side of the *Challenger* X<sub>o</sub> 582 ring frame bulkhead also remained with the X<sub>o</sub> 576 bulkhead. However, because the breakup events had different causes, this is assumed to be a coincidence.

**Conclusion L3-2.** The breakup of both *Challenger* and *Columbia* resulted in most of the X<sub>o</sub> 582 ring frame bulkhead remaining with the crew module or forebody.

#### Tunnel adaptor

The tunnel adaptor assembly (TAA) provided the internal pressurized path for the crew to move between the middeck to the SPACEHAB in the payload bay (figure 2.2-50). The tunnel adaptor attached to the mid-deck access panel (MAP), which is a large removable panel in the X<sub>o</sub> 576 bulkhead.

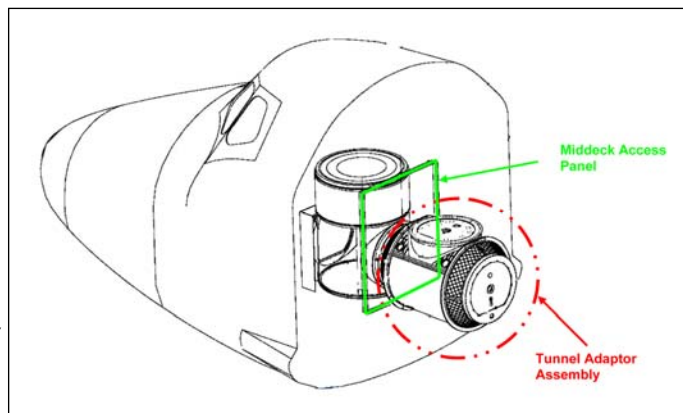


Figure 2.2-50. Tunnel adaptor assembly and middeck access panel.

One note of importance is that a breach in the TAA would cause the immediate rapid depressurization of the internal airlock, since there was no hatch between it and the TAA volume. The airlock inner hatch to the middeck was closed, so this would not result in the depressurization of the main CM, only the airlock.

Some items that were stowed in the airlock were recovered in the western portion of the debris field, prior to the main body of forebody debris. These items were either soft goods that were stowed in bags taped or strapped to the wall or floor, or bonded items (no airlock structure), which indicates that although the airlock rapidly depressurized, the structure remained intact. A headrest pad (used for ascent only) was stored in the internal airlock for entry according to the crew's entry stowage plan. Ballistic analysis was performed on this one item because of its easily described shape. This analysis determined that this item separated from the airlock/TAA compartment at GMT 14:00:36. Ballistic analysis was also performed on two small pieces of TAA structure. The release time for both pieces was computed to be GMT 14:00:43.

The debris field analysis shows that most of the TAA was recovered west of the main forebody debris field, suggesting that the TAA did not remain with the forebody but departed before the CMCE.

As shown in figures 2.2-51 through 2.2-54, the 12 high-strength bolts (180,000 pounds per square inch (psi)) that attached the forward ring of the TAA to the MAP failed with shanks still remaining in the inserts. This suggests that this area was subjected to high tension and bending while the remaining bolts were not subjected to the same loading. It implies that this TAA joint reacted to a bending moment ( $M_{TAA}$ ) plus aft tension loading (figure 2.2-54). When the aft end of the TAA was restrained by the SPACEHAB tunnel to the midbody, the forebody yawing left and pitching down relative to the midbody could create the same bending effects. This suggests that the TAA broke away from the MAP when the forebody separated from the midbody at the CE or shortly afterwards.



Figure 2.2-51. Tunnel adapter assembly and the manufacturing access panel debris, view looking forward at "B" hatch opening.

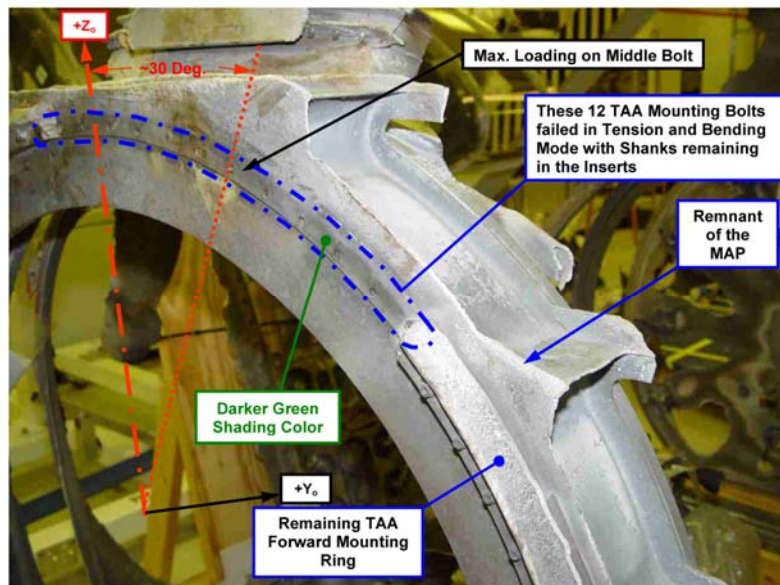


Figure 2.2-52. Tunnel adapter assembly debris showing that the bolt shanks failed mainly by tension and bending.

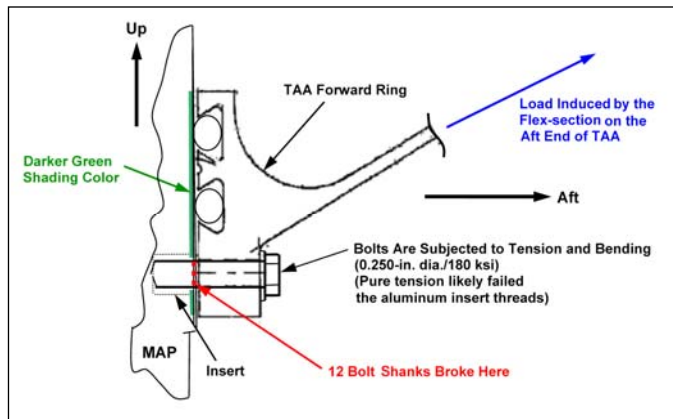


Figure 2.2-53. Cross section through tunnel adapter assembly mounting bolt.

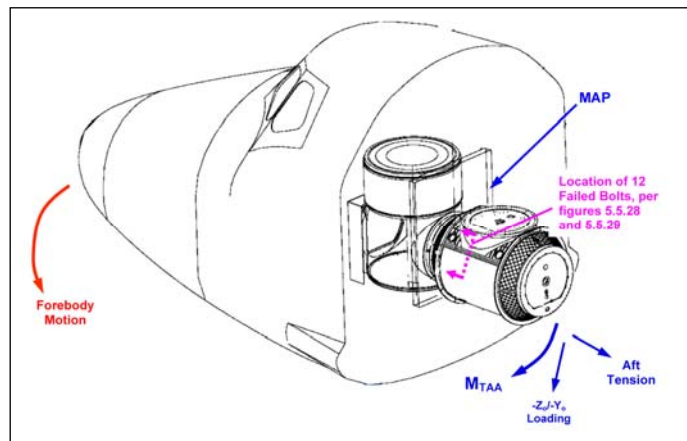


Figure 2.2-54. Predicted motion based on debris evidence.

Darker shading color on the surface of the MAP, as was noted on figures 2.2-51 and 2.2-52, indicates that this area was shielded by the missing portion of the TAA ring and suggests that the MAP surface outside of the TAA ring was subjected to thermal flow before the TAA departure. If the TAA departed at the CE, the MAP or the aft bulkhead of the CM was exposed to the thermal flow for some period of time prior to the CE (figure 2.2-44). This would agree with the theory that the PLBDs were compromised prior to the CE.

The failure of these TAA mounting bolts also indicates that it is unlikely that the X<sub>0</sub> 576 CM aft bulkhead suffered any major structural failure at the CE, although it was subjected to CM internal pressure and apparently some thermal exposure. By design, the X<sub>0</sub> 576 bulkhead can handle 24 psi of internal pressure. The TAA aft loading required to fail the TAA mounting bolts would impose less load on the X<sub>0</sub> 576 bulkhead than the maximum cabin internal pressure load case. The large mass of the bulkhead would also effectively absorb and diffuse heat.

As shown in figure 2.2-50, the MAP is a significant element of the X<sub>0</sub> 576 bulkhead. The bulkhead is linked to the flight deck floor, the middeck floor, and the two partitions on both sides of the airlock. It is not likely that the MAP would fail without causing a massive failure of the whole aft section including the X<sub>0</sub> 576 bulkhead and the airlock, affecting the floors and partitions (figure 2.2-55). This supports the conclusion that no significant damage occurred to the bulkhead at the CE.

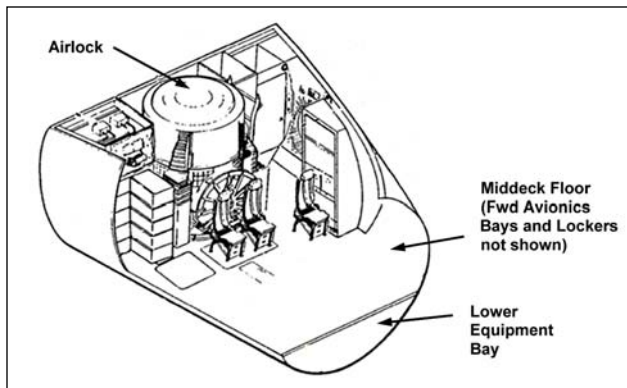


Figure 2.2-55. Airlock in the middeck.

Extreme thermal erosion at the lower edge opening on the MAP where the forward end of the TAA is attached indicates that after the TAA broke away from the MAP, hot gas flowed in over the lower edge of the “B” opening in the MAP. This thermal flow also caused heat erosion to the two aft corners of the stowage platform, which was mounted to the airlock floor (figure 2.2-56). This is consistent with the rotational motion of the forebody post-CE, when such an exposure could have occurred.

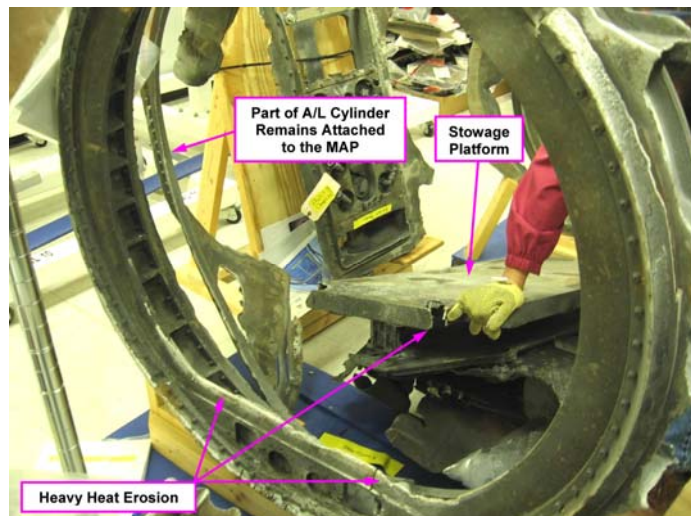


Figure 2.2-56. View looking forward at the “B” hatch opening on the X<sub>0</sub> 576 bulkhead.

## 2.2.5 Synopsis of orbiter breakup sequence

As reported by the CAIB, the left wing was gradually failing until orbiter breakup. At GMT 13:59:37, the orbiter lost control. Around GMT 13:59:49, the left OMS pod probably departed. It is possible that the PLBDs departed next or at least degraded enough to allow hot gas to flow over the starboard sill as the orbiter rotated. The orbiter then broke up at GMT 14:00:18 (CE) into aftbody, forebody, and midbody/right wing components.

It is likely that the initial failure was at the weakest area of the overall structure, just aft of the X<sub>0</sub> 582 ring frame bulkhead. This failure progressed from starboard to port by unzipping the skin splice at the X<sub>0</sub> 582 ring frame bulkhead. The forebody yawed left and pitched down, hinging at the portside x-link. This motion broke the lug fitting that supports the aft end of the port x-link, leaving the base of the lug and the local X<sub>0</sub> 582 ring frame bulkhead portside with the midbody. The aft and right wing attachments successively failed as abnormal load paths were propagated through the orbiter from the forebody separation. The next failure was the TAA, depressurizing the airlock. The forebody remained intact at orbiter breakup (see Section 2.4).

**Recommendation L3-1.** Future vehicles should incorporate a design analysis for breakup to help guide design toward the most graceful degradation of the integrated vehicle systems and structure to maximize crew survival.

## 2.3 Crew Cabin Pressure Environment Analysis

An analysis of the crew cabin pressure environment in *Columbia* was critical to formulating an understanding of what happened to the crew. This analysis was particularly important to acquiring insight into how the crew cabin environment affected the crew's ability to make decisions, at what point during the depressurization the crew's ability would have been permanently compromised, and when the crew members would have lost consciousness. To formulate this understanding, various aspects of the accident were analyzed. These included telemetry, ground-based videos, the debris, medical evidence, and structural analysis. This section draws on information described in detail in other areas of this report (structural analysis, medical findings, video analysis, etc.) to determine the timeline of the cabin depressurization. The timeline includes times for when the cabin depressurization began, when the depressurization was complete, and the rate of depressurization. Related to this analysis is determining the location(s) of the CM breach(es).

The conclusions relative to the cabin depressurization timeline are provided below:

**Conclusion L1-1.** After loss of control at GMT 13:59:37 and prior to orbiter breakup at GMT 14:00:18, the *Columbia* cabin pressure was nominal and the crew was capable of conscious actions.

**Conclusion L1-2.** The depressurization was due to relatively small cabin breaches above and below the middeck floor and was not a result of a major loss of cabin structural integrity.

**Conclusion L1-3.** The crew was exposed to a pressure altitude above 63,500 feet, indicating that the cabin depressurization event occurred above this altitude.

**Conclusion L1-5.** The depressurization incapacitated the crew members so rapidly that they were not able to lower their helmet visors.

### 2.3.1 Depressurization timeline boundaries

The depressurization timeline boundaries were identified with reconstructed telemetry and ground-based video. RGPC-2 data indicate that *Columbia*'s cabin pressure was normal (~14.7 psi) until GMT 14:00:04.826. Therefore, cabin depressurization started no earlier than (NET) GMT 14:00:05. No visual events in ground-based videos were identified positively as evidence of cabin depressurization. However, the videos show that at GMT 14:01:10, the CM image vanishes while it was still clearly in the camera's FOV. The image loss was due to the CM being broken into subcomponents that were too small and dispersed to be visible on the video. This event was defined as TD. After this time, the CM no longer had any structural integrity. Thus, cabin depressurization was complete no later than (NLT) GMT 14:01:10. This analysis establishes the absolute NET and NLT times for the start of the cabin depressurization and the completion of the depressurization. The effort to narrow these boundaries to the maximum extent possible is discussed in subsequent sections.

## 2.3.2 Start of depressurization

Medical evidence and debris field and ballistic analyses were used to determine the NET and NLT times for the beginning of the cabin depressurization.

Medical evidence suggests that the cabin pressure condition at CE was within the bounds of human survival (see Section 3.4). Therefore, the cabin depressurization started NET the CE at GMT 14:00:18.

**Conclusion L1-1.** After loss of control at GMT 13:59:37 and prior to orbiter breakup at GMT 14:00:18, the *Columbia* cabin pressure was nominal and the crew was capable of conscious actions.

Recovered objects originating from inside the CM are a positive indication of a breach in the CM. The 20 westernmost debris items originating from within the CM were evaluated.<sup>1</sup> All items were small (< 8 in.) in size and none were structural elements of the CM. The debris item located farthest west in the debris field was a piece of reflective tape from a crew helmet. Because this item was not a good candidate for ballistic analysis, the next farthest west item, a mission patch, was used for ballistic analysis. All crew members wear a mission patch attached by VELCRO® to the ACESs; virtually all other patches are stored in plastic-wrapped packages of 25 patches, which are stowed in a stowage compartment below the middeck floor called Volume E. Of the 20 debris items, nine were patches that probably originated from Volume E (Table 2.3-1).

**Table 2.3-1. Westernmost Crew Module Debris**

Item description	CM location
Launch/entry helmet reflective tape	Crew helmet
STS-107 mission patch fragment	Volume E (below middeck floor)
STS-107 mission patch fragment	Volume E
Harness or parachute webbing piece	Crew
STS-107 mission patch fragment	Volume E
STS-107 mission patch fragment	Volume E
Payload patch	Volume E
STS-107 mission patch fragment	Volume E
Payload patch	Volume E
Life raft spray shield fragment	Crew parachute pack
Panel illuminator fragments	Flight deck panel
Middeck ceiling luminous panel	Middeck ceiling
STS-107 mission patch fragment	Volume E
Air duct fragment	Middeck port
Payload checklist fragment	Middeck locker MF43K
STS-107 mission patch fragment	Volume E
Life raft reflective tape	Crew parachute pack
In-flight maintenance tool, no. 0 screw driver	Middeck locker MF43C
Sleep station closeout material	Middeck starboard
Sleep station light cover	Middeck starboard

Ballistic analysis produced a separation time of GMT 14:00:35 ± 5 seconds for the westernmost patch. Therefore, the depressurization of the CM started NLT GMT 14:00:35 ± 5 seconds.

<sup>1</sup>*Columbia* was traveling west-to-east, so debris that was recovered in the western portion of the debris field generally are items that departed from the vehicle earlier than items that were recovered farther east.

### 2.3.3 Depressurization rate

Debris items and medical evidence were analyzed in the hope that they would aid in determining the cabin depressurization *rate* and thereby aid in determining when the depressurization was complete.

Some intact packages (drink pouches and personal hygiene bottles) were recovered as was the CM cabin altimeter. Rapid depressurization tests were performed on new packages to determine the depressurization rate required to rupture these types of packages. Determining the depressurization rate sufficient to cause rupture also identifies the maximum rate that will *not* cause rupture, yielding an upper bound for the cabin depressurization rate. However, even at the maximum rate that the test chamber provided (almost 32 psi/sec<sup>2</sup>), the packages did not rupture, so an upper bound for the cabin depressurization rate could not be determined from these tests.

The recovered middeck cabin altimeter was disassembled and compared to a new cabin altimeter to determine whether the recovered altimeter contained any evidence of the cabin pressure environment. No pressure-related differences were noted between the recovered altimeter and the new altimeter. Neither the packages nor the altimeter analyses could provide any conclusions regarding depressurization rates.

Medical forensic evidence was studied to determine the rate of the cabin depressurization. Information on the effects of a rapid depressurization to vacuum is limited to postmortem analysis of isolated accidental occurrences and animal studies. A literature search revealed a case of apparent lung trauma occurring at slow depressurization rates.<sup>3</sup> Additionally, information on the fatal depressurization accident of *Soyuz 11* in 1971 revealed that although the *Soyuz 11* cabin depressurization was relatively slow (reportedly taking more than 3.5 minutes to depressurize to 0 psi), it was reported that the depressurization was fatal to the *Soyuz* crew in roughly 30 seconds.<sup>4</sup> Further research indicates that the specific circumstances (depressurization rates, the magnitude of the pressure differentials, absolute pressures, etc.) that result in the type of depressurization-related tissue damage seen in the *Soyuz 11* and *Columbia* crews have not been fully characterized. Because the exact scenario cannot be positively identified, no conclusions with respect to cabin depressurization rates or timing can be made from the medical findings.

The 51-L *Challenger* accident investigation showed that the *Challenger* CM remained intact and the crew was able to take some immediate actions after vehicle breakup, although the loads experienced were much higher as a result of the aerodynamic loads (estimated at 16 G to 21 G).<sup>5</sup> The *Challenger* crew became incapacitated quickly and could not complete activation of all breathing air systems, leading to the conclusion that an incapacitating cabin depressurization occurred.<sup>6</sup> By comparison, the *Columbia* crew experienced lower loads (~3.5 G) at the CE. The fact that none of the crew members lowered their visors<sup>7</sup> strongly suggests that the crew was incapacitated after the CE by a rapid depressurization.

Although no quantitative conclusion can be made regarding the cabin depressurization rate, it is probable that the cabin depressurization rate was high enough to incapacitate the crew in a matter of seconds.

**Conclusion L1-5.** The depressurization incapacitated the crew members so rapidly that they were not able to lower their helmet visors.

<sup>2</sup>This rate would result in a shuttle cabin depressurization in less than half a second – a scenario that is contradicted by debris and video evidence. The shuttle cabin depressurization rate was probably an order of magnitude less than 32 psi/sec.

<sup>3</sup>“Survival Following Accidental Decompression to an Altitude Greater than 74,000 Feet (22,555m).”

<sup>4</sup><http://history.nasa.gov/SP-4209/ch8-2.htm>.

<sup>5</sup>JSC 22175, STS-51L, JSC Visual Data Analysis Sub-Team Report, Appendix D9, June 1986.

<sup>6</sup>Report from Dr. Joe Kerwin to Rear Adm Truly, <http://history.nasa.gov/kerwin.html>, July 28, 1986.

<sup>7</sup>See Section 3.2, Crew Worn Equipment.

### 2.3.4 Depressurization complete

Because the depressurization rate was concluded to be high enough to incapacitate the crew within seconds, the depressurization complete NET time is some number of seconds after the earliest initiation of the depressurization, (i.e., several seconds after GMT 14:00:18). However, no direct debris evidence or analysis provided conclusive results that could refine the NET time for when the depressurization could have been completed.

Debris field analysis, ballistics analysis, and video evidence were used to provide the NLT time for when the depressurization completed. The presence of significant CM structural debris items in the debris field indicated a loss of structural integrity of the CM and, therefore, the inability to maintain cabin pressure. Ballistic analysis on a middeck floor panel indicates a release time of GMT 14:01:02 ± 5 seconds. More than 200 pieces of CM structure were recovered west of this item, strongly suggesting that the CM lost structural integrity prior to this time. Video evidence indicated that major changes in the appearance of the CM and significant debris shedding occurred from GMT 14:00:58 to GMT 14:00:59. It is probable that the CM lost structural integrity and was fully depressurized NLT GMT 14:00:59. The CM was estimated to be over 135,000 feet altitude at GMT 14:00:59, so the crew was exposed to a high-altitude environment. Figure 2.3-1 shows the depressurization timeline with the start of depressurization NET and NLT times and the NLT time for when the cabin depressurization was complete.

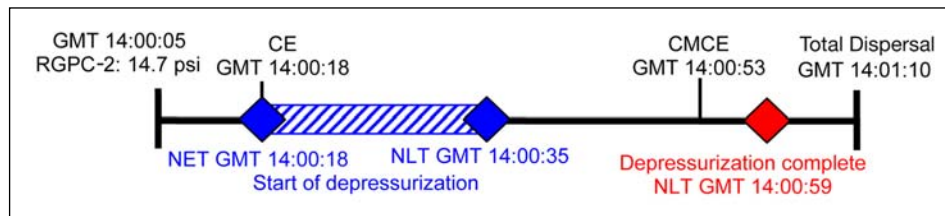


Figure 2.3-1. Cabin depressurization timeline.

**Conclusion L1-3.** The crew was exposed to a pressure altitude above 63,500 feet, indicating that the cabin depressurization event occurred above this altitude.

### 2.3.5 Location(s) of the cabin breach(es)

Structural analysis was performed to evaluate the overall loads for the CM to determine whether a structural breach occurred in the CM due to forces during the vehicle LOC. The CM was a strong pressure vessel that was designed to withstand the loads of a crash landing. Aerodynamic modeling of the vehicle provided loads for the period from LOS (GMT 13:59:32) to the CE. Deceleration loads were increasing and peaked at 3.5 G at the CE. None of the loads exceeded the CM crash loads structural limits, but CM structural deformation was possible. Impacts between the CM and the FF during and shortly after the CE likely caused damage to the CM, resulting in a depressurization.<sup>8</sup> Internal damage from the sudden load change also accounts for objects breaking free from Volume E and other stowage areas.

Depending on the size and location of breaches in the CM, a depressurization can result in differential pressures across the flight deck and middeck floors. The middeck floor had very few openings; the vent path between the middeck volume and the lower equipment bay consisted primarily of narrow gaps around the panels and access doors. Totalling all the gaps, this venting area was approximately 50 in<sup>2</sup>. The middeck floor structure could withstand a differential pressure of 0.32 psi without suffering deformation.<sup>9</sup> A cabin depressurization computer model was used to determine the maximum hole sizes that would exceed the

<sup>8</sup>See Section 2.4, Forebody Breakup Sequence.

<sup>9</sup>Rockwell internal letter SAS/AERO/88-469.

capability of the floor.<sup>10</sup> This model predicted that a hole larger than 12.4 in. diameter (or several smaller holes equivalent to 12.4 in.) *above* the middeck floor, or a hole larger than 4.8 in. in diameter *below* the middeck floor would result in a differential pressure across the floor greater than 0.32 psi (figures 2.3-2 and 2.3-3).

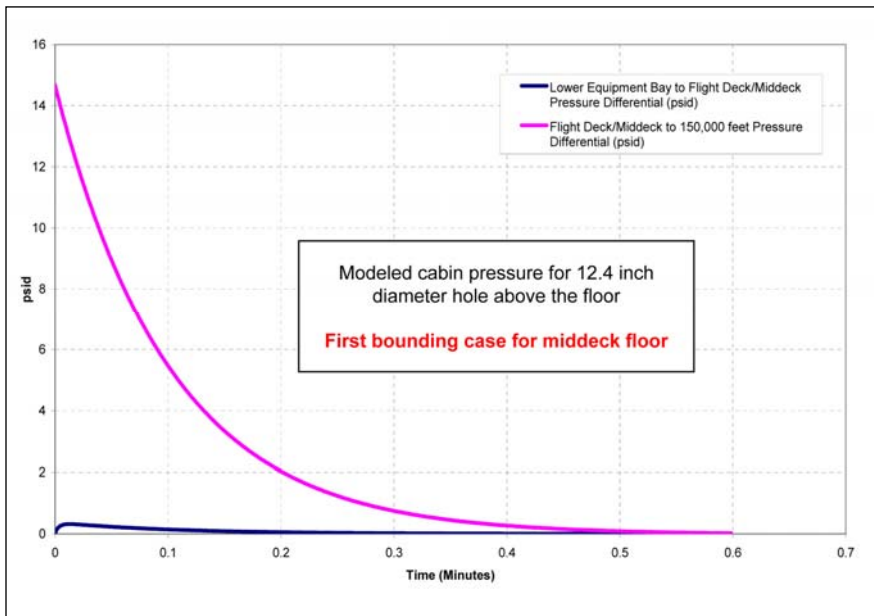


**Figure 2.3-2. Plot from a cabin depressurization model showing a 12.4-inch-diameter hole above the middeck floor. The maximum differential pressure across the middeck floor is 0.317 pounds per square inch (within middeck floor capability).**

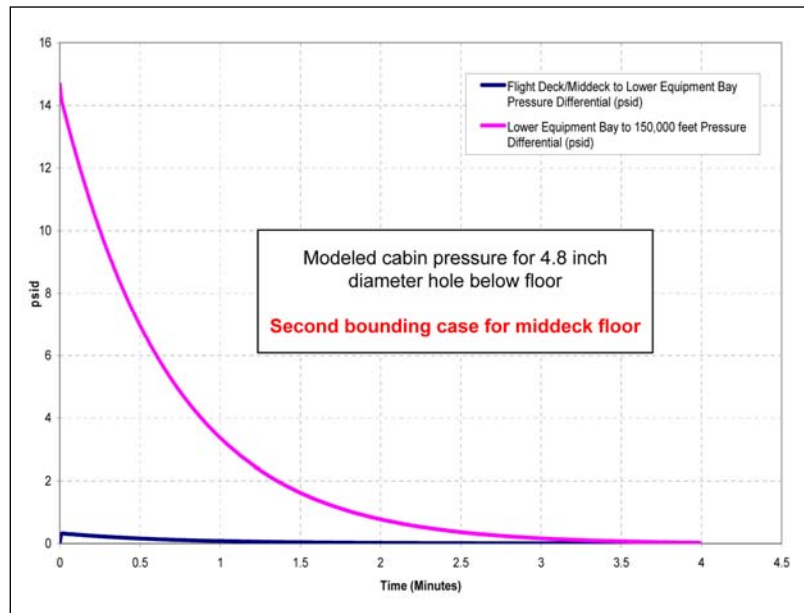


**Figure 2.3-3. Plot from a cabin depressurization model showing a 4.8-inch-diameter hole below the middeck floor. The maximum differential pressure across the middeck floor is 0.319 pounds per square inch (within middeck floor capability).**

<sup>10</sup>The shuttle life support system includes emergency regulators that can maintain the cabin pressure at 8 psi in the event of a cabin breach. The combined maximum flow rate for the system is less than 200 lbs./hour. Cabin breaches discussed in this report were much larger (> 50,000 lbs./hour) and would have overwhelmed the system. Additionally, because the O<sub>2</sub> and N<sub>2</sub> supply tanks were separated from the forebody at the CE, the cabin depressurization analysis presented here does not include gas introduction from the emergency system.

More than 65% of the middeck floor was recovered, and there was no evidence of buckling due to differential pressure. This indicates that the CM depressurization rate did not exceed the structural capability of the middeck floor.<sup>11</sup> Therefore, the cabin depressurization was not caused by an instantaneous hole above the middeck floor larger than 12.4 in. diameter (or several holes, all above the middeck floor, with a combined effective hole size of 12.4 in. diameter). Additionally, the depressurization was not due to an instantaneous hole (or several holes combined) below the middeck floor larger than 4.8 in. diameter. However, holes on both sides of the floor could cause cabin depressurization to occur more quickly and still not cause differential pressures sufficient to damage the floor. The analyses assumed that the hole sizes remained constant; if the holes were to enlarge gradually, a depressurization could occur faster without exceeding the middeck floor's 0.32 pounds per square inch differential (psid) capability.

Based on the fact that the westernmost CM debris field contained items originating from stowage volumes below the middeck floor and from areas above the middeck floor, and the lack of evidence of floor deformation, it is probable that the cabin breach involved holes above and below the middeck floor. The small size of the items and the distinct lack of CM shell structure or elements of heavy internal structure suggest that the individual breaches were not large.

The CE was the most probable time at which a structural failure would occur that would result in structural warping of the CM and/or CM/FF impacts, resulting in one or more breach locations. This is consistent with the previous conclusion that the crew was conscious at the time of the CE (GMT 14:00:18).

**Conclusion L1-2.** The depressurization was due to relatively small cabin breaches above and below the middeck floor and was not a result of a major loss of cabin structural integrity.

### 2.3.6 Synopsis of crew cabin pressure environment analysis

Prior to the CE (GMT 14:00:18), the *Columbia* cabin pressure was nominal and the crew was capable of conscious actions. The CM depressurization began NET GMT 14:00:18 and NLT GMT 14:00:35, and was due to cabin breaches above and below the middeck floor. The depressurization rate was high enough to incapacitate the crew members within seconds such that they were unable to perform actions. Although the CM lost structural integrity and was fully depressurized no later than GMT 14:00:59, it is highly probable that the depressurization was complete earlier.

---

<sup>11</sup>The flight deck floor can be damaged by a differential pressure greater than 0.81 psi. Due to the much larger venting area between the flight deck and the middeck, holes much larger than 12.4 in. diameter would be required to deform the flight deck floor. Very little flight deck floor debris was recovered, so no conclusions regarding the deformation of the flight deck floor could be made.

## 2.4 Forebody Breakup Sequence

This section discusses the breakup of the forebody of *Columbia*. The findings in this section are based on ground-based video analysis, ballistic calculations, cluster analysis of the debris field, and structural analysis.

The format of this section follows the format of Section 2.2, Orbiter Breakup Sequence. *It is strongly recommended that the reader review Section 2.2 before reading this section.* Complete descriptions of the types of analysis can be found in the introduction of Section 2.2 and are not repeated here.

Based on video, the forebody broke away from the intact orbiter at the CE, GMT 14:00:18. Because the forebody's ballistic number was significantly higher than that of the intact orbiter (more dense, with less drag), at the moment of separation the deceleration due to drag decreased suddenly. The loads experienced by the forebody dropped from the peak load of approximately 3.5 G just before the CE to approximately 1 G after the CE. As the forebody began its own unique ballistic trajectory, deceleration forces began to build again. Additionally, the forebody was rotating in all axes at approximately 0.1 rev/sec with an increasing rate (see Section 2.1).

The forebody breakup was initiated at the CMCE at GMT 14:00:53. This was the beginning of a sequence of events resulting in the dispersal of the forebody into multiple smaller components. NLT GMT 14:01:10, the CM had lost all structural integrity and had been broken into subcomponents. This time was defined as the TD.

The following findings and recommendation are in this section:

**Finding.** The *Columbia* windows remained largely intact up until the CMCE and were not a cause of cabin depressurization.

**Finding.** Windows 7 and 8 experienced a titanium deposition event that occurred prior to window breakup.

**Finding.** The most probable source for the titanium deposition on Windows 7 and 8 was PLBD rollers. These rollers were not exposed to heat flow until after the PLBDs were compromised.

**Finding.** All the windows had an aluminum-rich deposition, which was consistent with a turbulent process.

**Recommendation L3-1.** Future vehicles should incorporate a design analysis for breakup to help guide design toward the most graceful degradation of the integrated vehicle systems and structure to maximize crew survival.

## 2.4.1 Ground-based video analysis

This section addresses the detailed analysis of ground-based video related to the forebody after separation from the orbiter at the CE. This section only covers major events seen in the video that occur relative to the forebody breakup, including the CMCE and the TD.

A video triangulation analysis on the motion of the free-flying forebody was discussed in Section 2.1. A different relative motion analysis related to the TD is discussed here.

### Catastrophic Event to Crew Module Catastrophic Event

It was initially anticipated that the CM depressurization could be identified in videos as a halo or other visible effect. However, detailed review of the video showed a visually complex event at the CE. The forebody was not visually distinct from the rest of the orbiter's pieces until about 8 seconds after it separated from the intact orbiter. It is unknown whether a depressurization event would be visible; but if it was and it occurred during this time, any indication of the event would be lost in the merged signals of the orbiter's pieces. None of the changes in appearance at the CE or afterward could be positively identified as a depressurization event (see Section 2.3).

### Crew Module Catastrophic Event

Video analysis established the precise time for the CMCE (the initiation of the breakup of the forebody) as GMT 14:00:53. Thermal and ballistics analyses of forebody debris items were consistent with this, supporting the video-based time.

At the CMCE, the video shows that the forebody began to visibly brighten and the envelope of gases around the forebody appear to increase in size. This brightening event was followed quickly by a significant debris shedding event that was likely to be the FF and the CM separating from one another.

Figure 2.4-1 shows a set of five paired images covering less than 2 seconds of time. On the left is the original image and on the right is a close-up of the forebody and CM. The first frame shows when the forebody begins to brighten. The second frame, which was taken one-third of a second later, shows the slight increase in apparent size of the envelope of gases of the orbiter. The third image, almost 1 second later than the previous image, shows the first definitive indication (although it can be recognized a few frames earlier) that the forebody is beginning to fail. The magnified image has been inverted to emphasize the split in the trail of the forebody. The next frame, which occurs about one-third of a second later, shows what are believed to be two significant portions of the FF separating from the CM. The last image, taken one-fifth of a second later, shows how quickly the FF is breaking into pieces that are too small to be seen by the camera. The CM breaks up over the next 16 seconds.

### Total Dispersal

As objects separated from each other during the breakup, each took on its own trajectory based on its unique ballistic number. The high initial speed immediately resulted in a wide dispersion of trajectories as lighter and smaller items decelerated very rapidly, while heavier and larger items decelerated less and, hence, traveled farther. Evaluation of the debris appearance confirmed that very little debris-to-debris interaction (impacts) occurred. As subcomponents decelerated, the entry heating began to decrease quickly, resulting in a loss of visual signal in the video. The CM image vanishes while it was still clearly in the camera's FOV. The image loss was not due to a major deceleration taking the intact CM out of the frame, but was due to the CM being broken into subcomponents that were too small and dispersed to be visible on the video. This event was described as the TD. After this time, the CM no longer had any structural integrity.

It should be noted that cascading structural failures were still occurring following the TD, as well as frictional heating on individual objects with high ballistic numbers that decelerated more slowly. These ongoing failures could not be seen on video.



Figure 2.4-1. Five time-paired images covering under 2 seconds of time showing the Crew Module Catastrophic Event. Image on the left is the full frame, image on the right is an enlarged view.

Figure 2.4-2 shows the last few seconds of the CM as seen in the Apache video, ranging from GMT 14:01:06 through GMT 14:01:09. The images on the right side are a magnified view of the original images on the left. The CM has been circled in red.

As the images illustrate, when structural integrity of the CM completely failed, it did so in a fraction of a second. The times for the images (figure 2.4-2), from top to bottom, are GMT 14:01:06.73, GMT 14:01:06.87, GMT 14:01:06.97, GMT 14.01.08.3, and GMT 14:01:09.67. In the next frame, the CM is no longer visible.

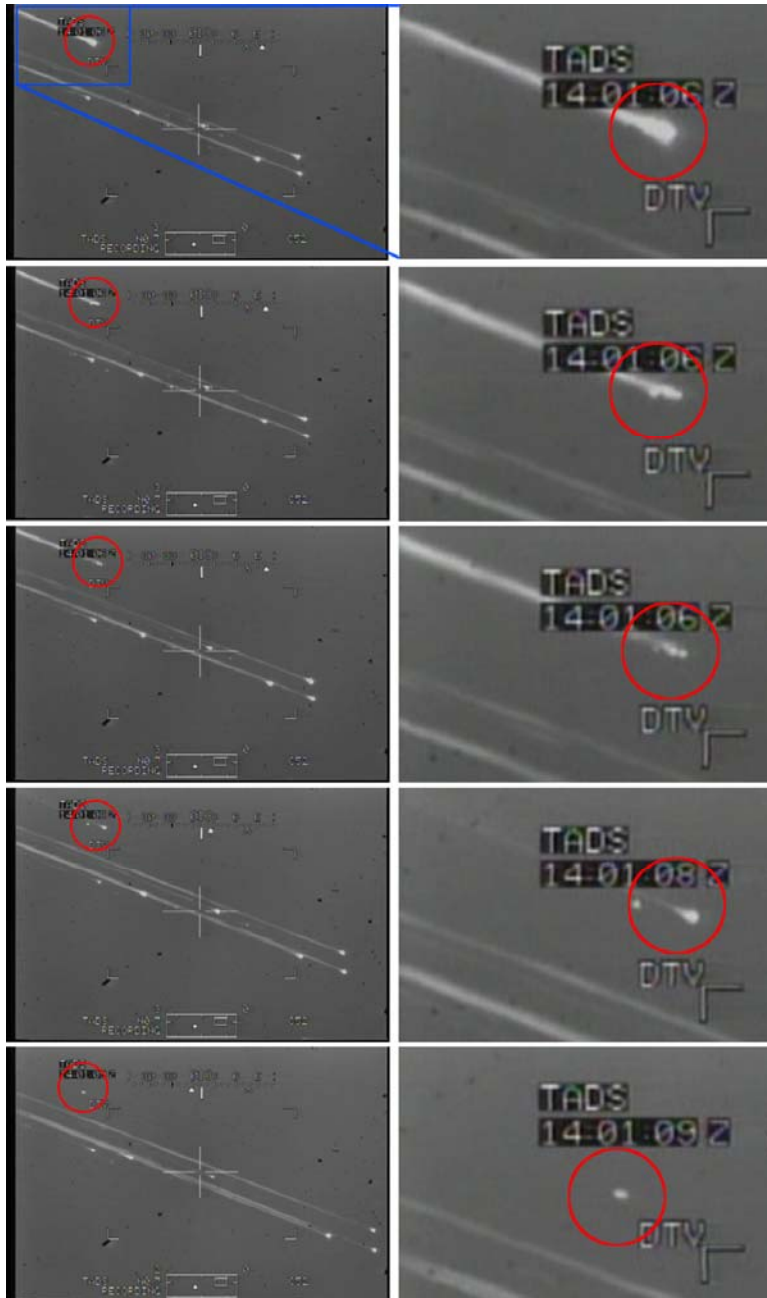


Figure 2.4-2. Apache video of the Total Dispersal, spanning from GMT 14:01:06.73 to GMT 14:01:09.67. The forebody/crew module is circled in red.

### Relative motion analysis

Relative motion analysis compares the rate of change of the movement of objects in the FOV of a video. Rate of change can provide an estimation of the G-load that is experienced by the bodies within a relative frame of reference; e.g., a relative difference might be that one object experiences a deceleration of 3 G

relative to another object. While the analysis indicates that the first object experiences three more Gs than the other object, it does not define how many total Gs either object is actually experiencing.

Two relative motion analyses were performed. The first regarded a triangulation of the motion of the forebody relative to the engines between the CE and the CMCE (see Section 2.1).

The second relative motion analysis was performed on the CM (identified as D21) and the aft engines post-CMCE in a stabilized Apache video (figure 2.4-3).

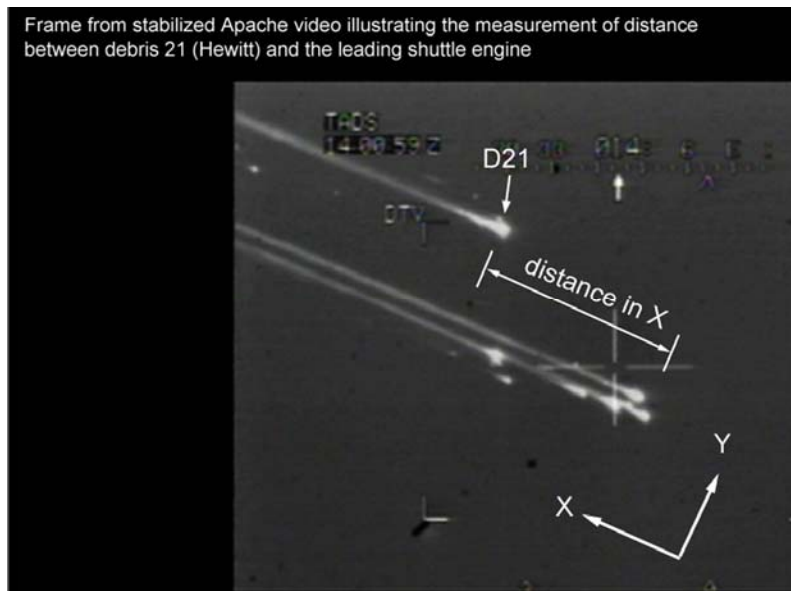


Figure 2.4-3. An analyzed frame from the Apache video.

The relative motion of the CM to the engines appears to suggest a high deceleration event occurred during the breakup of the forebody (between the CMCE and the TD). Later understanding of the breakup sequence revealed that this deceleration was related to the disintegration of the CM and the resulting cloud of debris. Rather than a specific high-G event that was experienced by an intact CM, it represents the cloud of individual items separating and rapidly decelerating. Heating was sufficient to keep the individual objects visible for a short period of time, and these items were close enough together that they could not be distinguished as separate items. This also explains why the CM's visible disappearance occurred in a fraction of a second, as the deceleration passed the threshold of sufficient heat generation for visibility in the video.

## 2.4.2 Ballistic analysis

Refer to Section 2.2.2 for a full description of the techniques, assumptions, and limitations for ballistic analyses.

### Forebody structure

Table 2.4-1 shows the debris ballistic timeline for some selected forebody structures. Ballistic analysis could not be done on all recovered debris because ballistic numbers are hard to estimate for irregularly shaped objects and the analysis is time-intensive. For some structures, there is a major structural release time. For other objects, the major structural release time is the same as the debris object release time since there is only one object.

**Table 2.4-1. Ballistic Timeline for Post-Crew Module Catastrophic Event Forebody Events**

Major Structural Release Time (GMT)	Vehicle Structure	Debris Object Number and Time of Release (GMT)
14:00:54	FF	11119 (14:00:51) 81231 (14:00:55) 26099 (14:00:55)
14:00:57	Forward RCS strut	2170
14:00:59	Forward RCS thruster	2167
14:01:05	Thermal pane glass (outer pane)	14:00:57 (65012) 14:01:02 (68534) 14:01:04 (1574) 14:01:05 (73192) 14:01:16 (77517)
14:01:07	FF port ejection panel <sup>1</sup>	51987
14:01:12	Nose cap	257
14:01:13.5	Forward RCS helium tank	14:01:13 (1481) 14:01:14 (1209)
14:01:35	FF starboard ejection panel	71801

These individual release times alone did not provide significant insight into the breakup event, but will be compared to other analyses in this section. However, the times generally span the video determination for the time between the CMCE and the TD. Although a few items appear to have been released after the TD, cascading failures were expected to occur even after the TD, and this accounts for those times being later (see Section 2.2.2).

#### **Crew module interior items**

Objects that are discussed in this section originated from inside the CM but are not directly associated with a seat or a crew member. All of the items listed were selected because their shapes were easily modeled for ballistic analysis, and all are believed to have been stowed or located in the middeck. No flight deck structural debris items were good candidates for ballistic analysis because of their irregular shapes. For a detailed discussion of individual crew seat and crew equipment recovery, see Sections 3.1 and 3.2. The results of that ballistic analysis concluded that the middeck seats and equipment were released prior to the flight deck.

The release times and descriptions of these interior items are in Table 2.4-2. The mission patch (debris item no. 31539) in this table should not be confused with the separate mission patch that is identified in the cabin depressurization analysis, which was one of the most westerly objects recovered.

<sup>1</sup>*Columbia* was the only orbiter in the fleet with ejection hatches for the Commander and Pilot stations. The ejection seat systems were disabled and the ejection hatches were deactivated when the orbiter program was deemed operational. Eventually, the ejection seats were removed from *Columbia*, but the hatches remained as an integral part of the structure of the FF.

**Table 2.4-2. Individual Debris Objects for the Crew Module Post-Crew Module Catastrophic Event**

Release Time (GMT)	Debris Number	Description	Shape
14:00:56	55952	Toilet handle ball	sphere
14:01:01	31539	STS-107 mission patch	triangular
14:01:02	1170	Middeck floor section	rectangular
14:01:07	1155	Middeck accommodation rack (MAR)	rectangular
14:01:07	2499	Middeck floor section	rectangular
14:01:08	44199	Volume E access door	rectangular
14:01:10	23262	Locker door	rectangular
14:01:10	7717	Photo TV floodlight	rectangular
14:01:13	7662	Light emitting diode (LED) indicator panel	square
14:01:15	8820	Window shade bag	rectangular

Again, no major conclusions could be drawn from these data alone. However, like the structures ballistic analysis, these times are consistent with the times for the CMCE and the TD as determined by video.

### 2.4.3 Cluster analysis

For a complete discussion of the techniques, assumptions, and limitations of cluster analysis of the debris fields, see Section 2.2.3.

#### Catastrophic Event to Crew Module Catastrophic Event

The most significant finding from debris field analysis showed that the FF and CM appeared to remain relatively intact from the CE to the CMCE, a period of 35 seconds (see Section 2.2.3). Small amounts of forebody structure, such as some nose landing gear door tile and small structure, were released earlier. However, 87% of the FF structure and all of the CM pressure vessel structure debris clusters overlap completely (figure 2.4-4), strongly suggesting a relationship between their structural failure. The western end of the main portion of the forebody structure debris field is at a longitude of 94.5W.

The fact that the forebody maintained structural integrity immediately after the orbiter breakup may be explained by the reduction in deceleration loads occurring at the CE due to the change in ballistic number. However, thermal effects would begin to increase, and deceleration loads once again began to build up to a peak of 3.5 G at the forebody c.g. at the CMCE. Note that loads experienced at the farthest outboard edges of the forebody could be as high as 10 G to 12 G at the CMCE due to the moment arm from the c.g. as the forebody rotated.

#### Cabin pressurization

Cabin depressurization was an important event to identify. The initiation of the depressurization of the cabin could not be observed in the video. However, the debris field provided the opportunity to evaluate when depressurization may have started, because items that were originally stowed inside the CM and recovered west of the main forebody debris field could indicate a CM breach.

Items that were stored on board the orbiter were carefully packed, stowed, and documented prior to launch. Some items on STS-107 were stowed in the middeck and the SPACEHAB (laptop computers and LiOH canisters). Most items also had a designated entry stowage location. Common use items (such as pens and

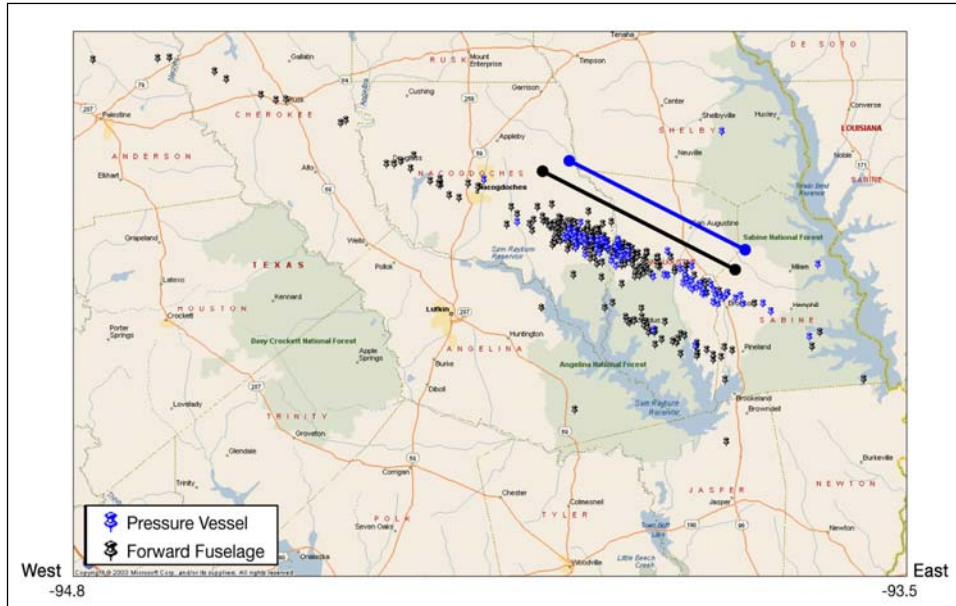


Figure 2.4-4. Debris field of the forward fuselage and crew module pressure vessel.

pencils) are not carefully tracked and not necessarily re-stowed to launch configuration for entry. In particular, trash was stored in multiple areas such as the SPACEHAB, the airlock, and the middeck volumes, some of which extend into the lower equipment bay below the middeck floor. The SCSIT chose to investigate only nonstructural items with accurately known storage locations. No CM pressure vessel structure or significant interior structure was recovered west of the main forebody debris field. Nonstructural items that were recovered west of the main forebody debris field were assumed to have been evacuated from the CM due to decreasing pressure and a small breach in the CM rather than major structural degradation. Study of these objects allowed the team to better understand when pressure inside the CM was lost, and to determine the areas where suspected breaches might have occurred.

Many “crew equipment” items that are listed in the database west of longitude 94.5W may not have originated from *Columbia*. Because they represent common use personal items, they cannot positively be identified as from the orbiter and may be discarded items that were present in the debris field. The items that can confidently be concluded came from the orbiter include empty food packets, LiOH canisters, clothing, and laptop computer debris. The bulk of these items were stored in the middeck lockers, the lower equipment bay volumes, the SPACEHAB, the airlock, and the Waste Collection System (WCS).

Seventy-one items were recovered west of longitude 94.6W and were positively identified from the middeck, flight deck, or CEE. The specific locations for these items were Volume E, middeck lockers MF43K and MF43C, port middeck and stowage volumes from the lower equipment bay, flight deck illuminator panels (i.e., acrylic sheeting), and equipment from the flight deck. These items were all small (< 8 in. and, in most cases, much smaller).

In general, small and light items did not travel downrange significant distances due to the ballistic properties of the object. Some paper/lightweight items were offset slightly northeast of the main debris footprints, probably due to the prevailing winds at the time of the accident. Figure 2.4-5 shows the debris field for nonstructural internal CM debris.

Many of the westernmost debris items came from internal stowage volumes. This implies that internal structural damage occurred at the CE. A full description of cabin depressurization is contained in Section 2.3. The integrated assessment concluded that depressurization occurred NET GMT 14:00:18 (CE) and NLT GMT 14:00:35. It ended NLT GMT 14:00:59, and most likely earlier.

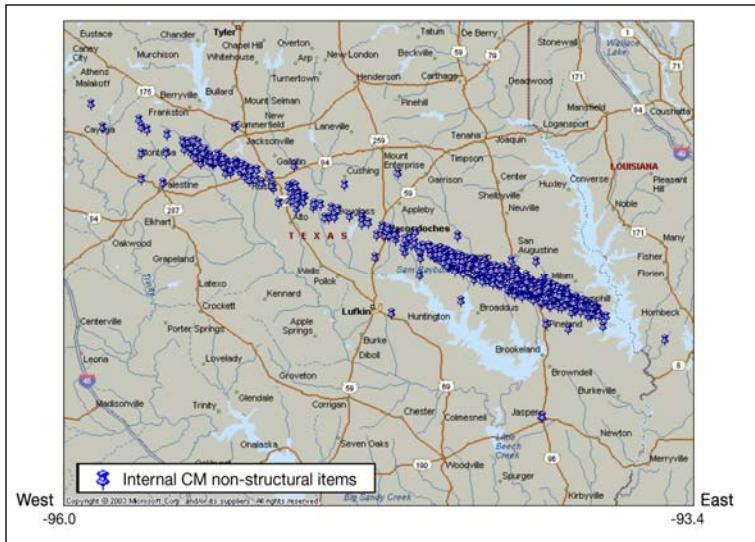


Figure 2.4-5. Debris field of the nonstructural items from inside the crew module pressure vessel.

### Window panes

A perceived vulnerable area of the forebody was the windows. Most of the windows in the forebody are triple-paned. Only the two aft windows, which are protected by the PLBDs during entry, are double-paned. For the three-paned windows, the exterior panes are “thermal” panes that provide thermal protection. The inner panes are “pressure” panes that provide structural support for the pressure inside the CM. The middle pane is a “redundant pane” as it is intended to be redundant for both the thermal and the pressure pane. Figure 2.4-6 shows the schematic of the three-paned window of an orbiter.

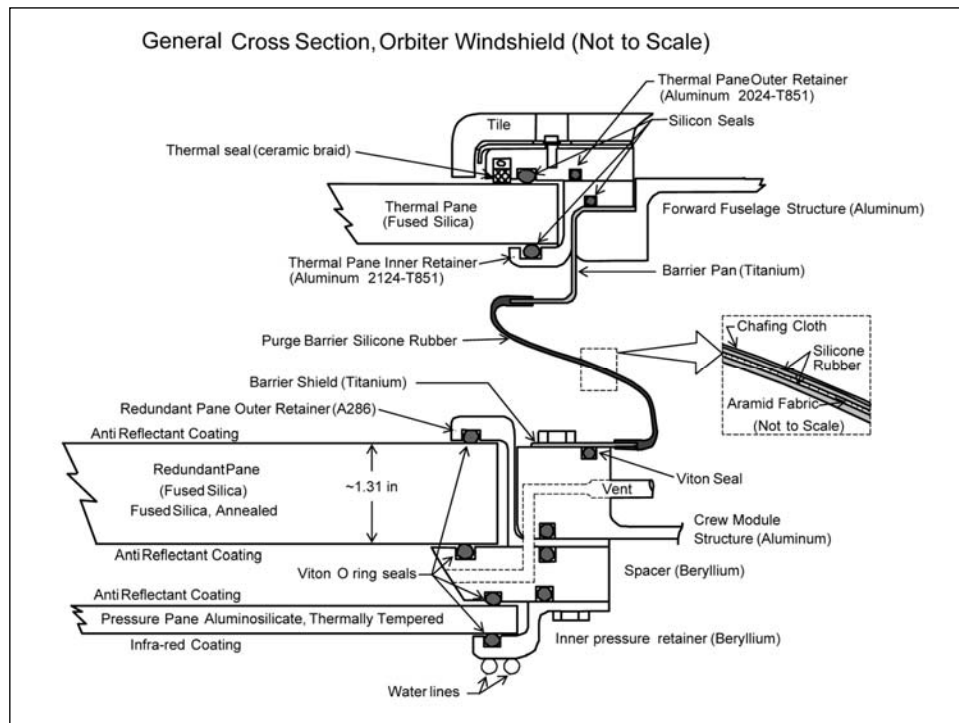


Figure 2.4-6. Schematic of the orbiter three-paned window.

Figure 2.4-7 shows the numbering system for the windows; the forward windows are numbered 1 through 6, the overhead windows are 7 and 8, and the aft-facing windows are 9 and 10. Window 11 (not shown) is the side hatch window. The thermal, redundant, and pressure panes vary in thickness depending on location on the vehicle. Table 2.4-3 shows the specified thicknesses for the various panes from the 11 different windows.

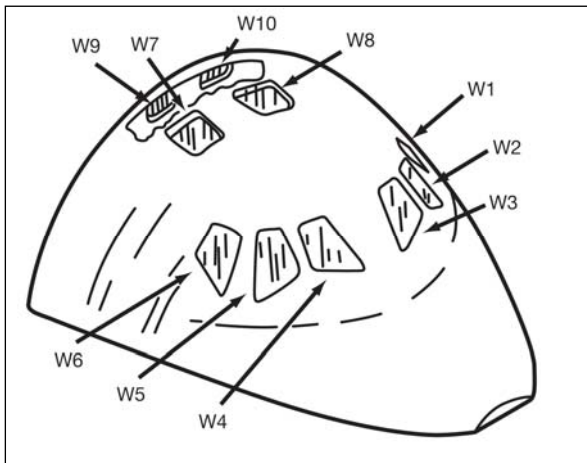


Figure 2.4-7. Window numbering system.

Table 2.4-3. Specified Orbiter Window Design Thicknesses

Size (in.)	Window pane
0.29	Side hatch thermal pane
0.33	Windows 9, 10 redundant pane (tempered) Windows 9, 10 pressure pane (tempered)
0.47	Windows 7, 8 redundant pane (tempered) Windows 7, 8 pressure pane (tempered)
0.49	Windows 7, 8 thermal pane Side hatch redundant pane
0.56	Windows 1, 6 thermal pane
0.61	Windows 2, 5 thermal pane
0.62	Side hatch pressure pane
0.63	Windows 3, 4 pressure pane (tempered)
0.65	Windows 1, 2, 5, 6 pressure pane (tempered)
0.69	Windows 3, 4 thermal pane
1.30	Windows 3, 4 redundant pane
1.32	Windows 1, 2, 5, 6 redundant pane

The orbiter windows are made of a compositionally unique fused silica that is highly thermally stable and not expected to thermally degrade under entry heating. Material analysis was not a primary means of assessment due to limited resources. Recovered glass was identified by measuring the thickness and comparing it to the data shown in Table 2.4-3. The highest confidence was in the approximately 1.3-in.-thick redundant panes of glass since this is not a common commercially available thickness. Due to the shattered nature of the tempered-glass fragments, further identification was difficult for loose fragments (those not retrieved from within the frames).

Initially, the windows were considered as a potential site of cabin breach due to thermal failure. The thermal panes, while designed to withstand thermal conditions, are not normally exposed to the highest entry heating conditions because of the geometry of the vehicle and its nominal attitude during the heating phase on entry. However, a preliminary thermal analysis showed that the structure around the windows would fail thermally before the window panes.

A different concern was whether the flexing of the structure under the varying loads at the LOC and the CE would cause the glass to shatter. The debris field analysis refuted that theory as well. Figure 2.4-8 shows the debris field coordinates for recovered glass.

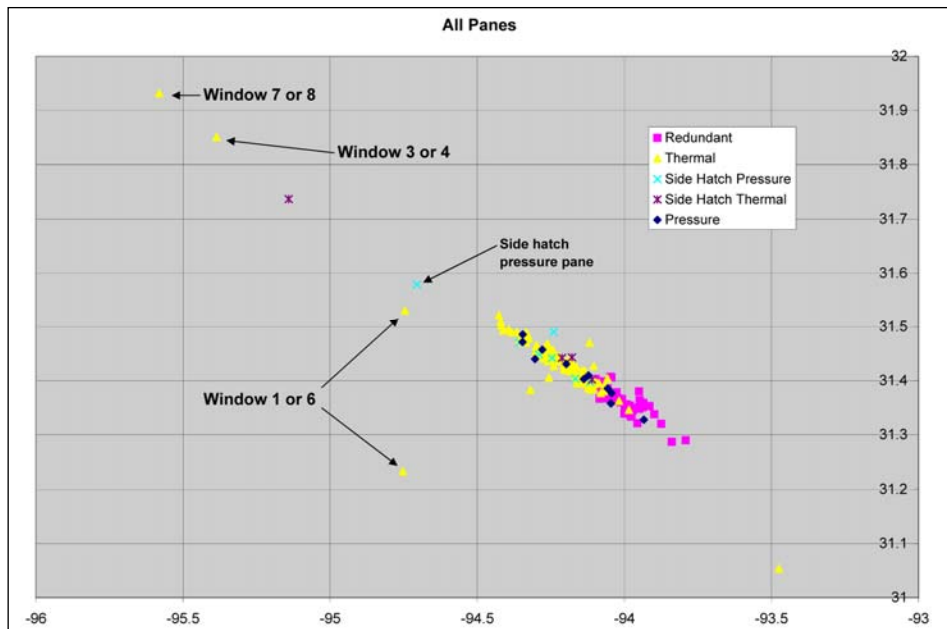


Figure 2.4-8. Recovered debris field for window glass.

Of the 201 recovered glass fragments, only six pieces of loose glass that are confidently believed to be from the orbiter were found west of the main forebody debris field. All were thermal (outer) panes with the exception of one piece of probable side hatch pressure pane. However, a piece of pressure pane that was recovered in the western end of the debris field does not alone indicate a source of depressurization. Pressure panes may be damaged due to objects moving around inside the CM as it rotated, impacting the windows. If the cabin is depressurized from a different source, these pieces can evacuate through other breaches.

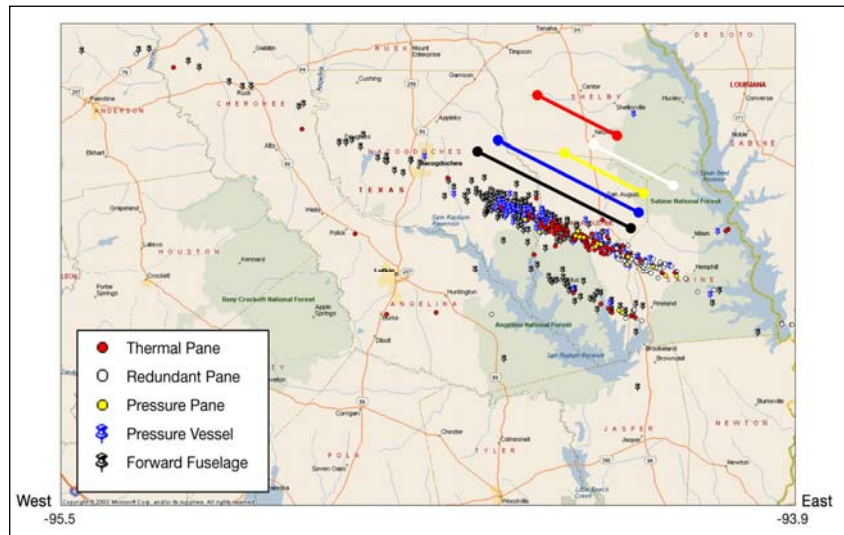


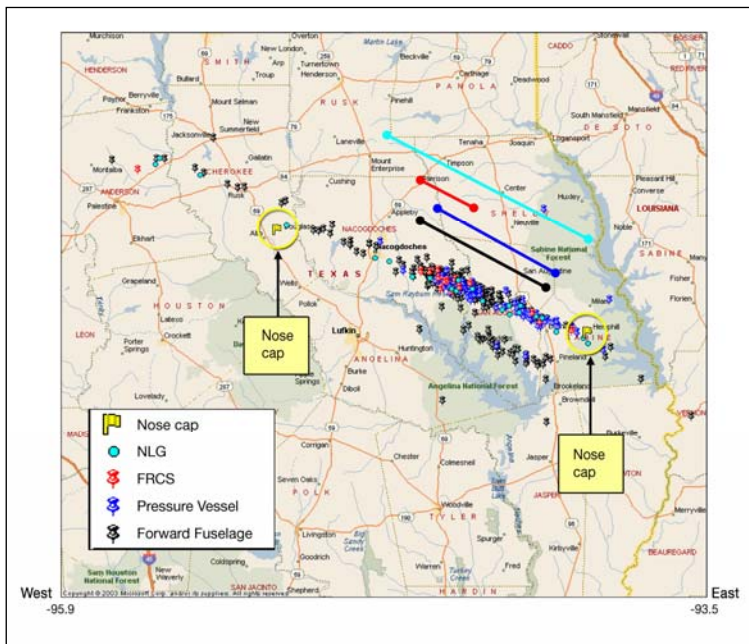
Figure 2.4-9. Debris field of the window panes, forward fuselage, and crew module pressure vessel.

If the source of the cabin depressurization had been a window, both the pressure pane and the redundant pane would have to have failed. However, redundant pane is not seen until the far eastern end in the forebody debris field. Also, in such a case, the pressure from inside the CM would likely blow the entire pane out and result in significant amounts of glass that were not seen west of the main forebody debris field.

Figure 2.4-9 shows the window debris field overlaid on the FF and pressure vessel debris fields.

Figure 2.4-9 shows that thermal pane debris was recovered east of the beginning of the main forebody debris, suggesting that the windows broke at or after the CMCE. Pressure panes were recovered west of the bulk of the redundant panes, possibly because the redundant panes were extraordinarily thick and heavy and may have traveled farther east because their ballistic number was higher. Determining the failure sequence of the windows based on ground plots alone was somewhat suspect because some of the window frames remained attached to other window frames as a unit, and the shape of the windows can potentially generate lift. Regardless, because the debris field does not contain significant pane debris west of the main CM debris field, it is concluded that the windows were not the source of a CM breach or a part of the initiating event of the forebody breakup.

**Finding.** The *Columbia* windows remained largely intact up until the CMCE and were not a cause of cabin depressurization.



**Post-Crew Module Catastrophic Event forebody breakup**

This section discusses the debris field clusters related to the CMCE and the breakup of the forebody. Figure 2.4-10 shows the major elements of the forebody including the CM pressure vessel, FF, forward RCS, nose, and nose landing gear debris. Figure 2.4-11 shows greater detail regarding specific items and highlights the scarcity of items recovered prior to the main FF/CM debris field.

Figure 2.4-10. Debris field of the forebody components.

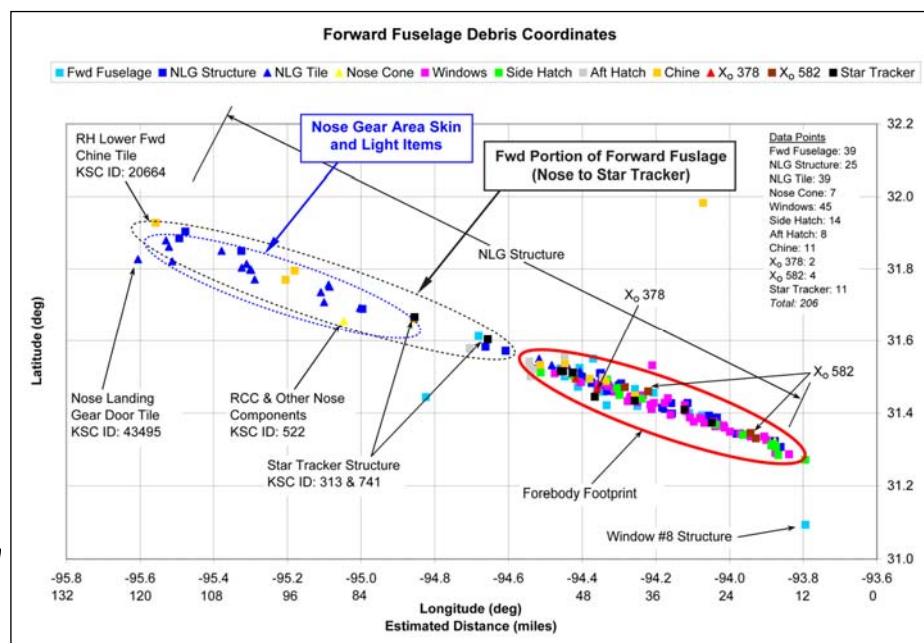


Figure 2.4-11. Forward fuselage debris field.

The debris field analysis suggests that the order of separation was as follows: nose landing gear structure and nose cap, FF, and forward RCS, followed by the CM pressure vessel. This is consistent with the video that appeared to show FF separating, followed very quickly by failure of the CM.

### Crew module interior structure

The CM interior structure discussion includes the flight deck, middeck, and airlock. *Columbia* was the only orbiter with an internal airlock, meaning that the airlock structure was located inside the middeck of the CM rather than in the payload bay like the other orbiters.

### Middeck and flight deck

Figure 2.4-12 shows the distribution of middeck and flight deck structure. The middeck structure appears farther west in the debris field, while the flight deck debris cluster is concentrated at the eastern end. This suggests that the flight deck remained intact longer and traveled farther downrange than the middeck.

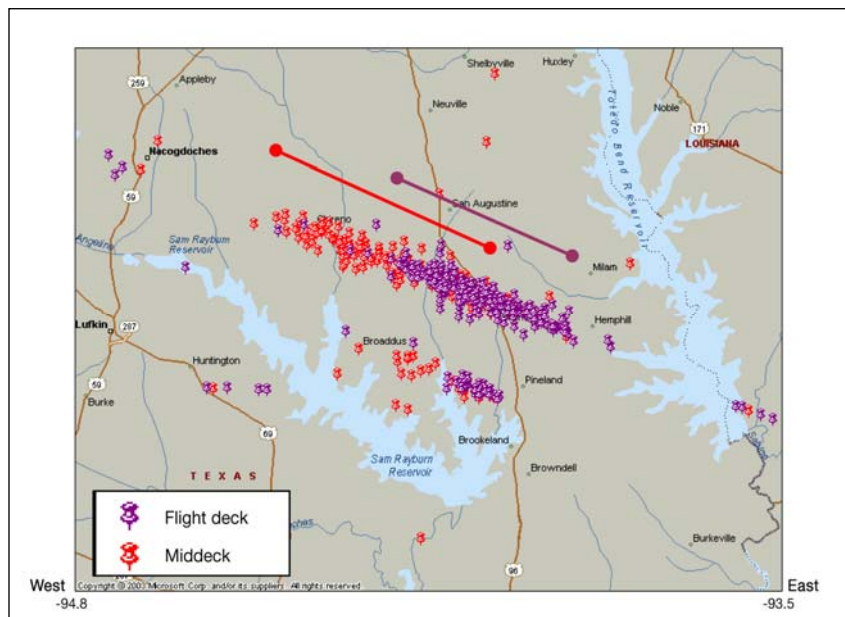


**Figure 2.4-12. Debris field of the middeck and the flight deck.**

This conclusion is supported by the fact that almost all of the middeck floor debris was in fair to very good condition. However, very little of the structurally stronger flight deck floor was recovered. Furthermore, the flight deck items that were recovered were heavily thermally eroded. This would be the case if the flight deck stayed together and received more thermal damage as a result of having a higher ballistic number than the individual middeck components.

Ground debris footprints for the crew worn equipment and seats are not addressed in this section. The analyses and conclusion from the seat and suit assessments (see Sections 3.1 and 3.2) also concluded that the middeck elements separated before the flight deck elements. This supports the conclusions from the structural debris fields.

The debris field was also evaluated based upon whether debris items came from the port or starboard side of the orbiter. Figure 2.4-13 shows the middeck structure debris field. Figure 2.4-14 shows the flight deck panel debris field.

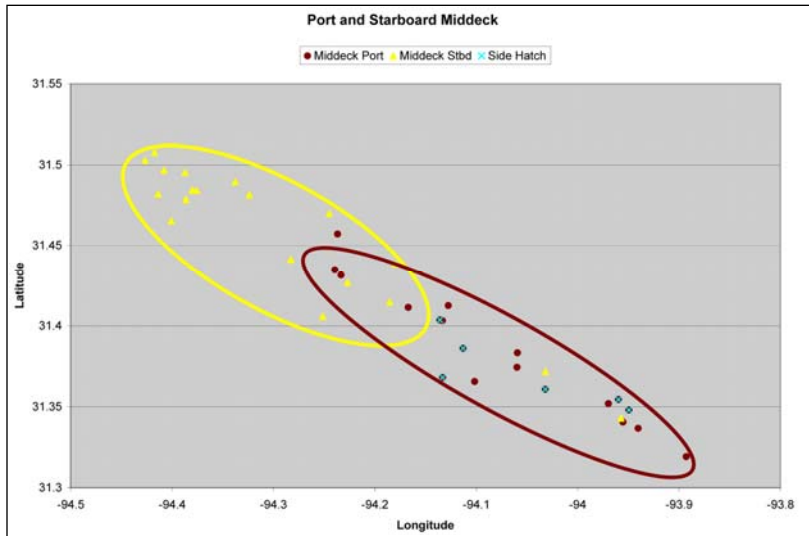


Figure 2.4-13. Middeck structural debris port vs. starboard.

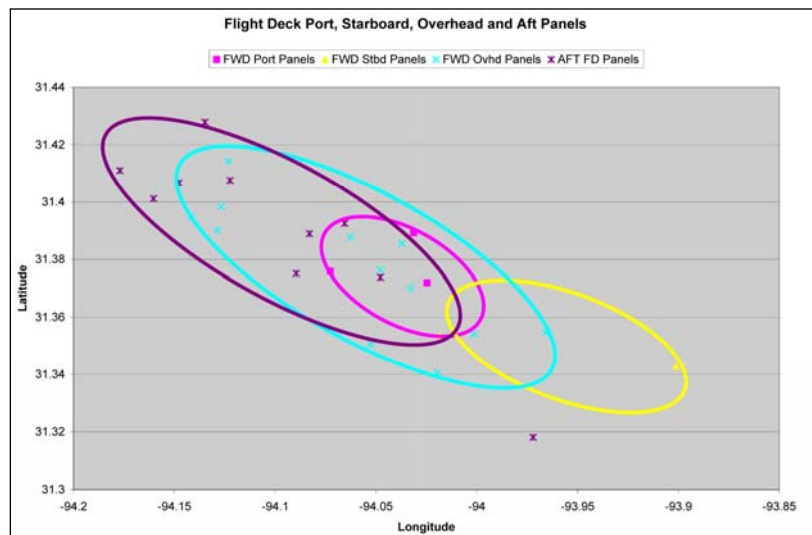


Figure 2.4-14. Flight deck panels by overhead, port, and starboard.

There was a substantial amount of debris for the middeck analysis. Middeck starboard debris was recovered west of the middeck port debris, suggesting that the starboard side failed before the portside. Many of the items from the starboard side were lightweight items from the sleep station with low ballistic numbers, which may also affect this debris field. The debris field is consistent with a yaw to the portside, exposing the starboard side to greater thermal and aerodynamic loads. However, the flight deck panels appear inconclusive relative to a specific failure sequence of forward to aft or port vs. starboard. Not many panels were recovered from port or starboard, which makes interpretations risky.

**Airlock**

The airlock was located on the middeck. The aft opening of the airlock had no hatch and was open to the tunnel to the SPACEHAB in the payload bay. The forward hatch, leading to the CM, was closed and locked. Therefore, the airlock could lose pressure without impacting the internal conditions of the CM. See Section 2.2.4 regarding the failure of the TAA and subsequent depressurization of the airlock at or closely after the CE.

A few “loose” items, as well as a few items that were adhesively bonded to structure and a few pieces of secondary structure, were recovered in the western end of the debris field, indicating that these items were evacuated from the airlock when the TAA departed (figure 2.4-15). However, almost 80% of the airlock structure was recovered in the eastern portion of the forebody debris field (figure 2.4-16).

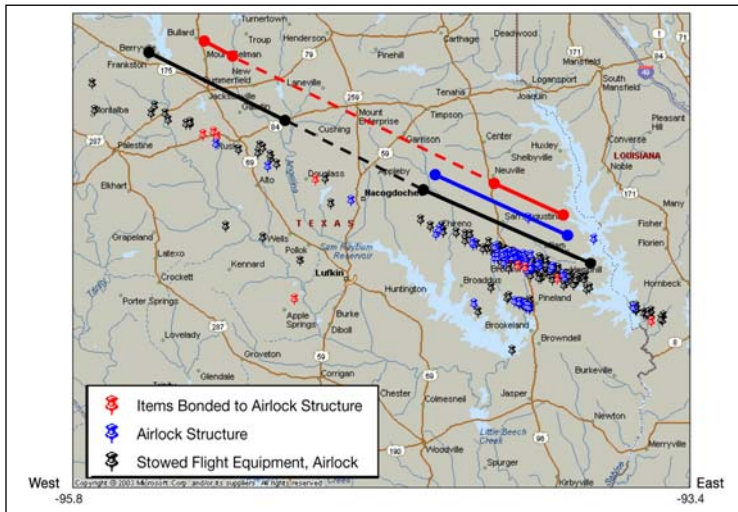


Figure 2.4-15. Debris field of the airlock structure, flight crew equipment stowed in the airlock, and items bonded to airlock structure.

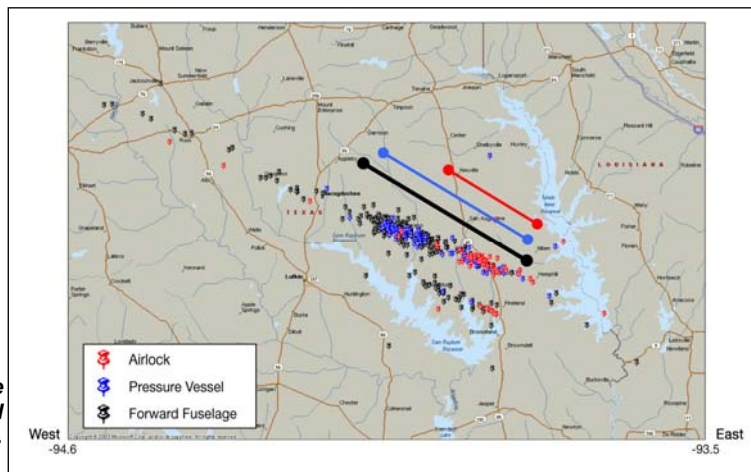
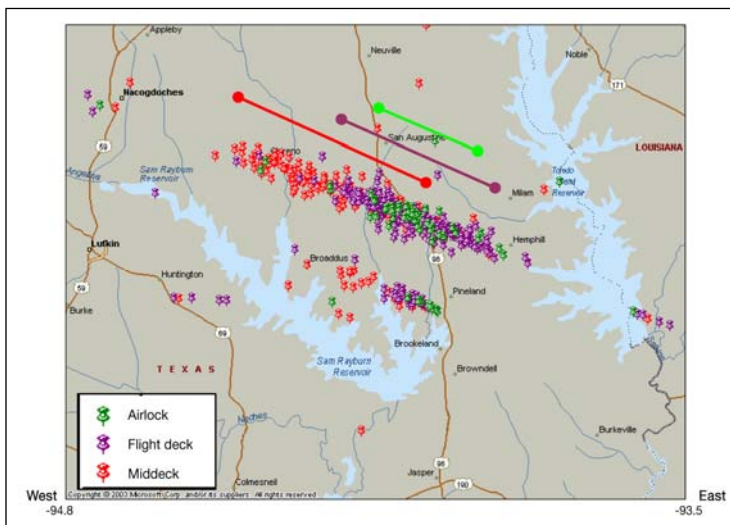


Figure 2.4-16. Debris field of the forward fuselage, pressure vessel, and airlock structure.



The internal airlock is structurally attached to the CM aft of the X<sub>0</sub> 576 bulkhead. It likely stayed with the aft bulkhead after the middeck departed. Figure 2.4-17 indicates that the airlock structural debris is also squarely in the middle of the flight deck structural debris. This suggests that the flight deck and airlock remained connected to each other by the aft bulkhead.

Figure 2.4-17. Debris field of the middeck, flight deck, and airlock.

**Forebody structural bulkheads**

The forebody contained four major bulkheads. The bulkhead that was aft of the forward RCS compartment and immediately in front of the CM forward bulkhead was the  $X_{cm}$  378 bulkhead. The forward bulkhead of the CM was the  $X_{cm}$  200 bulkhead.<sup>2</sup> The aft bulkhead of the CM was the  $X_o$  576 bulkhead, and the bulkhead immediately aft of it was the  $X_o$  582 ring frame bulkhead (figure 2.4-18).

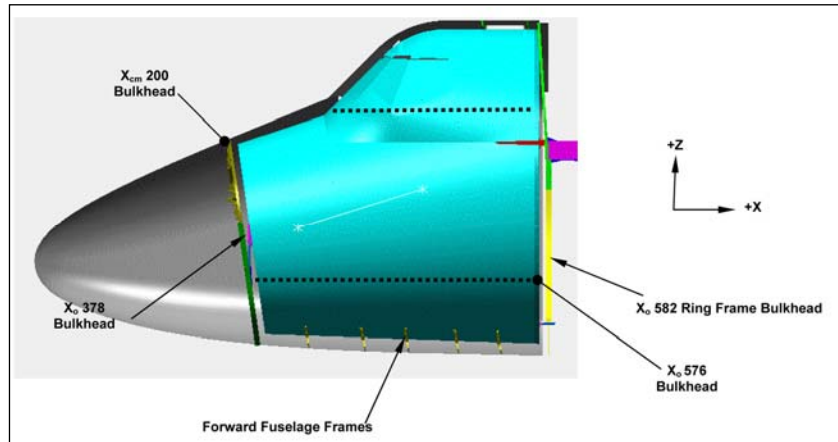


Figure 2.4-18. Forebody bulkheads.

Figure 2.4-19 shows the bulkhead debris field clusters relative to each other. Figure 2.4-20 shows the CM ( $X_{cm}$  200 and  $X_o$  576) bulkhead debris fields relative to the middeck and flight deck debris fields.

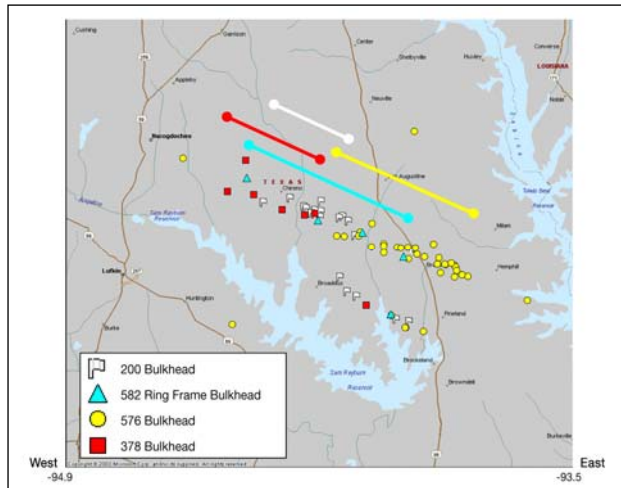


Figure 2.4-19. Debris field of the key forebody bulkheads.

<sup>2</sup>The  $X_{cm}$  reference frame is the CM reference frame. The  $X_{cm}$  reference frame axes are aligned with the  $X_o$  reference frame, but the X-axis origin is different.

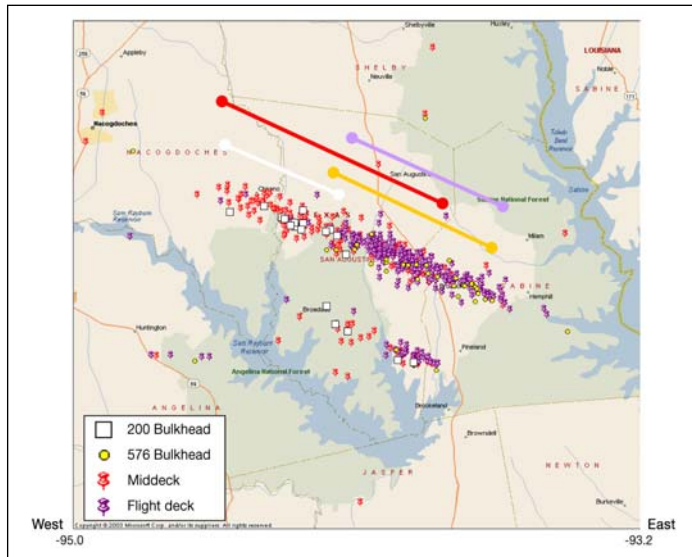


Figure 2.4-20. Debris field of the crew module bulkheads, middeck, and flight deck.

The debris field clusters suggest that the two forward bulkheads appeared to fail earlier than the aft bulkheads. Also, the outer (fuselage) bulkheads failed prior to their corresponding inner (CM pressure vessel) bulkheads. The debris footprint for the CM forward bulkhead ( $X_{cm}$  200) coincides with the center of the middeck debris field, suggesting that the  $X_{cm}$  200 departed with the middeck. The CM aft bulkhead ( $X_o$  576) appears to have remained with the flight deck until it disintegrated, likely also connected to the airlock since that debris field coincides as well.

This agrees with the general conclusion that the FF failed followed by the CM pressure vessel failure.

### Avionics bays

The CM avionics bays debris plots were also evaluated to see whether they might provide insight into the CM failure sequence. These bays are in immediate proximity to the forward and aft bulkheads of the CM.

Debris plots represent debris from four avionics bays that are located on the mid-deck. Avionics Bays 1 and 2 are in the forward-most portion of the CM, immediately aft of the forward  $X_{cm}$  200 bulkhead. Avionics Bays 3A and 3B are in the aft of the middeck on starboard and port sides of the airlock, respectively. These bays are immediately forward of the aft  $X_o$  576 bulkhead. Although Bays 3A and 3B are smaller than Bays 1 and 2, a greater number of items were recovered from Bays 3A and 3B than from the forward bays. The recovered debris (mostly avionics boxes) were remarkably consistent in shape and subsequently estimated ballistic number, so the clusters were assumed to be adequate for a relative assessment (figure 2.4-21).

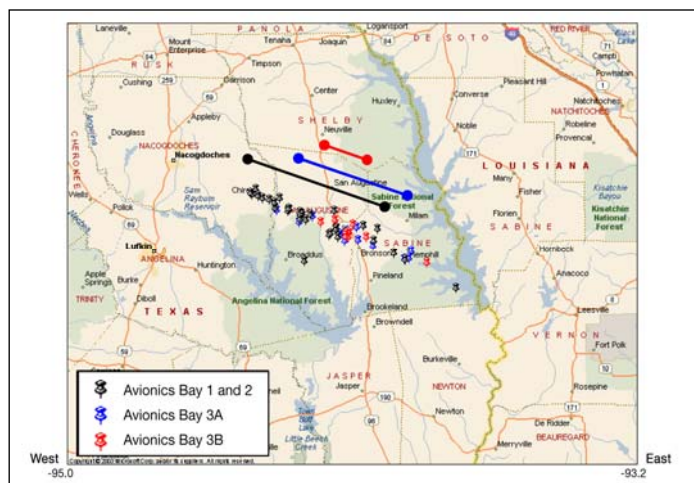


Figure 2.4-21. Debris field of the avionics bays.

Debris from Bays 1 and 2 was recovered west of Bays 3A and 3B. This order matches the CM bulkhead order, supporting that the front ( $X_{cm}$  200) bulkhead departed before the aft ( $X_o$  576) bulkhead.

**Sequencing based on cluster, video, and ballistic analysis**

Figure 2.4-22 shows the relationships of some of the addressed forebody structures. The CM bulkheads are included in CM structure, and the X<sub>o</sub> 378 bulkhead is included in the FF structure. The percentages listed in the figure refer to percentage of recovered debris, not percentage of the original intact area.

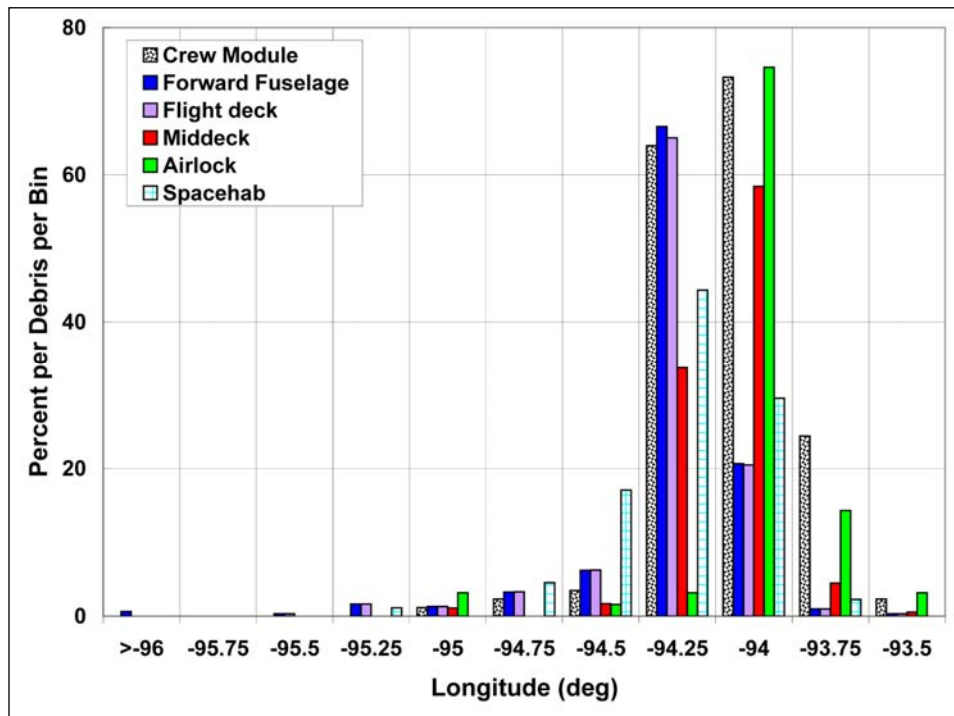


Figure 2.4-22. Histogram of the forebody structural components, plus SPACEHAB.

To summarize the video and debris field findings, at the CE the CM was contained within the FF structure. The CM began to depressurize through a series of small breaches, with small amounts of FF debris being shed. Eventually, the FF structure failed, and the CM itself failed within a few seconds afterwards. The middeck and forward bulkhead (X<sub>cm</sub> 200) of the CM departed, while the airlock, flight deck, and aft bulkhead (X<sub>o</sub> 576) remained together for a short period longer until all elements separated and the TD occurred.

**2.4.4 Structural analysis**

This section discusses the breakup of the forebody based on structural analysis, using supporting evidence from the video, ballistic, and debris cluster analyses. See Section 2.2 for a more detailed discussion of the separation of the forebody from the orbiter. This analysis specifically discusses events that are related to the forebody at the CE and ending at the TD.

**2.4.4.1 Events at the Catastrophic Event**

**General condition of forebody recovered debris**

The recovered FF components are predominantly skin/stringer segments. Most components exhibited mechanical overload as the primary failure mechanism. Roughly 40% of the FF was recovered with no difference in damage levels comparing left to right or upper to lower. Two recovered RCC components, the nose cap and the chin panel (figure 2.4-23), show evidence of mechanical breakup with low thermal damage. It should be noted that the nose cap, based on field reports, apparently hit a tree before hitting the ground. The presence of intact Koropon primer on many FF components indicates that significant heating did not occur. Temperatures above 400°F (204°C) degrade the primer’s appearance, and high temperatures

(>900°F) (486°C) will completely ablate it. The presence of Koropon indicates that the breakup of these elements was caused by mechanical overload rather than thermal effects.



**Figure 2.4-23. Nose cap Columbia Reconstruction Database debris item no. 1114 vs. the original nose cap with chin panel.**

Some large pieces of the forward RCS were recovered (figure 2.4-24). These exhibit evidence of mechanical overload as the primary failure mechanism. Heating did not appear to play a significant role in the component degradation and appears to have occurred during or subsequent to the mechanical breakup.



**Figure 2.4-24. Two large forward Reaction Control System debris pieces, Columbia Reconstruction Database debris item nos. 792 (left) and 82061 (right).**

Very few CM skin pieces were recovered. Most skin components were identified as portions of the thicker sections of the aft and forward bulkheads; the pieces all exhibit heavy thermal erosion. Several skin pieces that were identified as part of the CM center/bottom strip (“keel”) were recovered. These pieces exhibit some mechanical breakup along with heat erosion within this thicker strip.

More than 65% of the middeck floor panels were recovered with paint and Koropon primer still intact, indicating that they were exposed to low thermal erosion.

Small numbers of the flight deck floor structural pieces were recovered; all recovered pieces exhibit heavy thermal erosion.

**Crew module attach fittings (x-links, y-links, z-link)**

All four main CM/FF attach links were recovered. In Section 2.2, it was concluded that the attach fittings, which are known as the x-links, y-links, and z-link, stayed with the forebody. These fittings attach the CM to the FF. The x-links also bridge to midbody structure. For a more detailed discussion of these attach fittings, refer to Section 2.2.4.

**X-LINKS**

Both the port and the starboard x-links (figure 2.4-25) were recovered nearly intact with evidence of high heating. The titanium fittings on both links experienced significant thermal exposure/melting, predominantly on the upper surfaces. Additionally, the starboard side fitting experienced significantly greater heating and erosion than the portside.

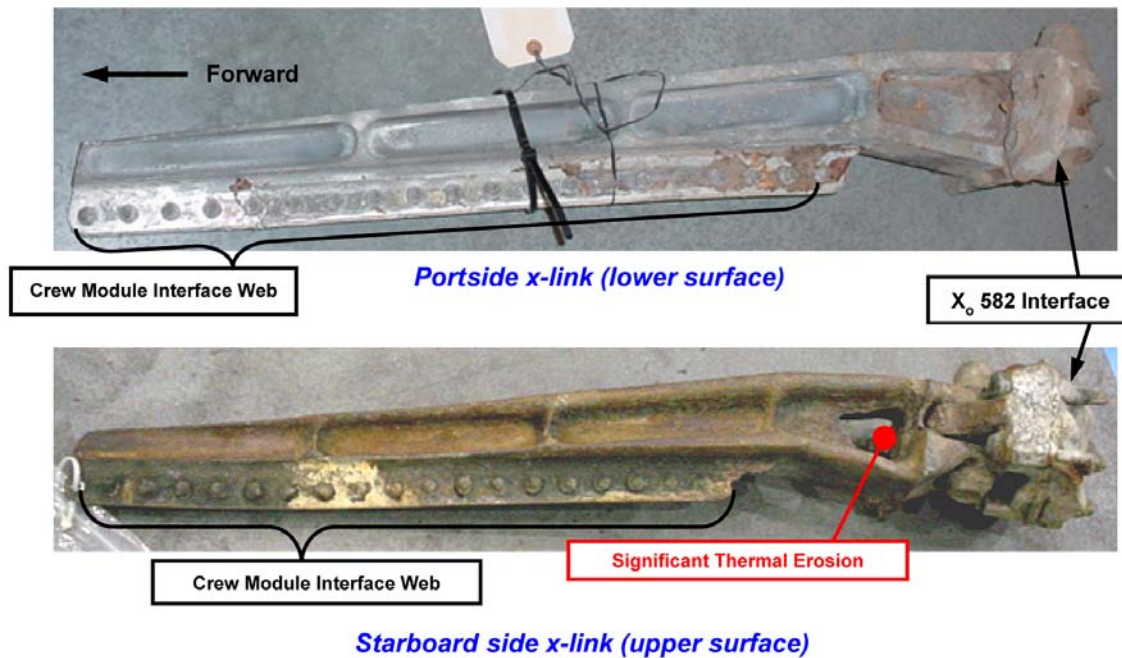


**Figure 2.4-25. Crew module x-links, Columbia Reconstruction Database debris item nos. 1678 (top) and 1765 (bottom).**

The titanium x-link components did not fail. The attach area on the CM side of the x-link is stronger than the FF side since it is reinforced by the flight deck floor and the X<sub>o</sub> 576 bulkhead. The failures occurred at the weaker X<sub>o</sub> 582 ring frame bulkhead connection points. The port x-link experienced a mechanical lug failure at the X<sub>o</sub> 582 ring frame bulkhead interface, while the starboard side fittings pulled through the X<sub>o</sub> 582 ring frame bulkhead at the CE. The starboard x-link retained some of the sill and X<sub>o</sub> 582 ring frame bulkhead while the portside did not. Furthermore, it was concluded that at the CE, the forebody rotated left and pitched down, separating from the midbody (see Section 2.2.4).

Heat damage patterns on the webs of both x-links indicates that, at some point, there was hot gas flow from aft to forward above both x-links. The starboard x-link has more damage than the port x-link. Thermal analysis (see Section 2.1.6.7) of the x-links shows that entry heating alone was not capable of causing such heavy erosion. Additionally, because the surrounding structure was aluminum with a much lower melting temperature, entry heating alone would have resulted in the weakening of the surrounding structure first and release of the x-links. Section 2.1.7 discusses the other thermal mechanisms that were likely involved, shock-shock interactions and combustion. Both of these mechanisms are possible with the forebody geometry as understood from the debris.

Debris item no. 2436 is a piece of FF skin panel outside of the starboard x-link (figure 2.4-26). It was subjected to heat erosion mainly at the aft edge (along the X<sub>o</sub> 582 ring frame bulkhead) (figure 2.4-27). The pattern of deposited molten aluminum on the inboard side indicates that it was subjected to thermal flow aft to forward over the x-link (see arrows, figure 2.4-27).

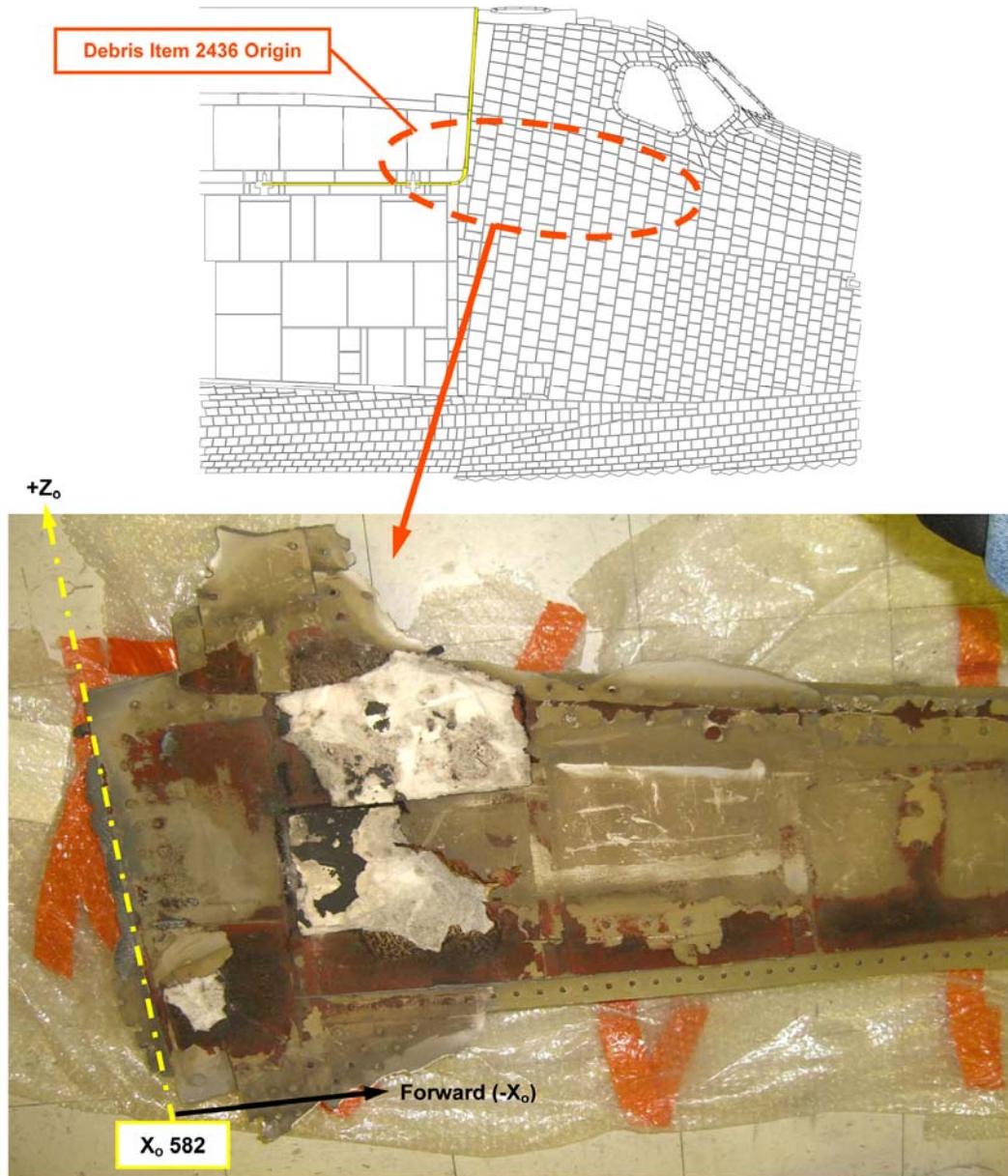


Figure 2.4-26. Starboard-side skin, view looking inboard, Columbia Reconstruction Database debris item no. 2436.

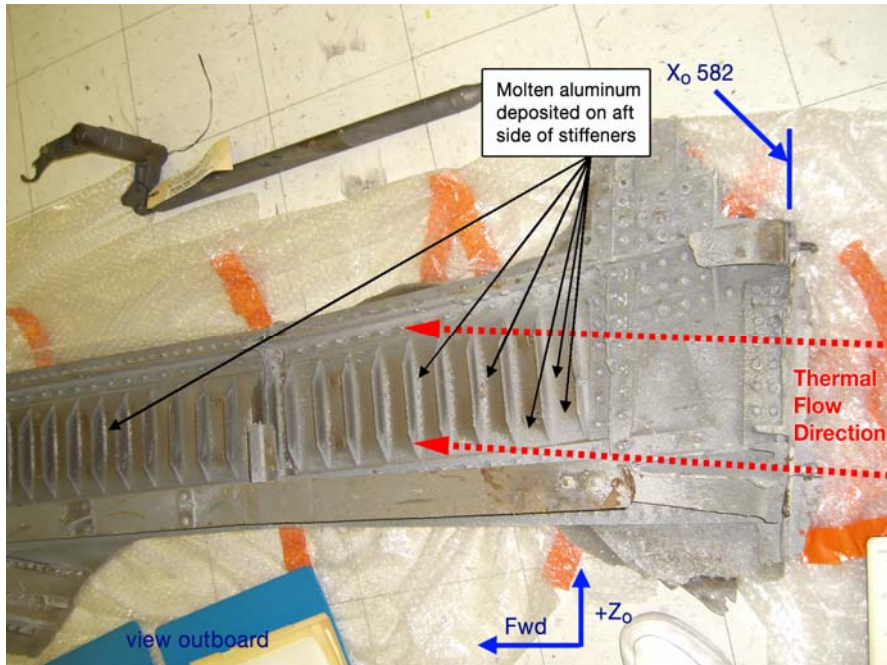


Figure 2.4-27. Inboard side of the starboard-side skin, Columbia Reconstruction Database debris item no. 2436.

This debris shows high heat erosion at the aft end while the remaining edges failed mechanically. The pattern of molten aluminum deposition indicates that the hot gas flowed mainly from aft to forward. If the thermal event happened after this panel broke away from the FF shell, all edges should experience a similar level of thermal damage, and the deposition of molten aluminum on the inside surface of the skin should have a random pattern instead of a directional pattern (figure 2.4-27). This suggests that this piece of FF skin was in place when the thermal event occurred. It is not known when this thermal event occurred. Since the forebody was rotating, the aft portion of the forebody may have periodically been presented to thermal flow for brief periods between the CE and the CMCE. The thermal event may also have happened around the CMCE, when the FF pulled away and exposed the area to thermal flow.

#### Y-LINKS

The y-links attach the aft bulkhead of the CM ( $X_o$  576) to the  $X_o$  582 ring frame bulkhead at the lower central portion of the bulkhead. It is possible that the two y-links remained intact at the CE, since most of the  $X_o$  582 ring frame bulkhead is believed to have stayed with the FF. After the CE, any Y-direction movement of the CM relative to the  $X_o$  582 ring frame bulkhead would exert high tension or compression loads on these links. Failure by tension is evident on the recovered debris of these links. The portside y-link shows that it also was softened by thermal exposure along with the tension failure. This portion protrudes beyond the  $X_o$  582 ring frame bulkhead, which would have been exposed periodically to hot gas flow following the CE as the forebody rotated (figures 2.4-28 and 2.4-29).

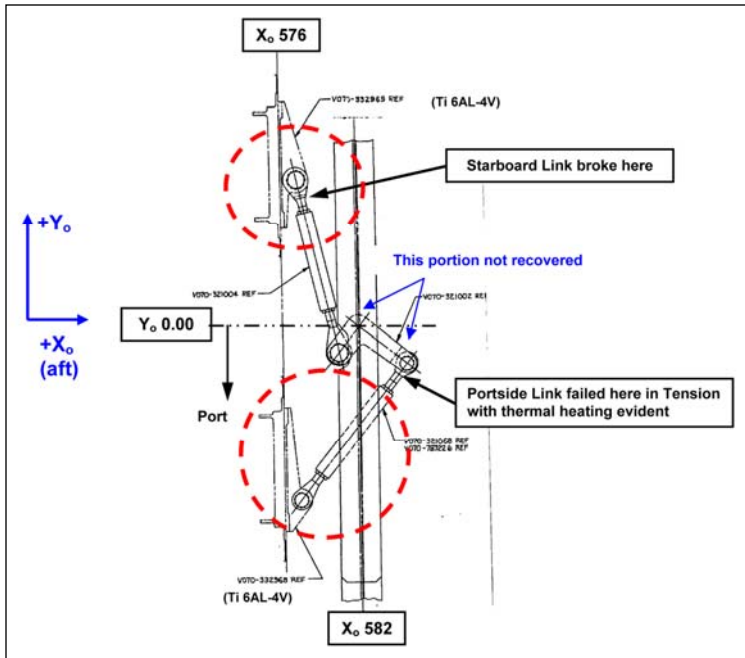


Figure 2.4-28. View looking from the top at the y-links.

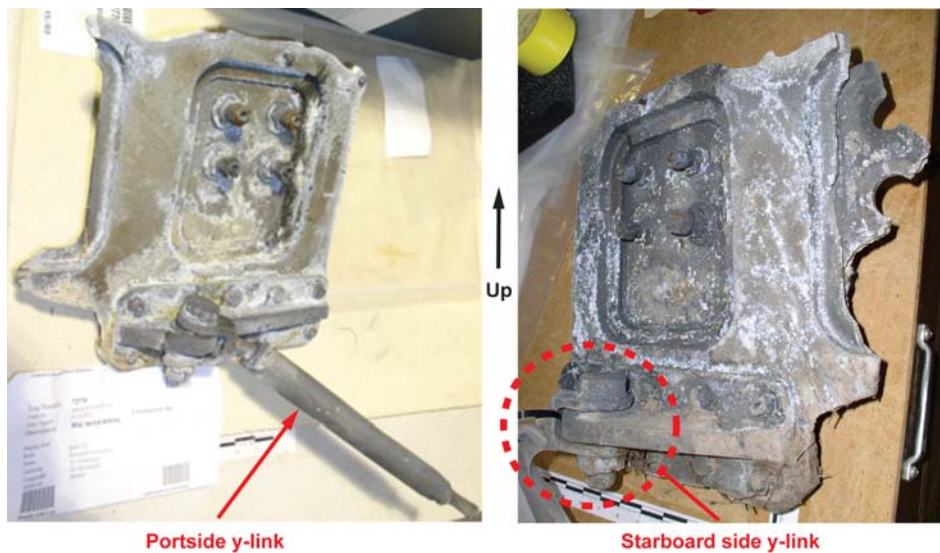


Figure 2.4-29. The y-link debris, still attached to the mounting on the  $X_o$  576 bulkhead, Columbia Reconstruction Database debris item nos. 72770 (left) and 9280 (right).

#### Z-LINK

The z-link failed at the attach point to the  $X_{cm}$  200 bulkhead (figure 2.4-30). The joint failed by a combination of fastener tensile failure and fastener insert pullout. Insert pullout requires thermal weakening of parent material because, by design, the insert is stronger than the fastener (under normal temperatures, the fastener should fail before the insert pulls out). Heating may have been occurring as the forebody rotated, allowing hot gas into the plenum between the CM and the FF. Failure resulted at the CMCE.

Alternately, after the FF separated, the  $X_o$  378 bulkhead may have remained in place attached to the  $X_{cm}$  200 bulkhead, connected by the z-link, and exposed to entry heating flow. The two bulkhead debris fields support this conjecture because the  $X_o$  378 bulkhead and the  $X_{cm}$  200 bulkhead debris fields overlap, with the  $X_o$  378 debris field being slightly west of the  $X_{cm}$  200 debris field. No ballistic analysis was done on either bulkhead elements to support or refute this conjecture.

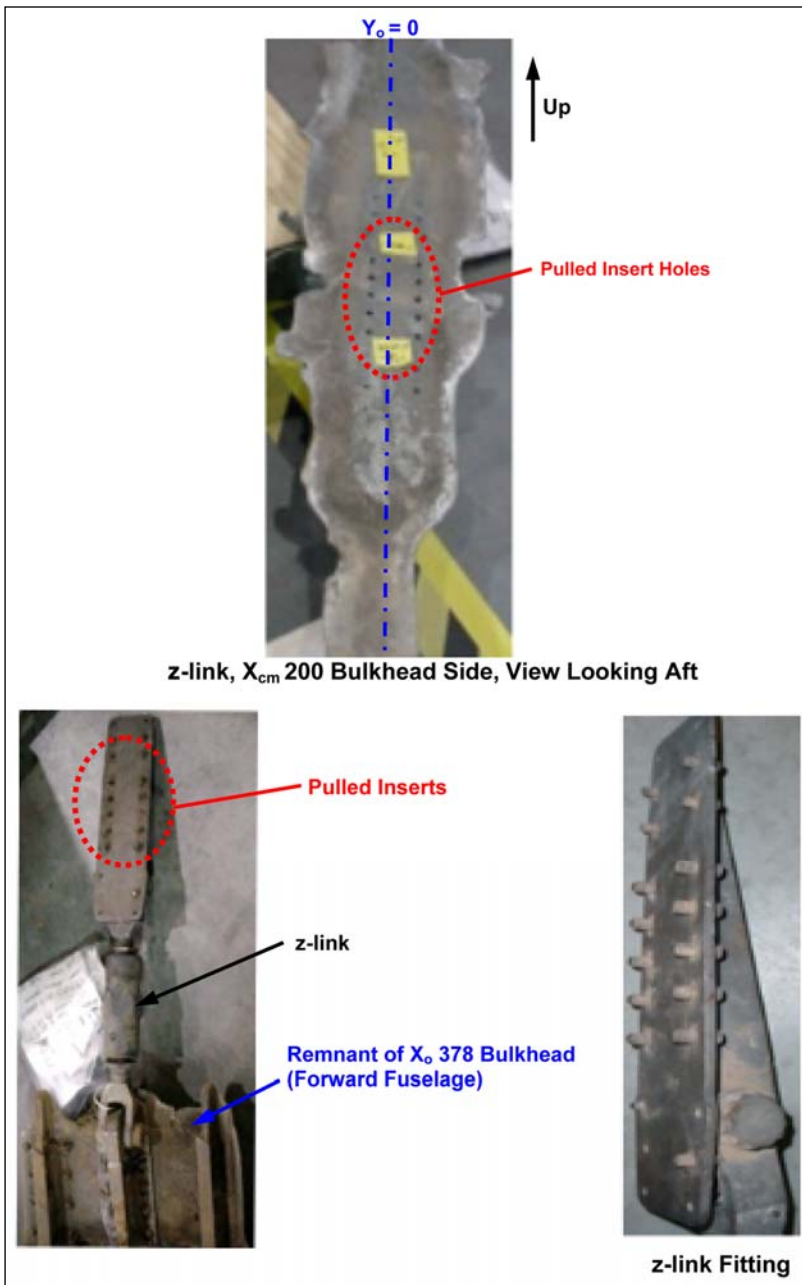
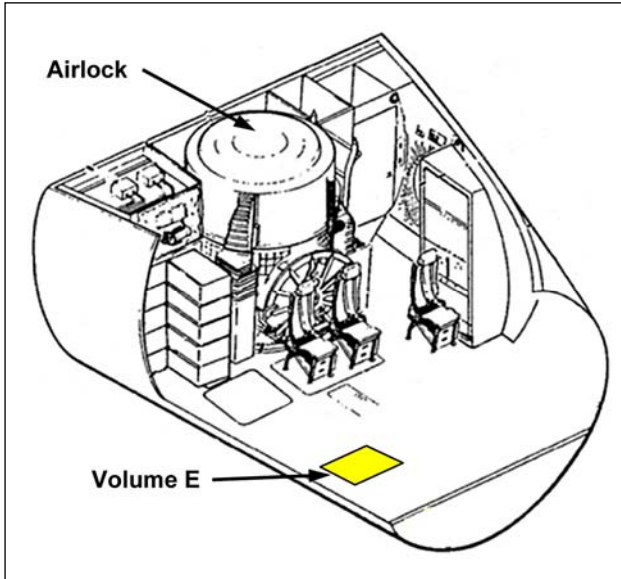


Figure 2.4-30. The z-link debris photographs, Columbia Reconstruction Database debris item no. 53828 (top).

#### Forward fuselage and crew module interaction at the catastrophic event

The cabin depressurization analysis (see Section 2.3) led to the conclusion that the cabin began to depressurize NET the CE (GMT 14:00:18) and NLT GMT 14:00:35; and probably depressurized through several small breaches. There is limited debris evidence to pinpoint locations for these breaches.

Items that originated from inside the CM and were recovered in the western portion of the debris field were reviewed to determine a potential breach area. These items included multiple STS-107 mission patches. Most of the mission patches were stowed in a middeck sub-floor stowage volume called Volume E. In-flight access to Volume E was not possible in the *Columbia* cabin configuration, so the crew could not have accessed the patches and stowed them elsewhere. Review of the stowage configuration documents for this compartment revealed that the patches were stowed near the bottom of Volume E. Therefore, the bottom portion of the Volume E structure had to be compromised to release the patches.



Volume E is a container with an opening on the top. The top part of this volume is a machined aluminum upper frame with a door, a hinge, and latches to cover the opening. Four sides and bottom panels are made of aluminum honeycomb core and aluminum facesheets. The upper edges of the side panels are attached to the upper frame vertical flanges by rivets. As illustrated by figure 2.4-31, the door of Volume E is at the level of the middeck floor. The upper frame of the box is attached to the floor beams by 18 Milson bolts and receptacles. The bottom of Volume E is tapered to match the curvature of the lower portion of the CM pressure shell.

Figure 2.4-31. View of middeck floor and Volume E, looking down and aft.

Detailed inspection of Volume E debris indicates that it was subjected to mechanical damage prior to thermal damage. The outer perimeter “picture frame” of the bottom panel was recovered and shows evidence of impact from below. Impact from the CM skin below Volume E would push the aft/outboard corner of the volume upward and then split the edge of the upper frame, as seen in the debris (figures 2.4-32 and 2.4-33).

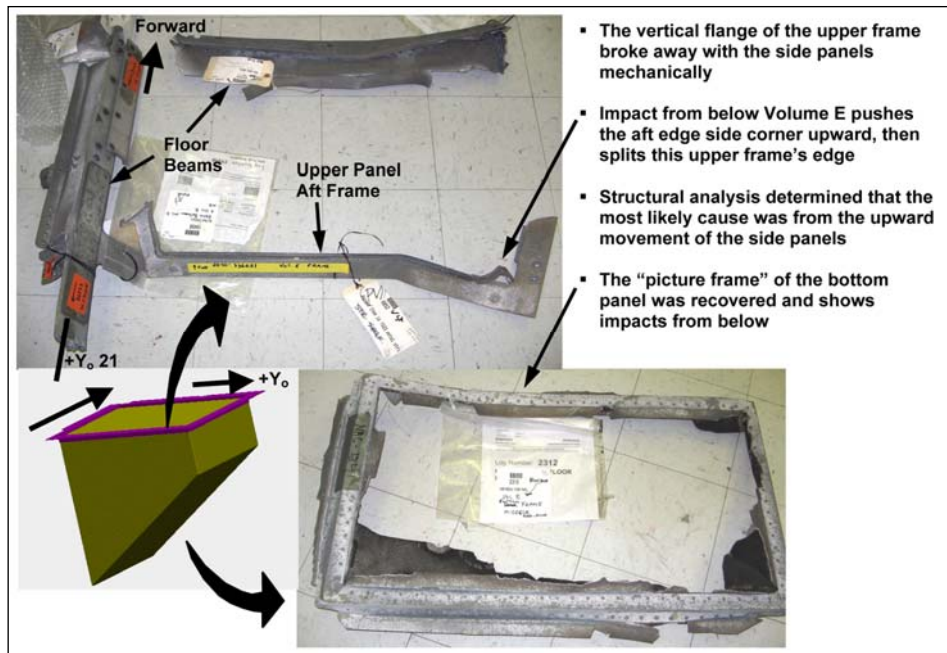
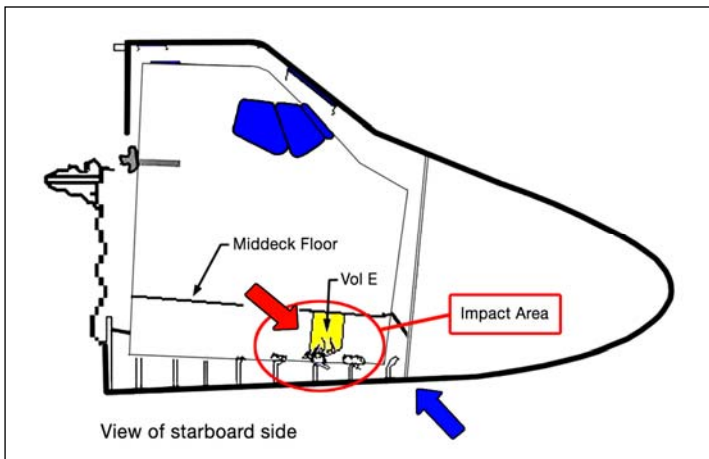


Figure 2.4-32. Volume E debris damage.



**Figure 2.4-33. Scenario showing how the crew module pressure vessel could impact the forward fuselage, and the middeck Volume E could impact the crew module pressure vessel, with resultant damage.**

Sudden changes to the rotation of the forebody complex probably occurred at the CE because of the asymmetric release from the mid-fuselage. Due to c.g. locations of the FF and CM, centrifugal forces would tend to pull one away from the other as the forebody rotated. The large portion of the X<sub>o</sub> 582 ring frame bulkhead was still attached to the FF. Thus, it and the other remaining attached linkages may have prevented the CM extraction from the FF.

It is likely that at or shortly after the CE, the FF structure impacted the CM skin below Volume E and, in turn, caused an impact between the CM skin and Volume E. The impact was severe enough to crack open the Volume E box, possibly near the lower portion, spilling some of its contents, including the patches. The patches then escaped the CM during CM depressurization.

The impacts under Volume E could possibly have breached the CM skin, providing a local vent path for the stowage volume contents such as the crew patch.

More impacts likely occurred as the forebody continued to rotate. From the CE to the CMCE, it is likely that the CM swung back and forth inside the FF, with both the CM and the FF experiencing impacts at multiple locations. The FF structures would have received damage, possibly creating paths for thermal inflow, as the forebody rotated. Impacts from the relative motion between the CM and the FF would damage the forward bulkheads (X<sub>o</sub> 378 and X<sub>cm</sub> 200), the fuselage frames, and the thinner areas of CM aluminum skin, star tracker well area, etc., depending on the attitude and the rotational movement. Recovered crew equipment debris also came from the forward lockers on the portside, not far from the star tracker wells, lending credence to this. Frame and bulkhead damage would destabilize the FF structures, perhaps popping open numerous items, including the star tracker panels, the TPS around the forward windows, the forward RCS module, the nose gear doors, and the side hatch outer layer. Review of forebody items found in the debris field prior to the main debris field support this conclusion, as portions of the nose gear, star tracker, and multiple tiles and portions of TPS made up this early released debris (figure 2.4-34).

Between the CE and the CMCE, it is not clear when the remaining links (z-link, four side links, and four side hatch links) failed. Obviously, sufficient integrity was maintained to hold the CM inside the FF.

#### **Mechanical and thermal degradation of the crew module pressure vessel between the Catastrophic Event and the Crew Module Catastrophic Event**

The airlock depressurized rapidly following the CE with the departure of the TAA (see Section 2.2.4). It might be speculated that rapid depressurization of the airlock with the interior of the CM still pressurized might implode the airlock structure. However, the airlock is intended for depressurization during spacewalk activities and its interfaces are reinforced. Empirical review of airlock structural capacity shows that implosion of the airlock is an unlikely scenario.

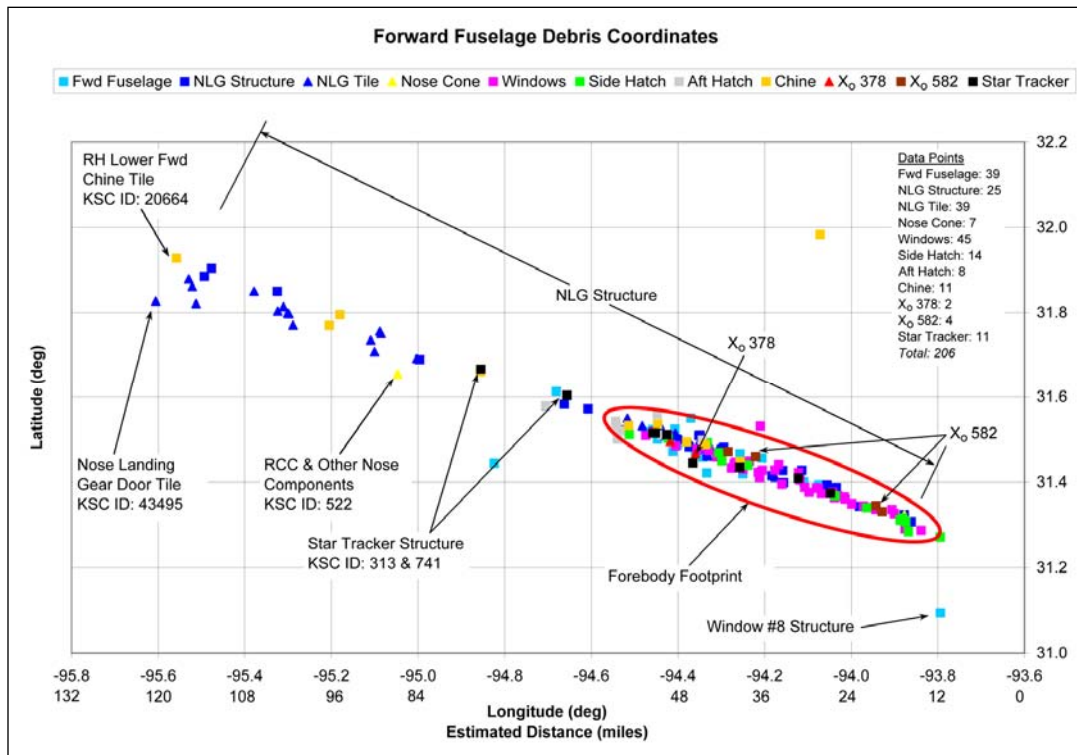


**Figure 2.4-34. Forward fuselage debris field showing tile, nose landing gear door structure, and star tracker door structure west of the main forebody debris field.**

Other warping as a result of the stresses of the CE cannot be ruled out. However, impacts as a result of the CM moving inside the FF appear to be the best candidate for mechanical breaches because they are the best supported by the debris field.

Thermal exposure of the CM pressure vessel may have weakened certain areas resulting in mechanical failure. This would not have happened immediately at the CE but would have taken time to develop as the forebody rotated, periodically exposing unprotected segments of the forebody.

The CM aft bulkhead was a clear immediate candidate for thermal breach since, unlike the rest of the CM, it was not protected by the FF and accompanying TPS. However, the bulkhead was extremely heavy, because it was made of aluminum waffle with additional reinforcing beams, and would act as a good heat sink. Debris field evidence does not support significant thermal erosion of the CM aft bulkhead prior to CM breakup.

There are gaps between the X<sub>o</sub> 576 bulkhead and the X<sub>o</sub> 582 ring frame bulkhead and directly over the x-links that would have allowed hot gas entry into the plenum between the forebody and the CM when rotation resulted in the aft forebody being presented to the directional thermal flow. Mechanical breaches resulting from the impacts of the CM and the FF could also have allowed thermal flow into the plenum if the breach were presented to the velocity vector.

The CM pressure vessel skin was designed with a main cone shape that has low thickness and minimized integral stringers to save weight (figures 2.4-35 and 2.4-36). Many large areas of the cone shape have uniform low thickness—as thin as 0.039 in. Skin thickness was controlled tightly by a chemical milling process during manufacturing. Because of low and uniform thickness, a large area of skin can be heated up quickly and uniformly. This can result in rapid thermal failure of the skin panel, and heat erosion can propagate rapidly.

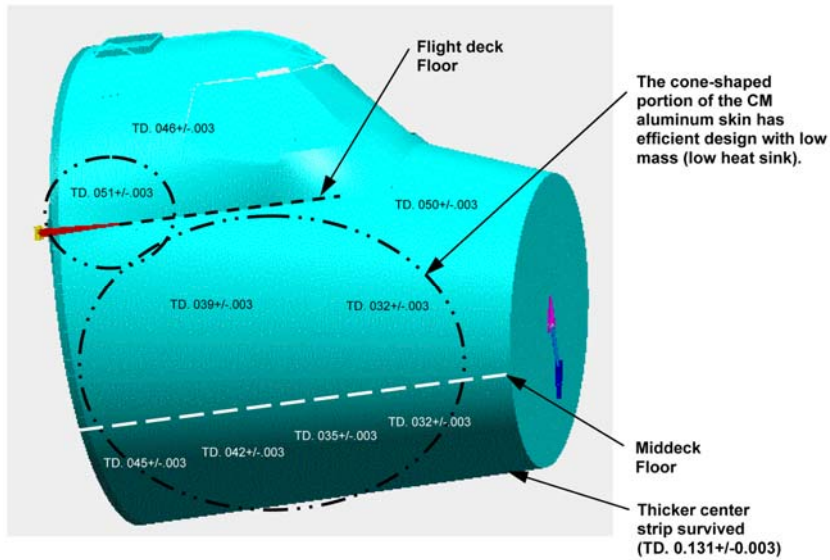


Figure 2.4-35. Crew module pressure vessel skin lightweight design. The thickness dimension (TD) is represented in inches.

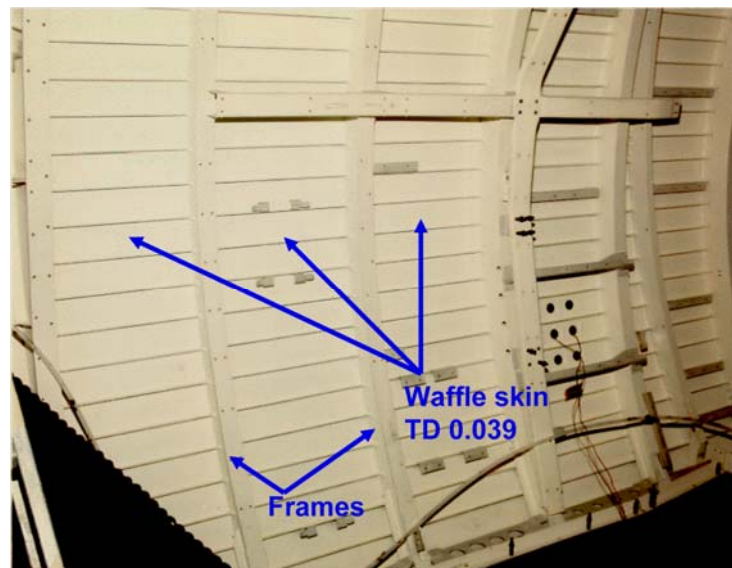


Figure 2.4-36. Typical crew module pressure vessel skin in middeck, looking outboard.

Very little CM skin structure survived. It is very thin, and probably melted quickly after breakup when exposed to entry heating. Only a relatively thicker region of skin strip (0.131-in. thick) along the bottom at the centerline was recovered in multiple pieces (figure 2.4-37).

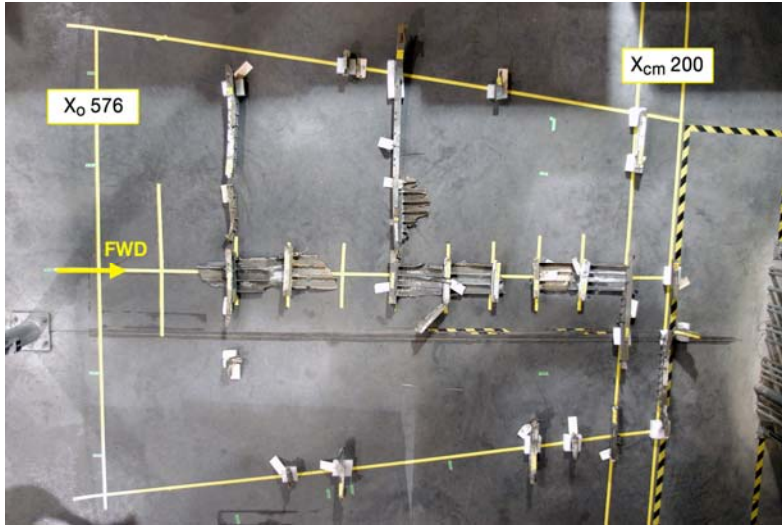


Figure 2.4-37. Recovered crew module pressure vessel base skin.

It is possible that areas of the CM skin were weakened or softened uniformly by thermal flow into the plenum between the CE and the CMCE. However, many recovered FF skin areas exhibited intact primer on the inner surfaces. This implies that most of the forebody TPS still remained to provide thermal protection on the outboard side of the FF panels before the FF breakup, and that the loss of CM pressure vessel skin was a result of exposure during the breakup after the CMCE.

#### 2.4.4.2 Crew Module Catastrophic Event/forebody breakup

##### Forward fuselage failure

It is unclear where the initial failure of the FF occurred. Loads due to deceleration of the forebody were increasing. Although much of the forebody was protected by the TPS of the FF, periodic exposure to heating was increasing as well.

The “arrowhead” skin/TPS panel between Windows 3 and 4 (debris item no. 65049) (figures 2.4-38 and 2.4-39) on the front of the forebody was recovered near the middle of the forebody debris field. It appears to have been torn on the portside and pulled through on the starboard side by mechanical loading, probably initiated by a relative movement between the port Windows 1 through 3 and the starboard Windows 4 through 6.



Figure 2.4-38. Forward fuselage arrowhead panel and the forward two windows, facing in.

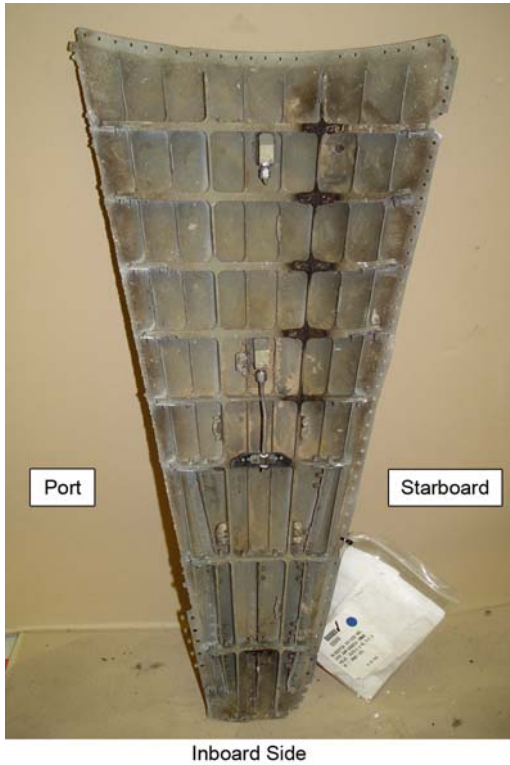


**Figure 2.4-39. Low-heat damage on the forward fuselage arrowhead panel, facing out, Columbia Reconstruction Database debris item no. 65049.**

The departure of the FF Windows 1 through 6 and the FF arrowhead panel would likely trigger the departure of the rest of the FF canopy by aerodynamic forces. This may have been the initiating event of the CMCE, or it might have been simply one event during the breakup. Without the upper FF half, the lower half would immediately peel away. This is supported by the video image, which shows what appear to be two large and symmetrically sized objects separating from the forebody at the CMCE.

Figures 2.4-40 and 2.4-41 are of the FF skin debris items that lie below the CM. Many panels have little molten metal deposition on the inside surfaces. Broken edges show little thermal damage, and some still have intact primer. This indicates that the plenum behind these areas was not exposed to long durations of thermal flow. Some skin pieces even had stringers that were removed mechanically. Most of the recovered skin debris appears to have mechanically fractured edges. Many forward RCS structural items were recovered; it appears that the forward RCS was pulled away mechanically and broke up into pieces with low thermal effects. The conclusion was that it is likely that the FF skin panel peeled away and broke up quickly.



**Figure 2.4-40. Lower forward fuselage skin and frame debris.**



**Figure 2.4-41. Lower forward fuselage skin panel near external tank attachment.**

### **Crew module breakup**

Unlike the FF, very little CM pressure vessel skin was recovered. The lack of thermal effects and interior deposition on the FF debris indicates that it was no longer with the CM when the pressure vessel skin melted. Once the FF separated, the CM would become highly susceptible to thermal heating, especially in the areas of low skin thickness. Multiple additional thermal breaches probably appeared on the CM skin within a few seconds because of the low heat sink and uniform thickness of the CM pressure vessel skin along the CM sides and bottom.

Failure modes that were assessed on the CM pressure vessel and secondary structural components suggest that fractures occurred subsequent to elevated temperature exposure (corresponding to a significant reduction of material properties). This clearly suggests that following FF separation, breakup of the CM structure occurred as a consequence of combined aerothermal heating and aerodynamic loading.

### **Middeck and forward bulkhead**

Figure 2.4-42 shows recovered CM forward bulkhead ( $X_{cm}$  200) debris on a grid that is the size of the original bulkhead. As described in the debris field cluster analysis, the CM forward bulkhead debris was recovered west of the aft bulkhead debris, and the middeck starboard debris was recovered west of the port debris. This suggests that the CM middeck starboard/forward was shed first and that the starboard and forward CM areas were exposed to higher heating first and/or faced the velocity vector at the time of the CM major breakup. The main CM breakup involved the departure of the middeck area, including the middeck floor and everything that was attached to that floor. Anything not firmly attached to the flight deck floor also came out with the middeck. Most equipment that was above and below the middeck floor was supported by the middeck floor; avionics bays are also supported by the side skins and bulkheads.

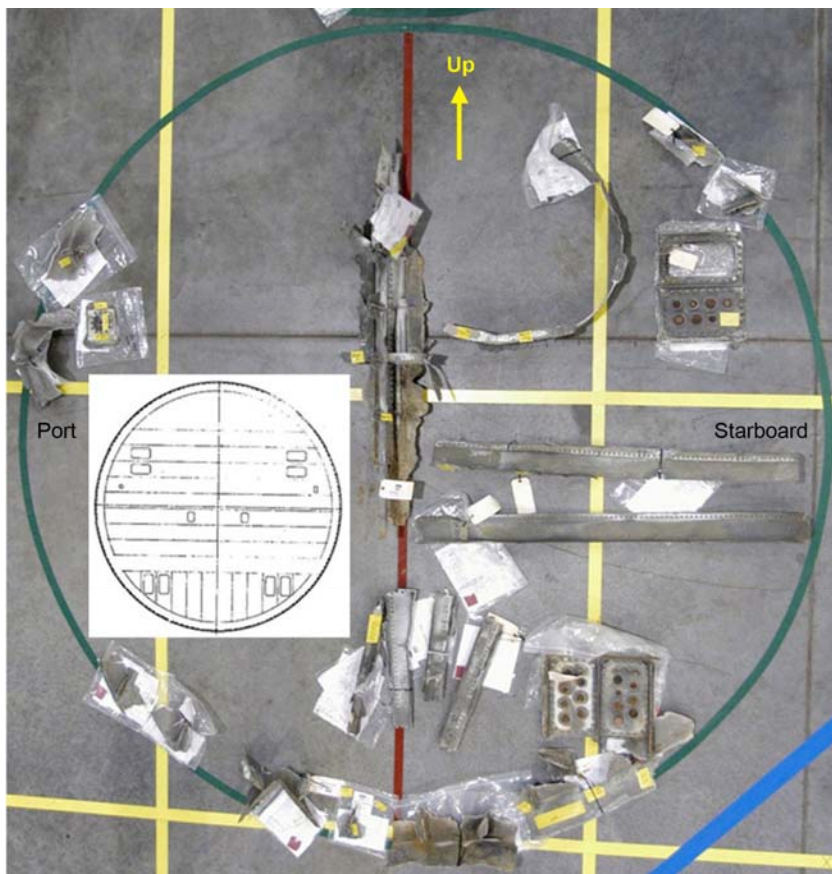


**Figure 2.4-42. View looking forward of the recovered crew module X<sub>cm</sub> 200 bulkhead debris.**

Structurally, the flight deck section is connected to the middeck section and the lower equipment bay is mainly connected by the CM side skin, avionics bay partitions, and the aft and forward bulkheads. The side skin and the forward bulkhead could be easily damaged by aerodynamic heating after the CM lost the protection from the FF shell. Therefore, as soon as the middeck side skin and forward bulkhead were compromised structurally, the lower half of the CM could have swung away from the flight deck portion by the effects of aerodynamic drag. It is likely that the whole middeck floor assembly came out together with the lower equipment bay. The hinge line appears to be at or near where the middeck floor attaches to the aft bulkhead. This motion would expand the middeck compartment (similar to opening a clam shell) and release all items attached to the middeck floor as well as other items stowed beneath that floor. Because the middeck floor disintegrated into many smaller parts without being significantly heated, it appears that the middeck floor failed as a result of structural loading. This may help to explain why more than 65% of the middeck floor was recovered without significant thermal erosion (figures 2.4-43 and 2.4-44).

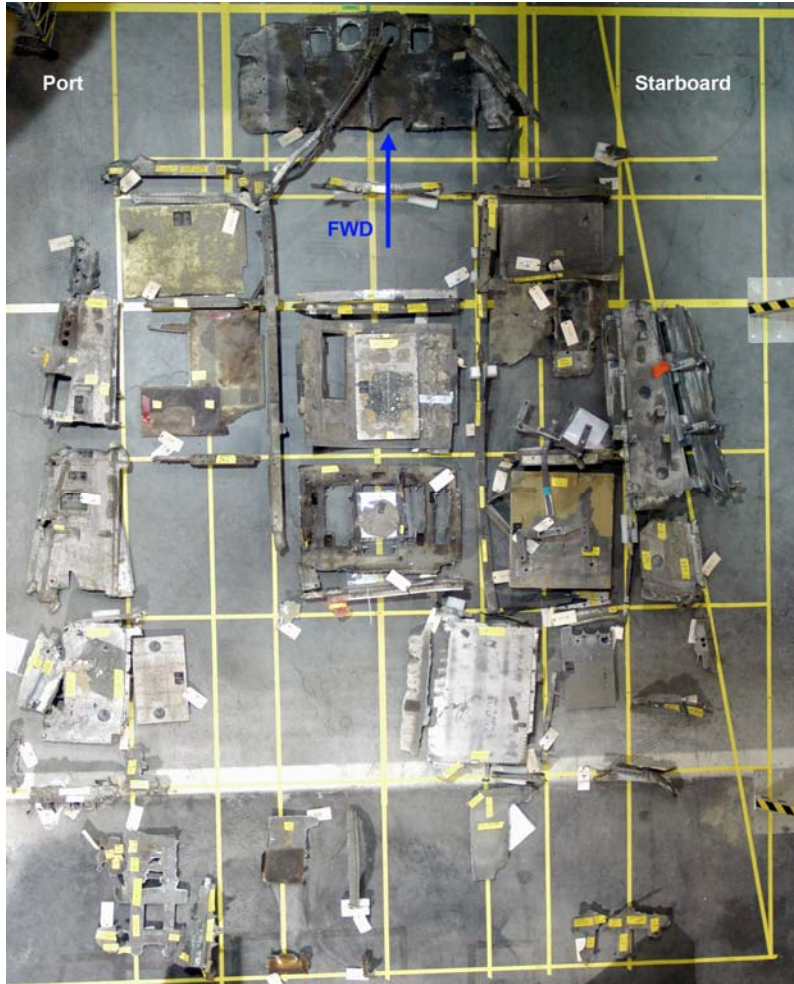


Figure 2.4-43. Top view of the crew module middeck floor debris.

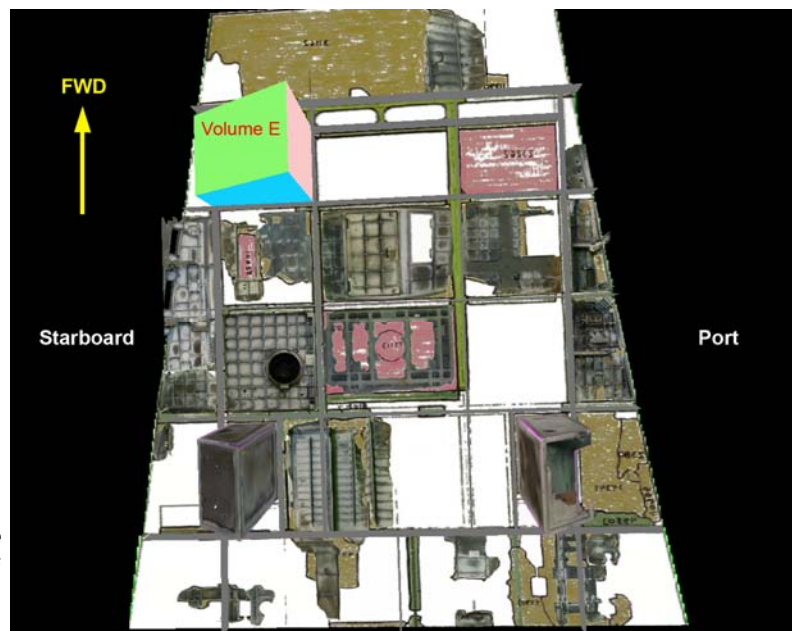


Figure 2.4-44. Bottom view of the recovered middeck floor items from virtual reconstruction.

The middeck floor and the lower equipment bay quickly disintegrated, with middeck floor panels, crew escape pole, MAR, and other crew equipment items (window shade bag, middeck lockers, sub-floor components, MADS/OEX recorder, etc.) departing quickly from the CM.

**Flight deck and aft X<sub>o</sub> 576 bulkhead**

The CM debris field suggests that after the forward bulkhead and the middeck floor departed, it was followed by the airlock, the flight deck, and the aft bulkhead. The flight deck floor debris exhibited much more thermal damage than the middeck floor debris.

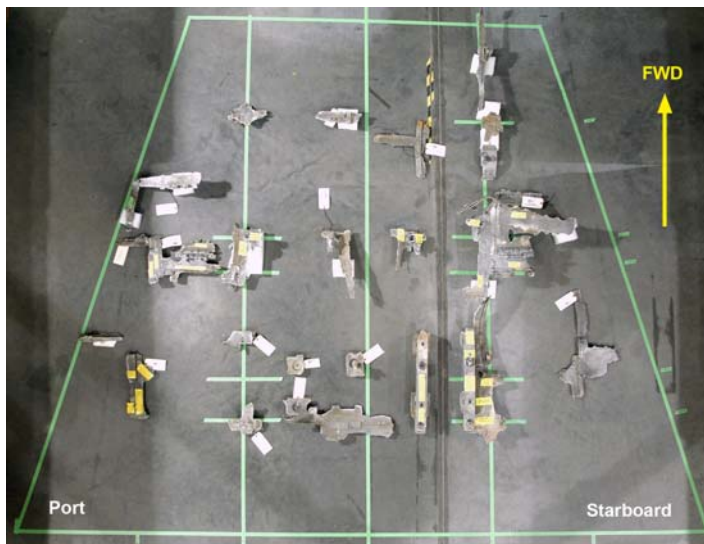


Figure 2.4-45. Top view of the crew module flight deck debris.

From the thermally eroded state of the flight deck debris, it appears that the flight deck stayed nearly intact for a period of time following the departure of the middeck area. This explains why so little of the flight deck floor was recovered (figure 2.4-45). Based on debris field evidence, the internal airlock, which was supported by the MAP (which is part of the X<sub>o</sub> 576 bulkhead), likely stayed together with the bulkhead and the flight deck.

Significant mechanical damage was noted on the starboard aft panels of the flight deck. These panels were recovered in much smaller segments than other flight deck panels. This suggests that the starboard side of the flight deck near the aft bulkhead (near the starboard x-link) experienced a more dynamic

failure than the portside. This may have resulted from structural degradation that occurred when the forebody separated from the midbody at the CE in this location. It is also consistent with a starboard-to-port failure for the middeck.

In general, heavy portions of the X<sub>o</sub> 576 bulkhead (including the MAP) survived the entry heating (figure 2.4-46). This is possibly due to the high heat absorption property of the aluminum bulkhead.

Some “T”-section stiffeners survived with little heat damage, possibly because of the early departure of these elements before the high thermal event that consumed the bulkhead.

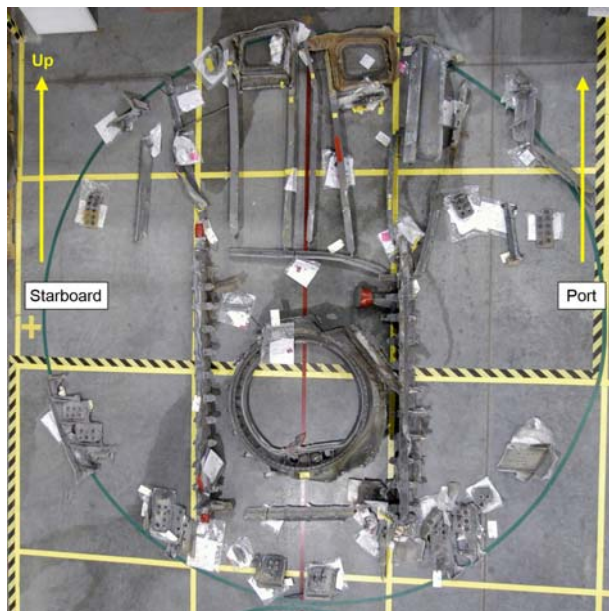


Figure 2.4-46. View looking aft of the recovered X<sub>o</sub> 576 bulkhead debris.

### Crew module crew equipment

The CM contains many items that were installed to facilitate the space shuttle crew's on-orbit operations. This equipment is generally termed "crew equipment" and includes the crew seats, middeck stowage lockers, the MAR, sleep stations, the galley, the WCS, the ergometer, the Crew Escape System (CES) pole, crew worn equipment, and loose equipment that was stowed in various locations. Attention was focused on the MAR and the CES pole because they have substantial attachments to the CM structure. Generally, the debris from the sleep stations, galley, WCS, ergometer, lockers, and loose equipment was highly fragmented and did not provide significant insight into the CM breakup. Analysis on those items was limited to identification and ballistics analysis on a few select items. Because the SPACEHAB module contained loose equipment that was stowed in middeck lockers, the SPACEHAB and the CM debris footprints both contained loose equipment and locker structure debris. Therefore, loose equipment and locker structure items were excluded from analysis on the SPACEHAB and CM debris footprints.

Recovery locations of suit and seat components indicate that the middeck crew members separated from the CM before the flight deck crew members. Additionally, flight deck seats experienced higher heating than middeck seats. These findings support the debris field cluster analysis conclusion that the middeck broke up before the flight deck broke up (see Sections 3.1 and 3.2).

### Middeck accommodations rack

The MAR is pinned to the port wall and the middeck floor forward of the side hatch and aft of the galley (figure 2.4-47) on the middeck. The MAR spans from middeck floor to ceiling.

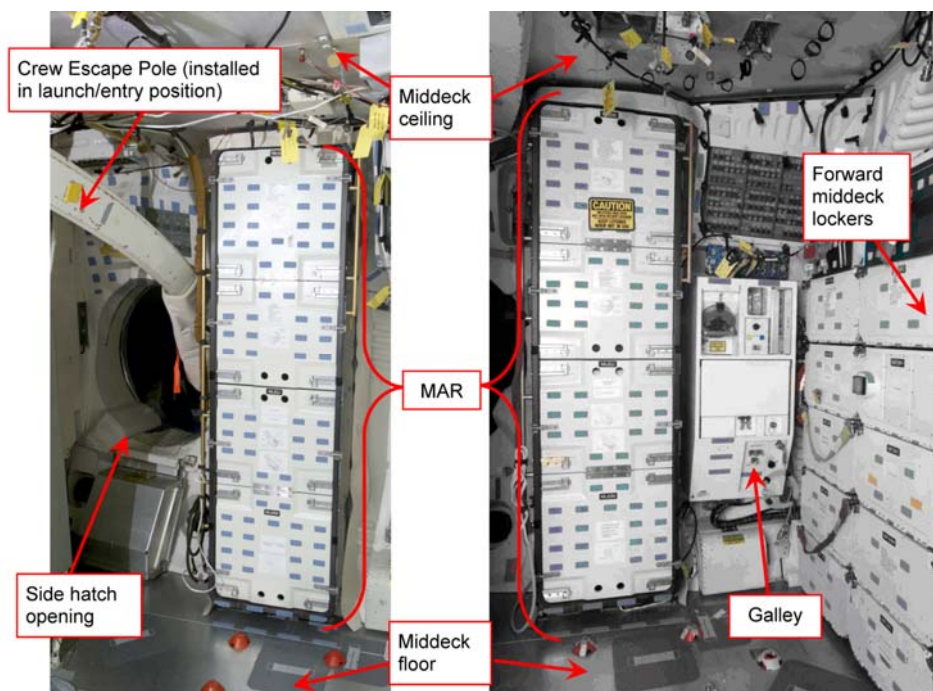


Figure 2.4-47. *Middeck accommodations rack.* [Picture from a shuttle training mockup in the JSC Space Vehicle Mockup Facility]

The MAR structure was made of a carbon fiber/epoxy composite with an aluminum honeycomb core. Two doors, which were hinged in the middle, face inboard into the CM, and were each held closed by eight locking spring latches. The MAR had two aluminum handrails that were attached to facilitate crew restraint and mobility. One handrail was mounted on the forward edge of the MAR and spanned from the top to the middle of the MAR. The other handrail was mounted on the aft edge of the MAR and spanned approximately three-quarters of the height of the MAR.

The MAR weighed 105 lbs. empty and could accommodate 12 ft<sup>3</sup> and over 200 lbs. of stowed items. Shelves could be bolted inside the compartment to subdivide the compartment. Stowed items were packed either in cargo transfer bags (CTBs) or foam cutouts to protect against damage.

For STS-107, the MAR contained payload general support computers (PGSCs), cables, a printer, the vacuum cleaner and attachments, medical kits, shuttle urine pretreat assembly (SUPA) hoses, and one can of LiOH. The total weight of the MAR (structure and return contents) was approximately 200 lbs.

Approximately 75% of the MAR structure was recovered, mostly intact. The blue areas in figure 2.4-48 represent the MAR structure that was recovered. The portions that were not recovered included the upper one-fourth of the MAR structure (including the upper attachment bracket), the top half of the upper door, a portion of the bottom half of the lower door, and the bottom surface of the MAR structure (including floor attachment brackets).

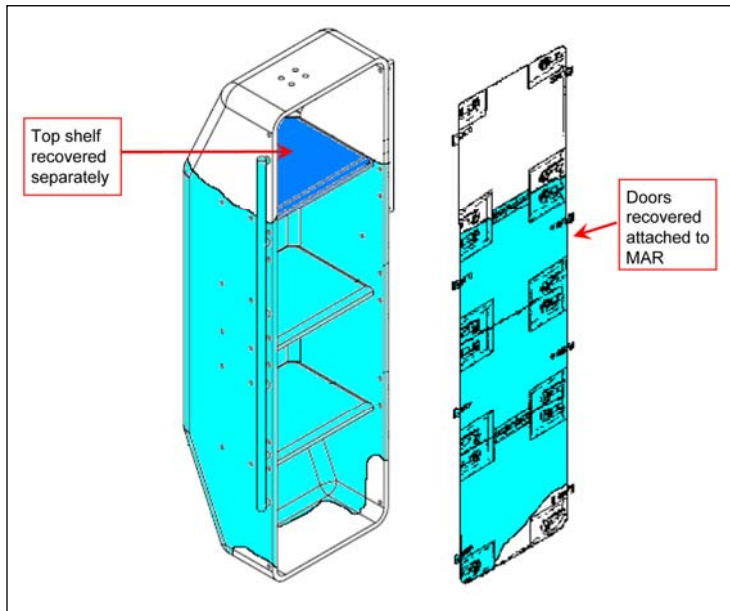


Figure 2.4-48. Recovered middeck accommodations rack structure (shown in blue).

The MAR was recovered with the middle and bottom shelves still attached. The top shelf was recovered separately. The lower door and the bottom half of the upper door were recovered with the MAR structure, as were the contents of the compartment between the middle and bottom shelves (CTBs with the printer and the vacuum cleaner (figure 2.4-49)). The contents of the compartment between the middle and top shelves and the contents of the compartment below the bottom shelf were recovered separately from the MAR structure and were highly fragmented.



Figure 2.4-49. Main middeck accommodations rack structure, as found.

The lack of impact witness marks on the MAR aft handle and the aft wall upper surface indicates that the MAR did not impact the CES pole, which is mounted just inches aft of the MAR. The lack of impact witness marks on the MAR starboard surfaces indicates that the MAR did not impact the seat 5 structure, which is mounted inches starboard of the MAR. Ballistic analysis indicates that the MAR separated from the CM shortly after the CMCE. Based on the failure of the fasteners securing the MAR attachment bracket to the middeck floor, it is concluded that the MAR separated from the middeck floor mostly to fully intact. These conclusions support the general findings that the middeck breakup was rapid and expansive, with very little interaction between major structures, and occurred at the onset of the CMCE.

**Crew escape system pole**

The purpose of the crew escape pole is to guide the crew member under the left wing when bailing out of the orbiter during controlled, gliding flight. For launch and landing, the escape pole is located on the middeck and is mounted to the starboard (right) ceiling and port (left) wall just forward of the side hatch (figure 2.4-50). During on-orbit operations, the escape pole is removed and stowed against the middeck ceiling.

The escape pole consisted primarily of a curved, spring-loaded telescoping aluminum cylinder and steel spring. It was contained within an aluminum housing. The complete assembly weighed 267 lbs. A magazine containing eight crew lanyards was attached to the port end of the pole housing near the side hatch tunnel (figure 2.4-51). In the event of a bailout, the orbiter side hatch is jettisoned pyrotechnically, the pole is deployed, and each crew member extends a D-ring and bridle from his/her parachute pack and attaches it to a snap hook on the outermost lanyard. As the crew member egresses the orbiter, the pole directs him/her beneath and away from the vehicle. Upon bailout, the forces on the lanyard and bridle initiate automatic parachute deployment.

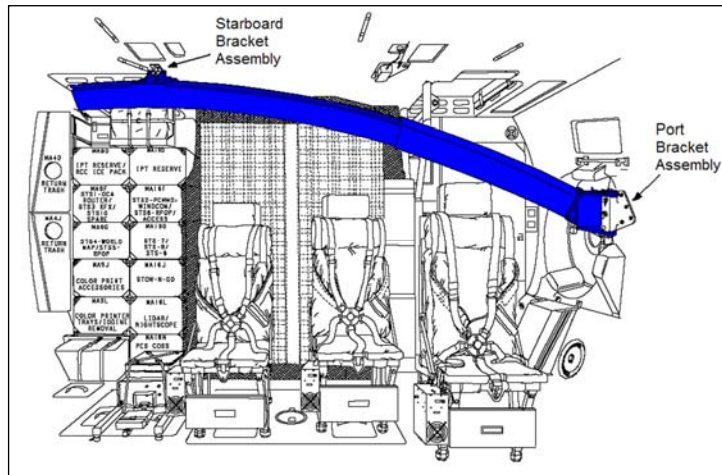


**Figure 2.4-50. Crew escape pole in launch/landing position, middeck, looking aft.**

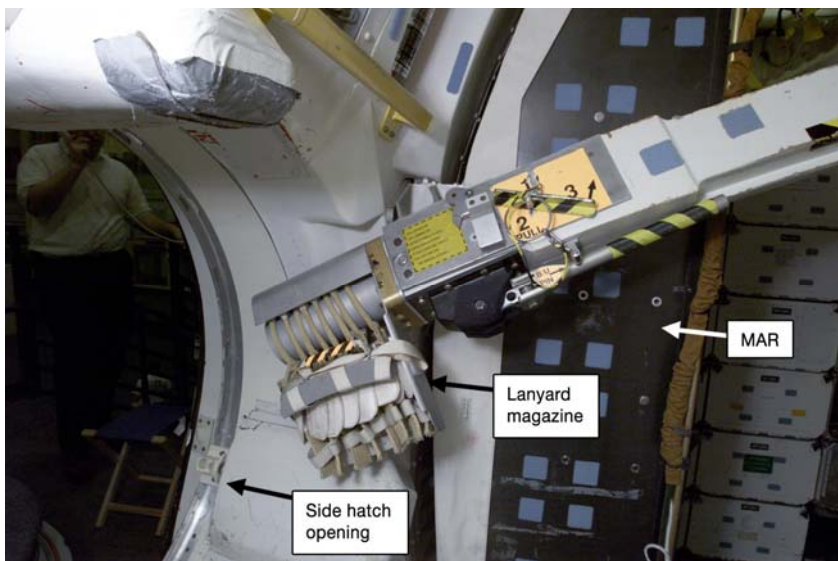


**Figure 2.4-51. Port end of the crew escape pole, showing lanyard magazine, middeck, looking forward. [Picture from a shuttle training mockup in the JSC Space Vehicle Mockup Facility]**

The SCSIIT database contains detailed information regarding the analysis performed on the CES pole and the conclusions made from the analysis. The conclusions and their relevance to the CM breakup are presented here.

The debris indicates that the pole was installed in the launch/landing position. There is no evidence to suggest that the pole had been deployed (or that the side hatch had been jettisoned<sup>3</sup>). The pole housing, the main pole, and the extension pole (figure 2.4-52) were recovered separately. The starboard end of the housing, including the middeck ceiling mounting bracket, shows evidence of thermal damage. The main pole and extension pole (figure 2.4-53) were recovered in relatively good condition, showing little mechanical or thermal damage. The main pole deployment spring was recovered separately from the housing, with the starboard end cap of the pole housing attached to the spring. Additionally, the portion of the CM port wall to which the pole attaches was recovered and analyzed. Several lanyards were recovered separately, but the lanyard magazine was not recovered.



Figure 2.4-52. Pole housing, main and extension poles.

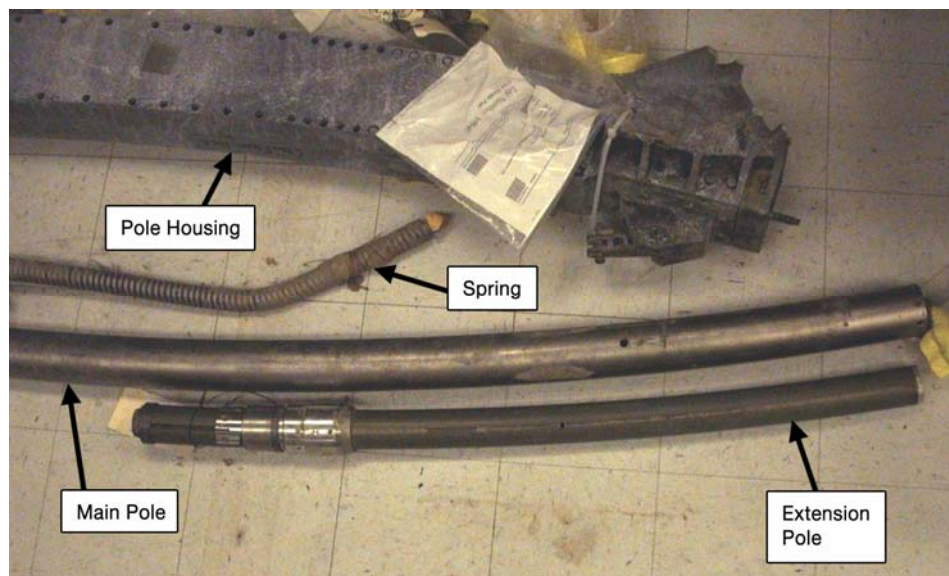
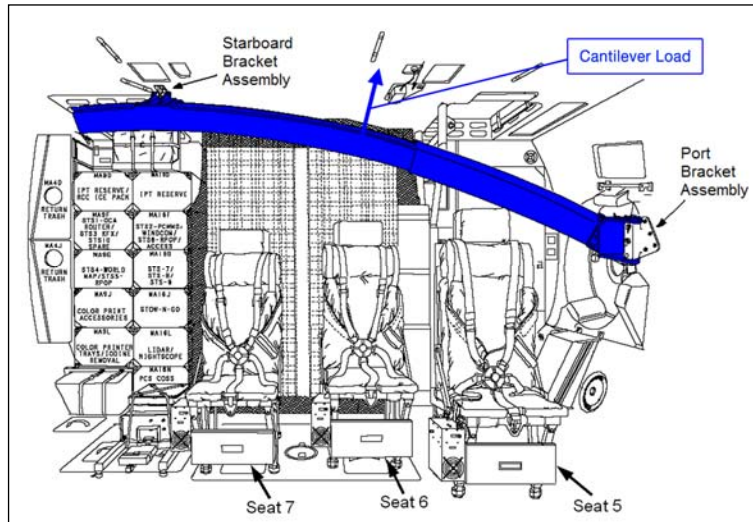


Figure 2.4-53. Port ends of housing, deployment spring, and main and extension poles.

<sup>3</sup>Several pyrotechnic components were recovered. All indicated that the hatch jettison system had not been activated.

Deformation of the upper portion of the knuckle that attaches to the CM indicates that it experienced an upward cantilever load (figure 2.4-54). This could be caused by the starboard end of the pole moving upward. This suggests that the flight deck separated from the middeck roughly at the flight deck floor/middeck ceiling level.



**Figure 2.4-54. Crew escape pole in launch/landing position, middeck, looking aft, with direction of cantilever load noted from debris.**

The relative lack of significant witness marks on the pole housing indicates that it experienced very few impacts. These conclusions support the earlier conclusions that the middeck breakup was rapid and expansive, with very little interaction between major structures.

### Flight deck instrument panels

Many of the flight deck panels were recovered and identified. Mechanical and thermal damage to the recovered panels was evaluated to assist in understanding the sequence of the breakup in an attempt to identify the location of the initial breach in the CM. Some of the panel parts were severely torn and deformed, yet some were mostly intact with less damage. Most of the recovered panels were photographed as orthogonally as possible under consistent lighting conditions, and the images were imported into a 3-dimensional computer model of the orbiter flight deck to create a virtual reconstruction of the flight deck (figures 2.4-55 and 2.4-56) (see discussion of virtual reconstruction in Chapter 4).



**Figure 2.4-55. Intact orbiter flight deck from the Shuttle Mission Simulator.**

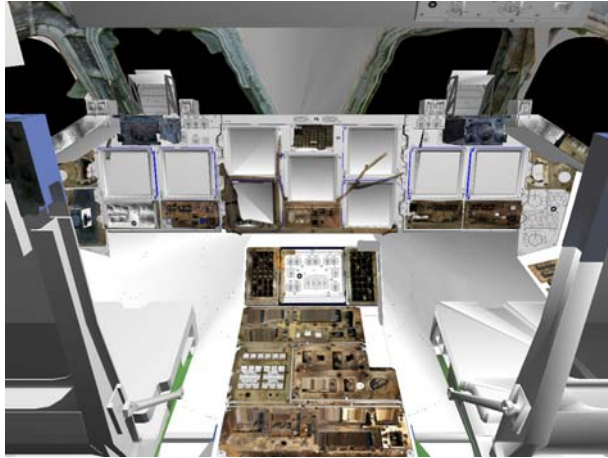


**Figure 2.4-56. Virtual reconstruction of the recovered Columbia flight deck panels.**

This virtual reconstruction was studied to investigate whether there were clear indications of a thermal or structural breach. However, adjacent panels were seen to have received significantly different amounts of thermal damage. This indicated that some panels broke off earlier than other panels, or were temporarily shielded from the thermal flow during the breakup. The damage varied greatly from one panel to the next, indicating a chaotic breakup sequence. No clear evidence of the initial breach location could be determined.

#### **2.4.4.3 Orbiter window analysis**

At least one window frame (CM or FF) was recovered from every window. Two large debris assemblies were recovered (figures 2.4-57 and 2.4-58). Each large piece is a complete assembly of three CM forward window frames (Windows 1, 2, and 3 and Windows 4, 5, and 6) with some broken glass pieces still captured in their retainers. Three CM window frames of Windows 7, 9, and 10 were recovered in separate pieces since they were not connected to each other by heavy CM skin structures (figure 2.4-59). Five thermal frames (FF) were also recovered.

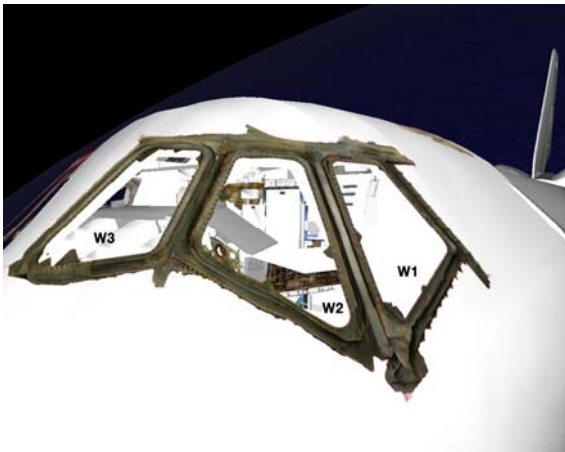


**Figure 2.4-57. Port view looking aft, recovered Columbia crew module Windows 1, 2, and 3.**

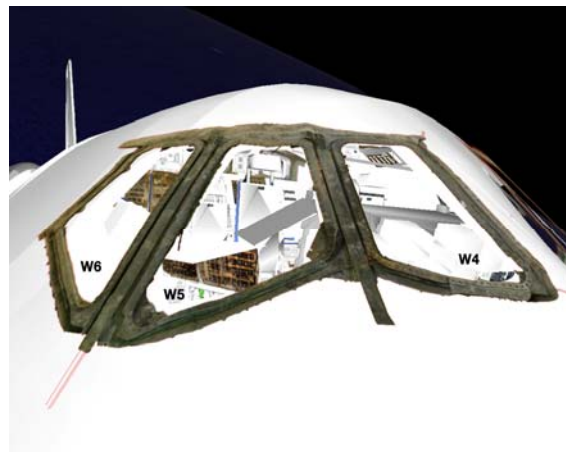


**Figure 2.4-58. Starboard view looking aft, recovered Columbia crew module Windows 4, 5, and 6.**

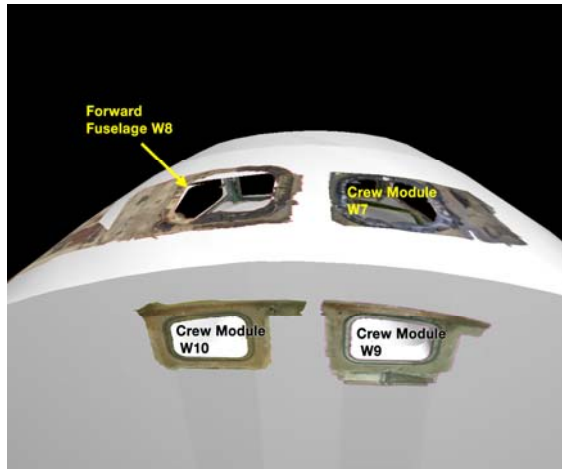


**Figure 2.4-59. View looking forward, recovered Columbia crew module Windows 7, 9, and 10 and forward fuselage Window 8.**

All CM window frames are heavily reinforced to limit the window retainer deflection when the CM is exposed to internal pressure load and flight loads. The redundant panes are also made from the same material as the outer thermal pane (fused silica) so that if the outer thermal pane failed, the middle redundant pane still could be able to take some limited thermal flow for a short time.

Debris evidence suggests that most of the CM skin structures surrounding the CM flight deck windows had been melted away during the event. One exception is the upper edge of CM aft Windows 9 and 10, which shows mechanical fracture edges.

To summarize previous conclusions, there is no evidence to suggest that failure of the CM window panes was the cause of cabin depressurization. The debris field shows that no glass from the redundant panes, which would have had to have failed to lose pressure, was recovered west of the main forebody debris field. Most of the loose glass from all panes was recovered from the main forebody debris field, suggesting that the windows shattered during the CMCE. The departure of the FF Windows 1 through 6 and the FF arrow-head panel may have triggered the departure of the rest of the FF canopy by aerodynamic forces.

The recovered glass showed a marked discoloration. Discussions with the window subsystem manager confirmed that the window appearance did not match the appearance of thermally discolored glass. Close inspection showed that the discoloration appeared to be deposited material. Analysis of the deposition on the glass was conducted to determine the sequence of events experienced by the windows.

Evaluation was restricted to only thermal (outer) pane glass from which the location was positively identified. Based on thickness, one piece of glass was identified as either Window 3 or Window 4, but for purposes of this assessment this was considered sufficiently specific. When possible, glass samples were obtained from what remained in the various window frames.

For purposes of this report, the deposition that coated the glass was referred to generically as the “char layer,” regardless on which window it formed. Because the char layer was suspected to have formed at relatively high altitudes and temperatures, it was presumed that it remained intact from formation through eventual ground impact. Therefore, it was assumed that the char layer was sufficiently adhered to the glass surfaces such that all lightly attached particles were either deposited later in the breakup sequence or were field contamination. The harvested samples were cleaned in a laboratory setting using standard preparation techniques. Figure 2.4-60 is an example of an extracted thermal pane in its cleaned state, prior to sectioning. Black lines on the images denote approximate sectioning planes.



**Figure 2.4-60. Window fragment removed from the thermal pane frame from Window 8. The black dashed line denotes the sectioning plane. The red dot was used to indicate the outward face of the pane.**

Various aspects of char layer characterization were performed by the JSC Materials and Processing Office, the JSC Astromaterials Research Office, the KSC Failure Analysis and Materials Evaluation Branch, and the White Sands Test Facility. Electron and light microscopy, X-ray diffraction, powder diffraction, layer metrology, and phase characterization were all performed.<sup>4,5</sup>

The char layer coverage observed on Windows 3, 4, and 5 appeared relatively translucent when placed in front of a light source. The coloration of the char layer from these samples varied from a brownish tan to a dark brown hue. The translucent characteristics of these samples implied a relatively thin deposit thickness. By comparison, samples from Windows 7 and 8 were notably opaque and had more of a blackened appearance. The surface texture of the window samples appeared relatively rough, consistent with re-solidified molten deposition. Visual examination alone was not able to assess the relative thickness of the deposits on Windows 7 and 8.

Cross sectioning of the various thermal pane window remnants was performed using standard cross-sectioning metallographic techniques. The char layer deposits on all thermal panes examined were evaluated and characterized based on mean thickness and constitution of the deposits (voids, inclusions, etc.). In general, the thermal panes for Windows 3, 4, and 5, were covered by a char layer deposit that ranged from a few microns ( $\mu\text{m}$ ) to nearly  $100\ \mu\text{m}$ . The deposit in the char layer for these forward-facing windows was not continuous; the areas without deposition retained their translucence. In the regions of continuous deposit, the thickness profiles were irregular, indicating sporadic deposition of the material. For regions where deposits were thick, void entrainment (porosity) was evident. In contrast to the exterior surfaces of the forward-facing windows, the exterior surface of the thermal panes for Windows 7 and 8 samples were covered by a char layer deposit that ranged from  $30\ \mu\text{m}$  to nearly  $500\ \mu\text{m}$  and appeared continuous. Although the char layers on these windows varied in thickness, the mean thickness was on the order of  $50$  to  $100\ \mu\text{m}$ . The measurements taken on the interior and fracture surfaces of Windows 7 and 8 samples were consistent with those of the forward-facing windows.

In-depth materials analysis was performed on the char layers for the forward windows to compare to the char layer on the overhead windows.

While almost every window sample contained multiple metallic species, aluminum was the predominant component of the char layer with other metal species existing in either discrete features or within a very narrow region of the layer. Interspersed in the layers were globules of silicon throughout the thickness. The spectroscopic signature indicated that the majority of this layer was a heavily oxidized aluminum amalgam consistent with a 2000-series aluminum alloy. This series aluminum alloy is used in the FF and CM structure.

A porous layer of aluminum was deposited on all window pane (forward and overhead thermal) samples, including both external and fracture surfaces. The porous nature of this feature in the char layer was considered to be a result of a dynamic process of deposition when the fragments of the glass, and the structure that contained them, possessed a high relative and turbulent motion to the deposition source. The deposition source, likely a 2000-series aluminum alloy and probably from the aluminum 2024 FF structure, was dispersed in the form of molten/semi-molten particles that partially cooled and/or oxidized prior to

<sup>4</sup>J. D. Olivias, L. Hulse, B. Mayeaux, S. McDanel, P. Melroy, G. Morgan, Z. Rhaman, L. Schaschl, T. Wallace, and C. Zapata, *Examination of OV-102 Thermal Pane Window Debris – Final Report*, KSC-MSL-2008-0178 (in press).

<sup>5</sup>J. D. Olivias, M. C. Wright, R. Christoffersen, D. M. Cone, and S. J. McDanel, *Crystallographic oxide phase identification of char deposits obtained from space shuttle Columbia window debris*, *Acta Materialia*, 2008 (in press).

impacting the glass substrate. Additionally, this feature of the char layer was irregular in thickness and also had distinct particles of other oxidized metal systems.

The formation of this porous char layer can be explained by several scenarios. The deposition source could have been nearby, but the area had highly turbulent relative motion. Or, the deposition source could have been a significant distance from the window, creating high dispersion in the molten material flow. This is less likely because liquid droplets would cool quickly and be less likely to adhere. Finally, the deposition could have resulted from the glass passing through a rapidly solidifying vapor surrounding the forebody as a result of thermal erosion of materials. It is conceivable that all three processes were occurring, either simultaneously or discretely. Given the debris field of recovered glass and the presence of the deposition on the fracture surfaces and inner panes, it is concluded that this deposition event occurred between the CMCE and the TD.

In addition to this porous layer, the two overhead thermal panes showed unique layers not seen on the forward windows. On these two panes, two additional layers, which contained titanium in appreciable quantities, were identified below the porous aluminum-rich layer. The overhead thermal pane window char was loosely characterized into three layers: a titanium-rich layer closest to the glass, a titanium-aluminum-rich layer, and the porous aluminum-rich layer that was described above. Crystallographic investigation of the titanium-rich region adjacent to the glass indicates that the nodules are consistent with  $\text{TiO}_2$ , a titanium oxide.

The aluminum-rich, thinner outer char layer appeared to be deposited via a different mechanism than the lower titanium-rich layers. Based on the lack of porosity, the environment in which the lower titanium-rich layers were deposited was likely substantially less dynamic than the environment during the deposition of the porous aluminum-rich top layer. This continuity of the titanium-rich layers suggested that the source was likely in close proximity to the windows; longer distances from the source would result in a more dispersed and turbulent flow, and probably result in material cooling/solidifying prior to impact on the window, which was not seen. The transition from titanium to a mixture of aluminum/titanium seems to imply that some time after the titanium began to deposit on the windows, aluminum from a nearby source also began to deposit on the windows. Analysis of the deposition on the carrier panel tile surrounding the overhead window panes showed similar deposition layer patterns. This deposition occurred prior to the breakup of the windows and structure, which was presumed to have begun at the CMCE. The existence of this distinctive three-zone char layer only on the exterior surfaces of the thermal panes from Windows 7 and 8 also supports the previous debris field finding that the windows were largely intact through the CMCE.

The previous findings were considered interesting enough to lead to a search for the source of the titanium and aluminum. The intention was to discover whether there was any information that was suggestive of the structural condition and the orientation of the forebody prior to the CMCE. A search for forward structures containing titanium showed that the nearest source of titanium material to the windows was the forward PLBD rollers. These rollers are made of titanium and aluminum with an Inconel sleeve. The PLBDs of the orbiter, when closed, rest on these roller mechanisms, which are attached to the X<sub>o</sub> 582 ring frame bulkhead upper arch in the forward part of the payload bay. These rollers are in close proximity to Windows 7 and 8. The structure that supported the roller components was primarily composed of 2024 aluminum alloy and also displayed evidence of significant thermal erosion. However, regions farther away from the rollers showed minimal signs of thermal erosions; green Koropon primer was still present on portions of these remote regions (figures 2.4-61, 2.4-62, and 2.4-63).



Figure 2.4-61. Endeavour, OV-105, X, 582 ring frame bulkhead arch with rollers. Circled in red is one of the eight rollers.

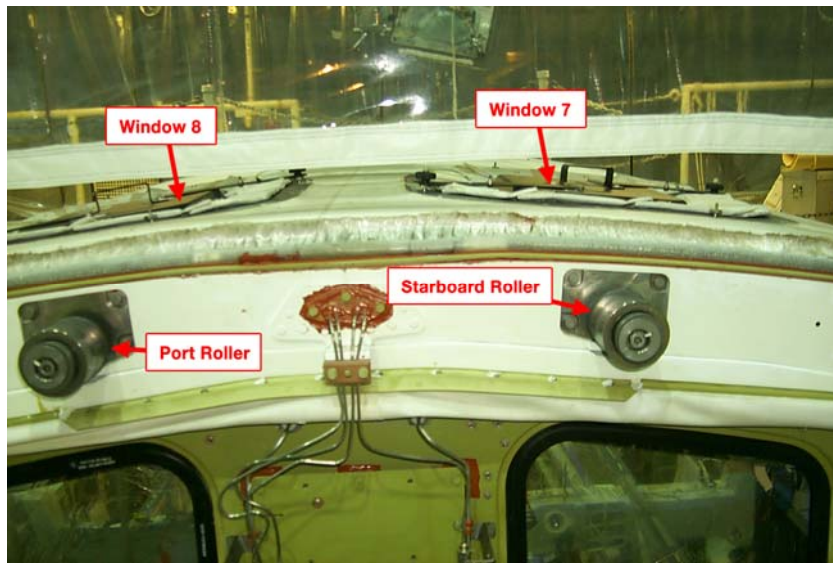


Figure 2.4-62. Nominal configuration (Endeavour, OV-105) of the two inner rollers and overhead windows.

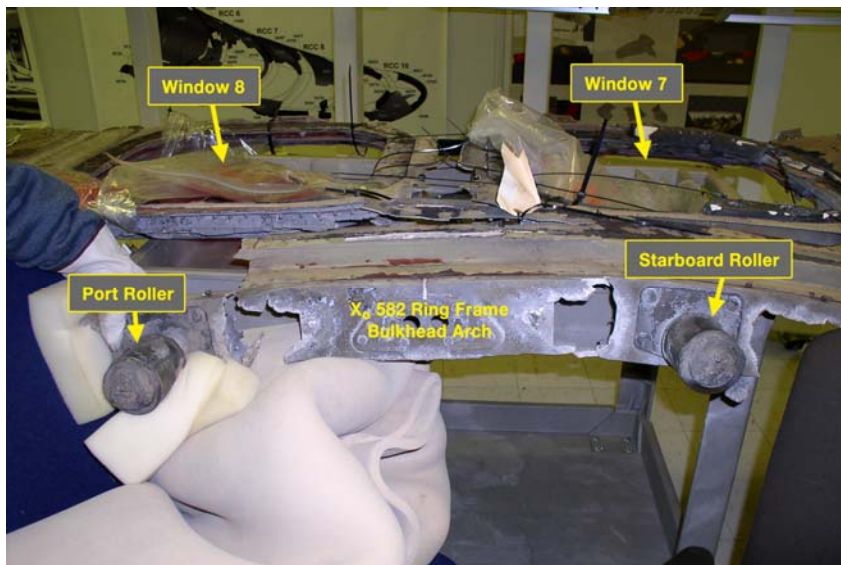


Figure 2.4-63. Columbia debris for same location. Note eroded rollers and eroded region of the X, 582 Ring Frame Bulkhead Arch.

The recovered rollers for the location closest to the overhead windows both showed significant signs of erosion. While these rollers were not the only components made of titanium, they were the only ones recovered that possessed the proper material, proximity, and thermal indications and were, therefore, concluded as the source location. Given these findings, the rollers were the most probable source of titanium causing the deposition on the windows.

Since the rollers are located on the X<sub>0</sub> 582 ring frame bulkhead arch aft and below these two windows, and protected by the PLBDs, the PLBDs must have been compromised or fully departed while the bulkhead arch was still attached to the CM. Additionally, the forebody must have been traveling aft-end forward for some period of time to have the directional thermal flow that caused the titanium to “vaporize” flow over the glass external surface of the thermal panes or on the external surface of the Windows 7 and 8 redundant panes, it can be concluded that the thermal panes were intact at the time of this event. This is consistent with other findings showing that the FF remained with the CM until breakup of both elements.

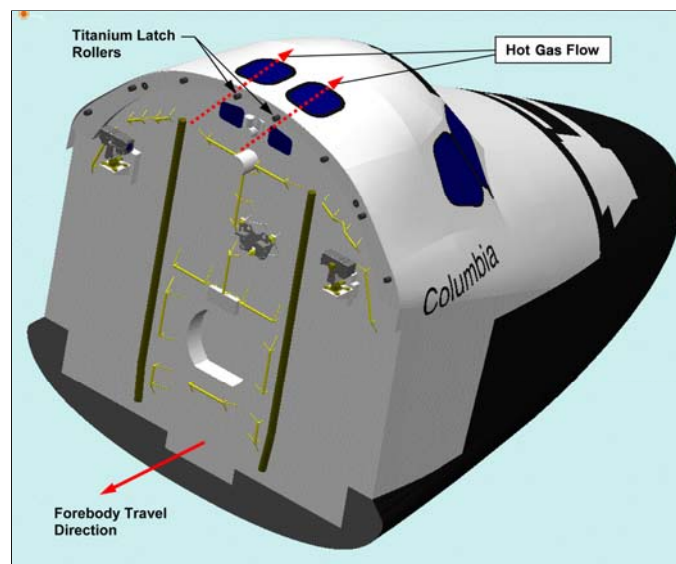


Figure 2.4-64. Titanium deposit on windows indicates forebody traveled backwards.

**Finding.** Windows 7 and 8 experienced a titanium deposition event that occurred prior to window breakup.

**Finding.** The most probably source for the titanium deposition on Windows 7 and 8 was the PLBD rollers. These rollers were not exposed to heat flow until after the PLBDs were compromised.

**Finding.** All the windows had an aluminum-rich deposition, which was consistent with a turbulent process.

A complete discussion of the thermal mechanisms that may have led to the titanium deposition is covered in Section 2.1.6.8.

## 2.4.5 Synopsis of forebody breakup sequence

The orbiter breakup (CE) or subsequent impacts between the CM and the FF caused small mechanical breaches on the CM skin. The FF shell stayed with the CM until the CMCE at GMT 14:00:53. At the CMCE, the FF most likely separated in two large segments, upper and lower. The departure of the FF arrowhead panel and FF Windows 1 through 6 may have triggered the departure of the rest of the FF canopy by aerodynamic forces.

Once the protective FF structure departed, the CM side skin was consumed by thermal exposure. Breakup of the CM structure occurred as a consequence of aerothermal heating and aerodynamic loading. The CM broke up with the middeck and forward bulkhead departing, most likely from starboard to port. The middeck breakup was rapid and expansive, with very little interaction between major structures.

The flight deck remained intact for some period after the middeck separated. The flight deck likely remained with the airlock and the aft bulkhead. As a relatively intact “pod” with a high ballistic number, the flight deck experienced more thermal exposure until its final breakup completed the CMCE.

The forebody was broken down to subcomponents that were too small and dispersed to see on video at GMT 14:01:10. This was described as the TD. Cascading failures and thermal damage were still occurring, but the CM no longer had any structural integrity at this time.

**Recommendation L3-1.** Future vehicles should incorporate a design analysis for breakup to help guide design toward the most graceful degradation of the integrated vehicle systems and structure to maximize crew survival.



# **Chapter 3 – Occupant Protection**

***3.1 Crew Seats***

***3.2 Crew Worn Equipment***

***3.3 Crew Training***

***3.4 Crew Analysis***



## 3.1 Crew Seats

The seats, which are the interface between the vehicle structure and the crew members, provide a source of data for the accelerations and thermal environments that the crew members experienced. This section provides background information on the design and construction of shuttle crew seats, and describes the detailed analyses performed on the *Columbia* crew seats. These analyses included review of the recovered videos recorded on orbit, review of the materials analyses performed by the *Columbia* Accident Investigation Board (CAIB)/Crew Survival Working Group (CSWG), and inspection of debris items including microscopic inspections of the inertial reels mechanisms and straps.

The following is a summary of the findings, conclusions, and recommendations for this section:

**Finding.** Evidence from the inertial reel straps indicates that the seats 1, 2, and 3 straps were mostly extended at the time of strap failure. The seats 4, 6, and 7 straps were extended during a material deposition period (seat 4 at least 8 in., or ~36% extended; seat 6 at least 21.25 in., or ~96% extended; and seat 7 at least 21.5 in., or ~98% extended). Medical evidence (see Section 3.4) indicates that some of the crew members received injuries consistent with insufficient upper body restraint.

**Conclusion L2-2.** The seat inertial reels did not lock.

**Conclusion L2-3.** Lethal injuries resulted from inadequate upper body restraint and protection during rotational motion.

**Recommendation L1-3/L5-1.** Future spacecraft crew survival systems should not rely on manual activation to protect the crew.

**Recommendation L2-4/L3-4.** Future spacecraft suits and seat restraints should use state-of-the-art technology in an integrated solution to minimize crew injury and maximize crew survival in off-nominal acceleration environments.

**Recommendation L2-8.** The current shuttle inertial reels should be manually locked at the first sign of an off-nominal situation.

**Finding.** The seat 2 inertial reel strap exhibits “strap dumping” failure features. The strap failed progressively, possibly due to damage to the lateral edge of the strap from contact with the sharp edge of the strap pass-through slot.

**Recommendation L2-5.** Incorporate features into the pass-through slots on the seats such that the slot will not damage the strap.

**Finding.** All inertial reel straps are tested with static loads at room temperature. Load testing has not been conducted to determine the loads required to fail the straps at elevated temperatures or under dynamic loads. Testing has not been conducted to determine the material properties (combustion vs. chemical degradation vs. melting) in a high-temperature/low-oxygen (O<sub>2</sub>)/low-pressure environment.

**Recommendation L2-6.** Perform dynamic testing of straps and testing of straps at elevated temperatures to determine load-carrying capabilities under these conditions. Perform testing of strap materials in high-temperature/low-oxygen/low-pressure environments to determine materials properties under these conditions.

**Finding.** While all seat piece-parts include serial numbers, only the serial numbers of the inertial reels were recorded and tracked to a specific seat assembly. The lack of configuration management documentation hindered the process of ascribing the seat debris items to specific seat locations.

**Recommendation A5.** Develop equipment failure investigation marking (“fingerprinting”) requirements and policies for space flight programs. Equipment fingerprinting requires three aspects to be effective: component serialization, marking, and tracking to the lowest assembly level practical.

### 3.1.1 Seat design and construction

Two types of seats are used on the space shuttle. The Pilot seats are used by the mission Commander (CDR) and Pilot (PLT), and Mission Specialist seats are used by all other crew members. Both types of seats provide for crew member positioning and restraint during launch, entry, and some on-orbit operations. Both types of seats are also designed to accommodate a fully suited crew member.

Seat positions are numbered 1 through 7, beginning with the CDR’s position on the flight deck (seat 1) and ending with the starboard-most Mission Specialist seat on the middeck (seat 7). Seats 1 through 4 are on the flight deck (figure 3.1-1), and seats 5 through 7 are on the middeck (figure 3.1-2). Seats 1 through 5 are flown on all missions. Seats 6 and 7 are flown as required.

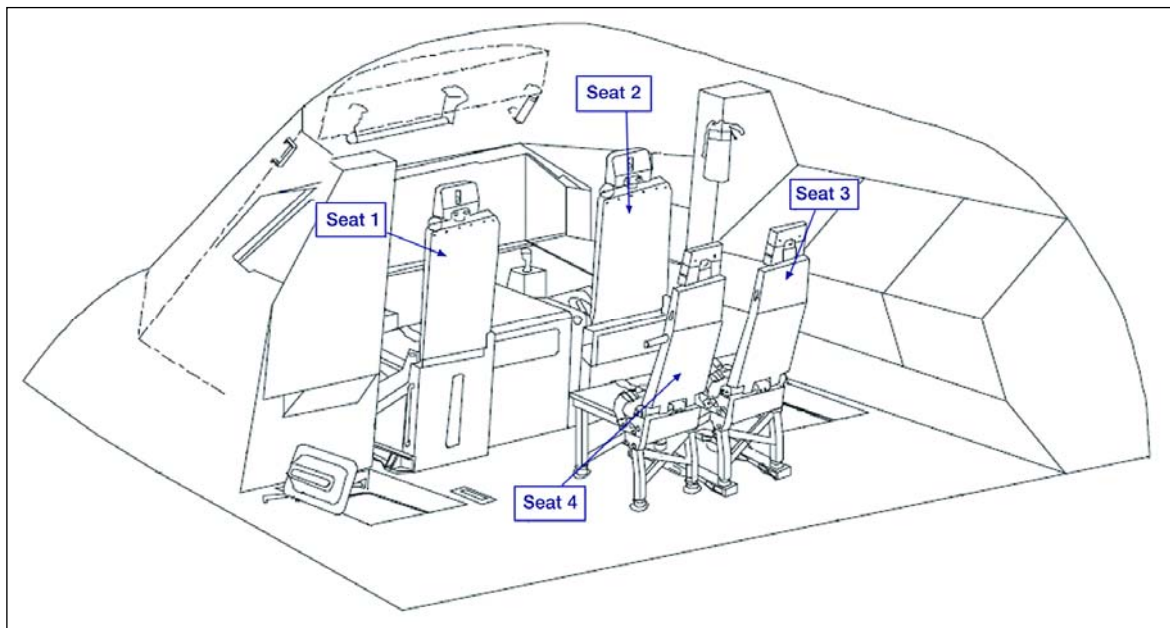


Figure 3.1-1. Depiction of the flight deck seats.

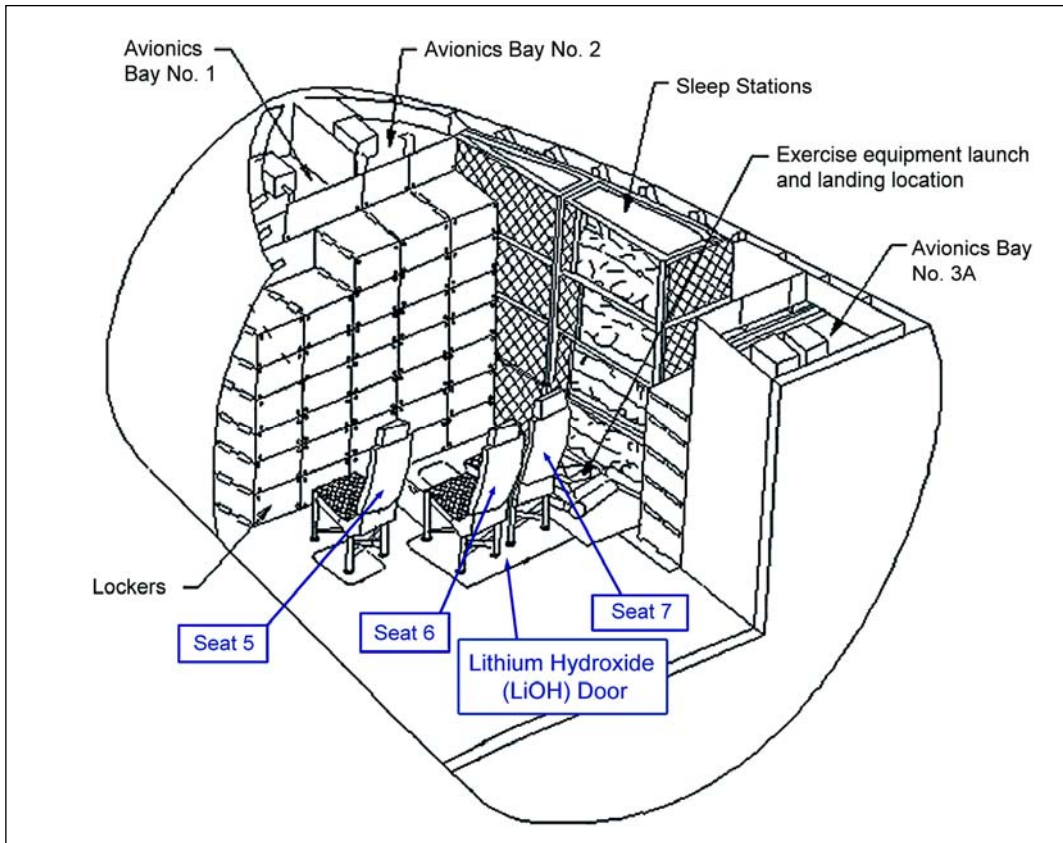


Figure 3.1-2. *Depiction of the middeck seats.* [Adapted from the Shuttle Crew Operations Manual]

The Pilot seats (figure 3.1-3) and Mission Specialist seats (figure 3.1-4) have several common design features. Both seat types have identical seatbacks, five-point restraints, headrests, and MA-8 inertial reels (a part of the restraint system).<sup>1</sup> The five-point harness restrains the upper torso with shoulder belts, and the lower body with lap and crotch belts. All belts connect to a rotary buckle that is permanently mounted to the crotch belt. The shoulder belts join to a single strap, the inertial reel lead-in strap, which attaches to the inertial reel mechanism mounted inside the seatback. The inertial reel will lock automatically due to accelerations pulling the strap out at 1.78 G to 2 G. A lever to manually lock and unlock the inertial reel is located on the left side of the seat pan. Both seat types accommodate the attachment of O<sub>2</sub> hoses and communications cables, and both have attachment brackets for cooling units used in conjunction with the crew member suits for crew member comfort.

<sup>1</sup>The MA-8 inertial reel is an off-the-shelf design used in military helicopter seats and was not designed specifically for the orbiter.

Figure 3.1-3. *Pilot seat.* [Adapted from the Space Shuttle Systems Handbook]

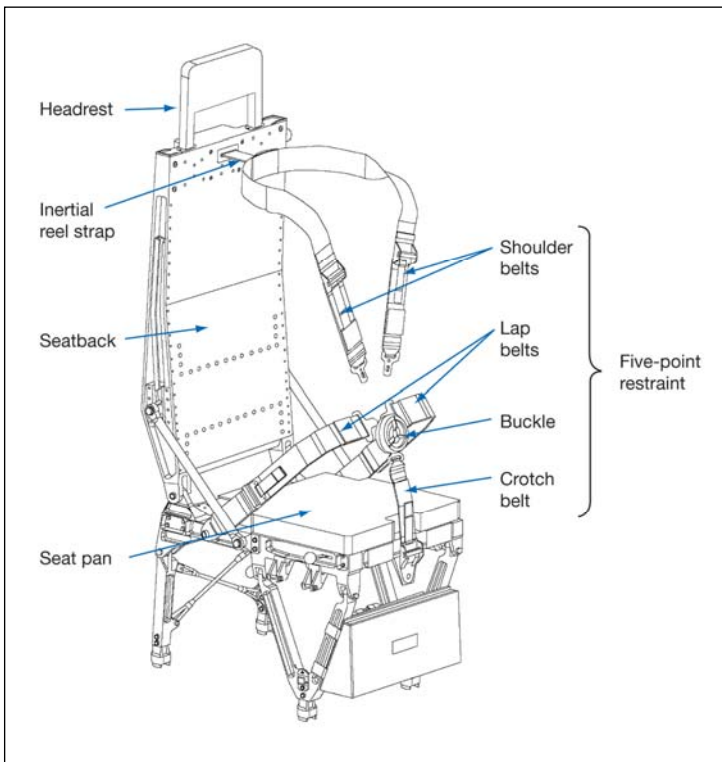
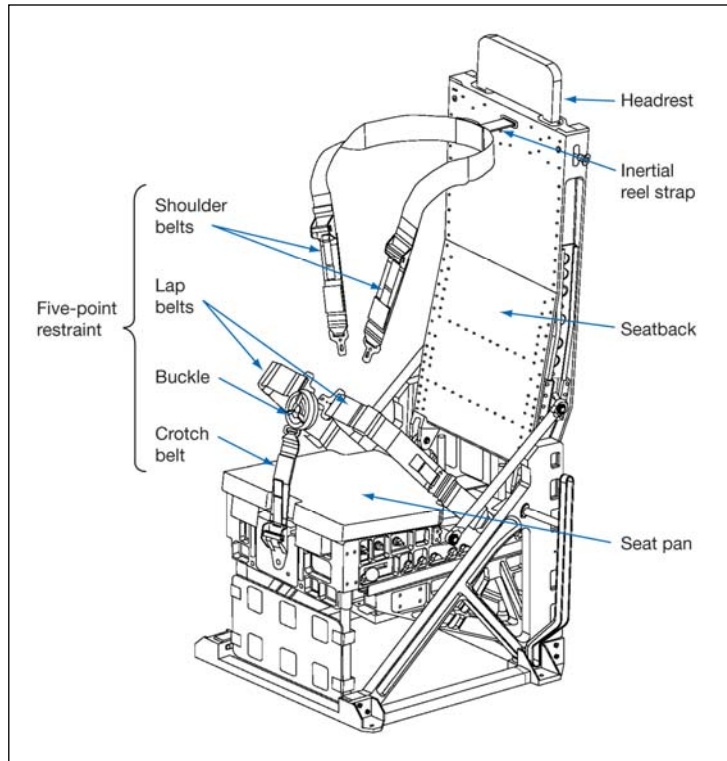


Figure 3.1-4. *Mission Specialist seat.* [Adapted from the Space Shuttle Systems Handbook]

The seat pan and base of the Pilot seats (seats 1 and 2) differ from the Mission Specialist seats. The Pilot seat base is permanently mounted to the flight deck floor and incorporates mechanisms providing up/down and forward/aft adjustability of the seat position. The Pilot seats also provide a mounting base for the rotational hand controllers (RHCs) (figure 3.1-5). RHCs are control sticks that are used by the CDR and PLT to control vehicle rotation about the roll, yaw, and pitch axes during ascent, orbit, and entry. The RHCs

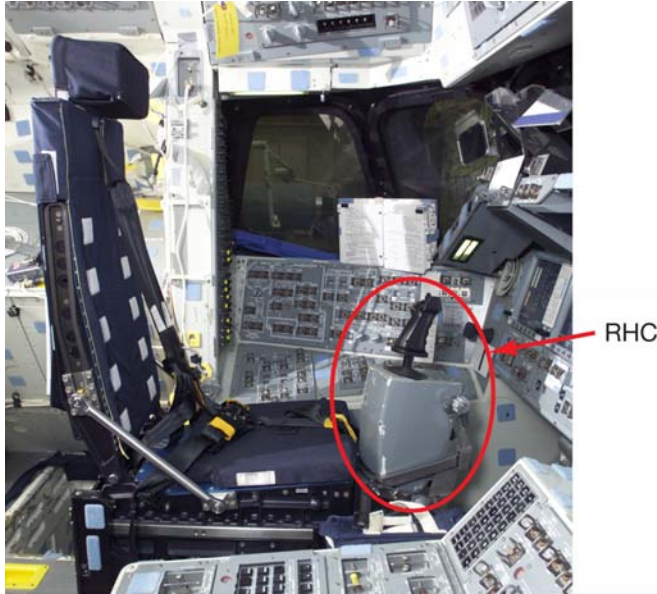


Figure 3.1-5. Commander's seat and one of the rotational hand controllers, flight deck. [Picture from a shuttle training mockup in the JSC Space Vehicle Mockup Facility, looking from starboard to port]

provide input to computers to actuate various vehicle control effectors (aero-surfaces and/or Reaction Control System (RCS) jets)).

Crew members assigned seats 3 through 7 use the Mission Specialist seats for launch and entry. Five Mission Specialist seats were flown on STS-107. Seat 3 was mounted on a special sled assembly that was unique to *Columbia*.

The Mission Specialist seats have no base, but have foldable legs attached to the seat pan. The legs are equipped with quick-disconnect fittings to allow for seat removal and stowage. Once the shuttle is on orbit, all Mission Specialist seats are detached from the floor, folded, and stowed in various locations depending on crew preference. During deorbit preparation, the crew reinstalls the Mission Specialist seats.

### 3.1.2 STS-107 seat configuration

The recovered middeck and flight deck videos revealed information that was related to the configuration of the crew seats and other flight crew equipment. The recovered middeck video recorded deorbit preparation (D/O PREP) activities on the middeck. Although there is no credible timestamp<sup>2</sup> on the video, the STS-107 crew plan<sup>3</sup> offers some insight into when the recording probably occurred.

The video shows that all middeck seats were installed. The seat 5 crew member is suited, and the seat 1 and seat 6 crew members are donning their suits. Based on the crew D/O PREP plan, this 30-minute video probably recorded events from approximately Greenwich Mean Time (GMT) 11:40:00 to approximately GMT 12:10:00.

The recovered flight deck video is a 13-minute, 11-second video with sound that was recorded more than 1 hour after the middeck video described above. This video recorded entry events on the flight deck from approximately GMT 13:35:34 to GMT 13:48:45. It shows that all of the flight deck seats were installed and the flight deck crew members were properly restrained. This video provides a good view of the crew members in seats 1 and 2, and fair views of the crew members in seats 3 and 4. It also shows that all of the flight deck crew members were properly secured with seatbelts to prevent floating from the seats (tight lap belts). No slack in the belts is visible in the shoulder harnesses, and the crew members are able to move their upper bodies, indicating that the shoulder harness inertial reels are not locked, which is normal at this point during the mission.

<sup>2</sup>The video has no air-to-ground audio, nor does it record any actions that can be time-verified through telemetry or on-board data recorders, so a precise time-stamp cannot be determined.

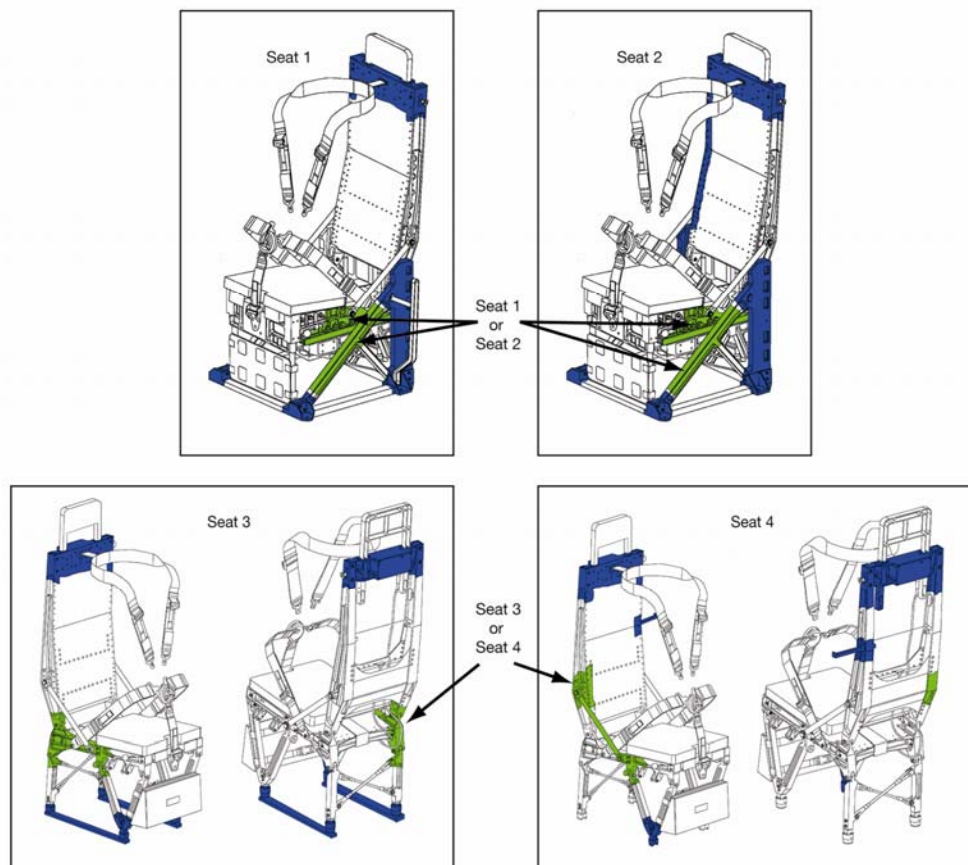
<sup>3</sup>Pre-mission, each shuttle crew develops a detailed deorbit preparation plan that is tailored from the formal Flight Data File procedures.

From video evidence, investigators concluded that all of the seats were installed and the flight deck crew members were properly strapped into their seats. Although no recovered video shows that the middeck crew members were strapped into their seats, medical findings and evidence in the seat debris described below confirms that two middeck crew members were fully strapped in and that one middeck crew member was at least partially restrained in the seat.

### 3.1.3 Seat structure

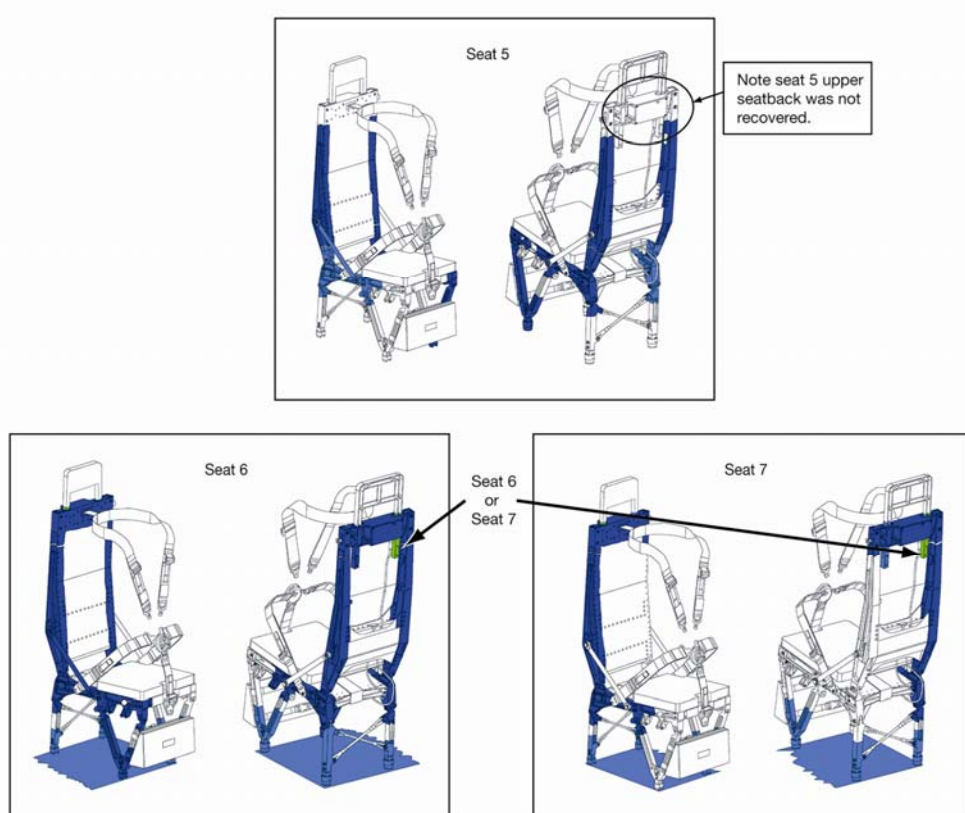
More than 68 pieces of seat structure debris were recovered. Positive assignment of the recovered seat debris to specific seat locations was difficult and required considerable analysis of subtle differences between the seats and the mounting locations because a significant portion of the lightweight seat design is common to all seven seats. Several of the recovered components were ascribable as coming from the flight deck seats (seats 1, 2, 3, and 4) and the middeck seats (seats 5, 6, and 7).

Figures 3.1-6 and 3.1-7 show seat structure pieces that were identified to each seat location. The blue items in these figures represent items that were positively identified to a seat location. The green items are those items that could be from one of two seats. Figure 3.1-8 shows the major seat structure debris pieces that could not be identified to a specific seat location (the colors in this figure distinguish the different pieces and are otherwise inconsequential). Although represented in figure 3.1-8 on just two seats, the seatback and seat restraint items could be from any of the seven seats. However, the seat pan items could only be from the Mission Specialist seats.



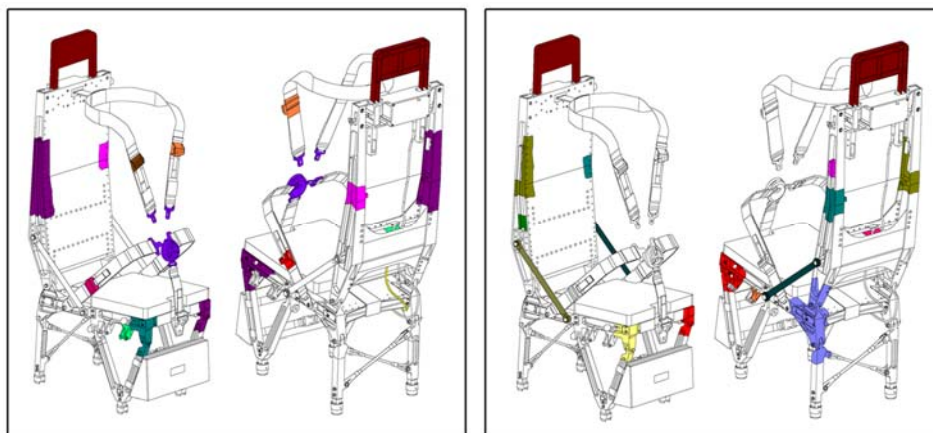
Blue items are positively identified to a specific seat;  
green items could be from either one of the two indicated seats.

**Figure 3.1-6. Identified debris from the flight deck seats. [Adapted from the Space Shuttle Systems Handbook]**



Blue items are positively identified to a specific seat;  
green items could be from either one of the two indicated seats.

**Figure 3.1-7. Identified debris from the middeck seats. [Adapted from the Space Shuttle Systems Handbook]**



Colors are used only to distinguish different debris items.

**Figure 3.1-8. Debris from unknown seat locations. [Adapted from the Space Shuttle Systems Handbook]**

The only consistent piece of seat debris that was positively identified to six seat locations (except seat 5) was a portion of the upper seatback that included the seat restraint inertial reel mechanism and strap.

Major differences in the magnitude of thermal exposure were identified on the flight deck vs. the middeck seat locations. The flight deck seat components, as well as the flight deck floor structure, were highly melted and/or deposited with splattered aluminum on all surfaces. Close inspection of the fracture surfaces on the flight deck seat attach points revealed deformation towards the vehicle starboard direction.

Materials analysis revealed that the flight deck seats collected deposits of melted aluminum from locations throughout the cabin area. Materials that were consistent with the bulkheads and outer pressure shell (2219 aluminum), the surrounding primary and secondary structure (2219, 2024, 2124, and 7075 aluminum), and the seats (2024 and 7075 aluminum) were discovered on the upper and lower surfaces of the recovered seat debris. The CAIB Report concluded,<sup>4</sup> and this report concurs, that the flight deck seats remained attached to the flight deck floor panels and adjacent to the surrounding structure during a period of significant thermal exposure and material deposition.

The magnitude and distribution of heating of flight deck seat components indicates a prolonged attachment to other crew module (CM) structure during exposure to heating. This indicates that the flight deck seat components were released from the CM later in the breakup sequence than the middeck seat components. Ground plots of debris recovery locations also support this conclusion (figure 3.1-9). Figure 3.1-10 compares a portion of the seat leg from a flight deck Mission Specialist seat component with a similar component from a middeck seat.

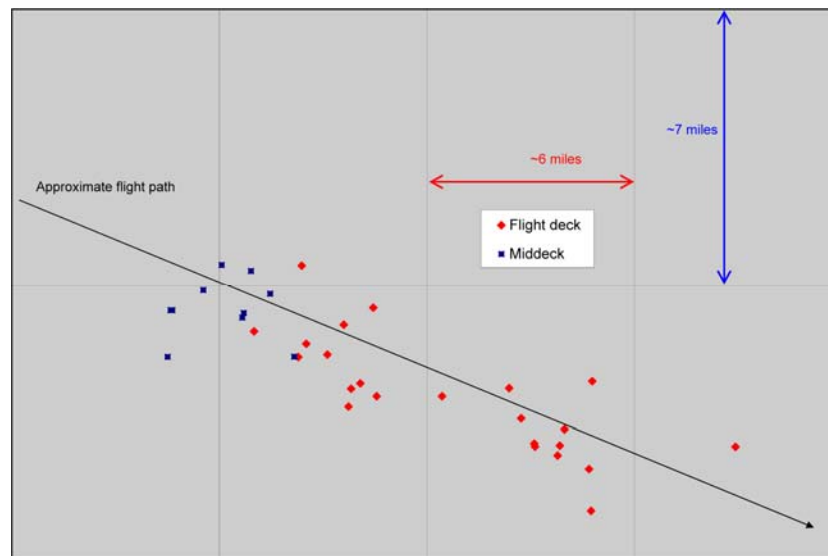


Figure 3.1-9. Recovery locations of seat structure debris.

<sup>4</sup>Columbia Accident Investigation Board Report, Volume V, Appendix G.12, Crew Survivability Report, October 2003, p. 362.

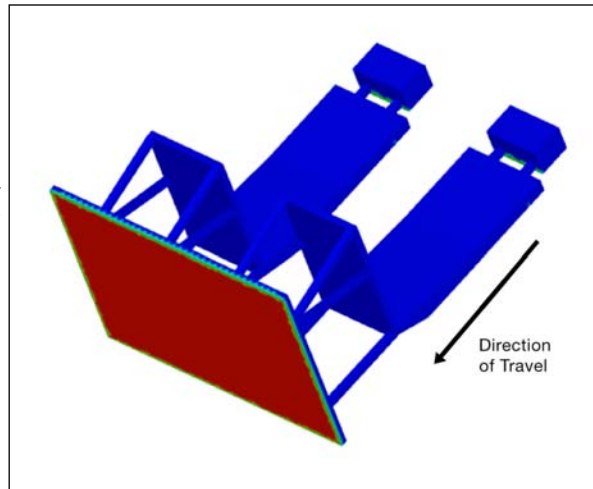


**Figure 3.1-10. Comparison of seat debris from a flight deck Mission Specialist seat (left) and a middeck Mission Specialist seat (right).**

Although all seat components experienced significant heating, the middeck seats were less eroded and fragmented when compared to the flight deck seats. Material analysis revealed that the seat 6 and 7 components collected significant deposits of melted aluminum from the lithium hydroxide (LiOH) door to which they were attached. Unlike the flight deck seat components, analysis revealed no materials consistent with the pressure shell deposited on the middeck seats. The CAIB Report concluded,<sup>5</sup> and this report concurs, that seats 6 and 7 remained attached only to the LiOH door during a period of significant thermal exposure and material deposition. The highly directional nature of the deposition indicates that the LiOH door/seat 6/seat 7 combination attained a stable attitude (figure 3.1-11) during thermal exposure. The close proximity of debris recovery locations indicates that the seat 6 and 7 components separated from the LiOH door shortly before ground impact.

<sup>5</sup>Columbia Accident Investigation Board Report, Volume V, Appendix G.12, Crew Survivability Report, October 2003, p. 362.

**Figure 3.1-11. Stable attitude of the lithium hydroxide door/seat 6/seat 7 combination, as indicated by deposition.**



Of the seats, seat 6 had the highest percentage of structure recovered and identified; seats 5 and 7 had slightly fewer structural components that were identified. The flight deck seats had significantly lower percentages of identified structural components.

Nearly all seat fractures occurred at minimum thermal cross-sectional areas (minimum thermal mass), away from any large heat sink locations.<sup>6</sup> Common seat fracture locations are shown as red lines in figure 3.1-12. It is also noteworthy that nearly all thin-sheet aluminum materials (closeout panels on the seat pan and seatback) are missing (i.e., overloaded/melted away). Additionally, with the exception of the inertial reel straps, very little belt material and seat cushion material was recovered.

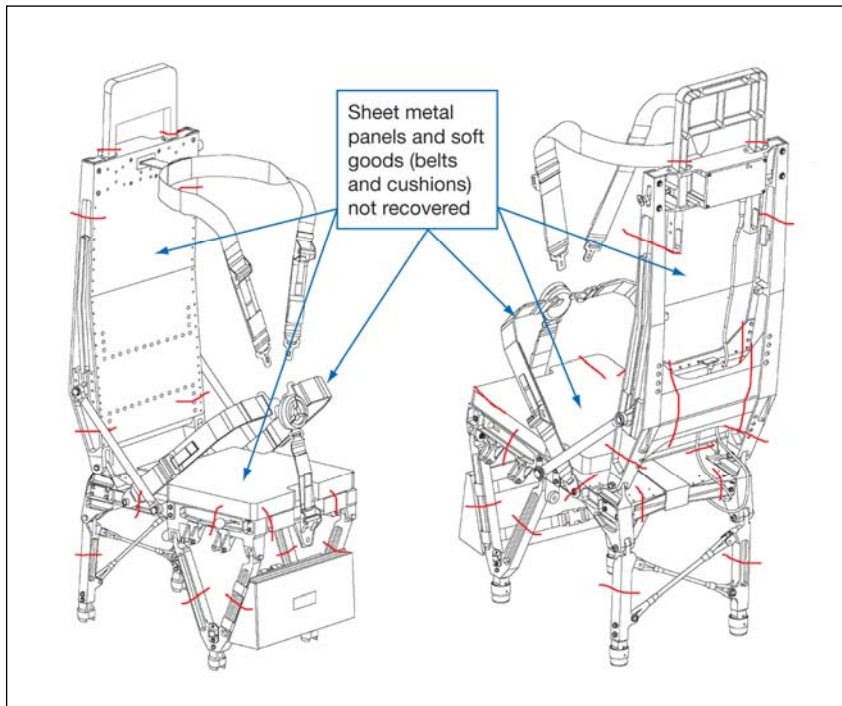


**Figure 3.1-12. Common seat failure locations (shown in red). [Adapted from the Space Shuttle Systems Handbook]**

Note: Mission Specialist seat shown; lower seat components on seats 1 and 2 are different.

<sup>6</sup>A heat sink is an area of the structure that has more material and takes longer to heat when exposed to elevated temperatures. Areas of minimal thermal cross-sectional area have less material and take less time to heat when exposed to elevated temperatures.

Examples of the fracture occurring at minimal thermal cross-sectional areas are evident on the seat leg failures for seats 6 and 7. Seats 6 and 7 are attached to a middeck floor panel that is the lid to the LiOH sub-floor storage compartment (figure 3.1-13). This panel, known as the “LiOH door,” and the attached legs pieces are shown in figure 3.1-14.

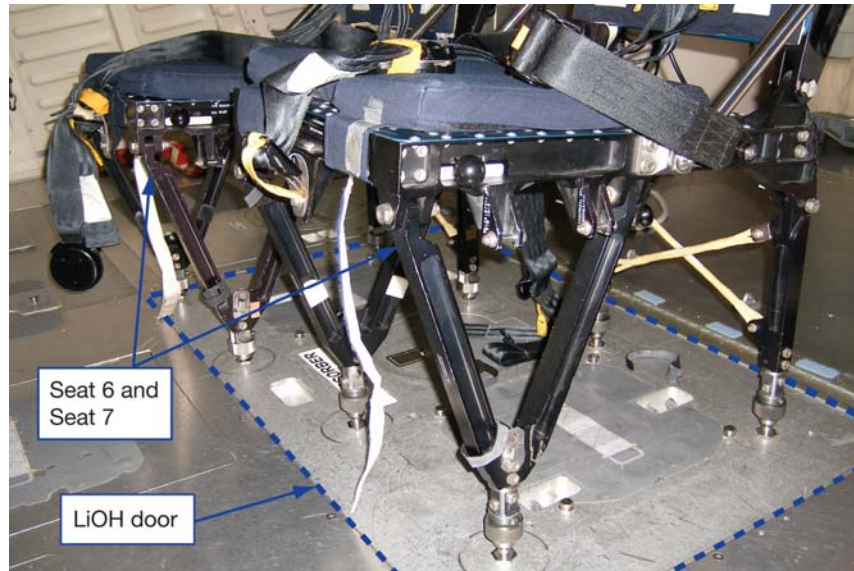


Figure 3.1-13. Example of an intact lithium hydroxide door with seats 6 and 7 attached. [Picture from the Crew Compartment Trainer]



Figure 3.1-14. Recovered lithium hydroxide door with seats 6 and 7 legs attached.

Seats 6 and 7 leg failures occurred with the legs in tension. The lowest strength margin (and, therefore, the expected failure point) at room temperature is at the leg attachment lug at the top of the leg. Analysis indicates that the leg attachment lug should fail at around 12,000 lbs. at room temperature, but only the left aft leg of seat 6 failed at the attachment lug (figure 3.1-14). Another expected leg failure point is the seat attachment floor fitting. At room temperature, the floor fitting should fail at around 21,400 lbs., but only the right forward leg from seat 6 failed at the floor fitting.

Five of the eight seat legs failed at mid-leg locations. The room temperature failure load for mid-leg fractures of the forward leg is 45,000 lbs. and the aft leg failure load is 24,000 lbs.

The seat 7 right forward leg floor fitting is present, but the corresponding seat 7 leg was not recovered; therefore, the failure location was not the floor fitting. Because this leg is very close to the edge of the LiOH door, it is possible that the failure occurred because the locking collar<sup>7</sup> was thermally damaged as the LiOH door/seat 6/seat 7 complex experienced entry heating.

Structural assessments were performed on the legs (which are made of 7075 aluminum, with a melting point between 890°F (477°C) and 1,175°F (635°C)) and the floor fitting (which is made of Inconel 718, with a melting point between 2,300°F (1,260°C) and 2,440°F (1,338°C)) to evaluate materials strengths with respect to temperature. As mentioned above, a force of 45,000 lbs. is required to cause a mid-leg tension fracture of the forward leg at room temperature. The required fracturing force decreases to 33,000 lbs. (~75% of room temperature strength) at 300°F (149°C), 21,000 lbs. (~45%) at 400°F (204°C), 9,000 lbs. (~20%) at 500°F (260°C), and 4,950 lbs. (~11%) at 600°F (316°C).

A force of 21,400 lbs. is required to fracture the floor fitting at room temperature. This force decreases to 20,300 lbs. (~95% of room temperature strength) at 300°F (149°C), 20,100 lbs. (~94%) at 400°F (204°C), and 19,900 lbs. (~93%) at 600°F (316°C). These values are plotted in figure 3.1-15.

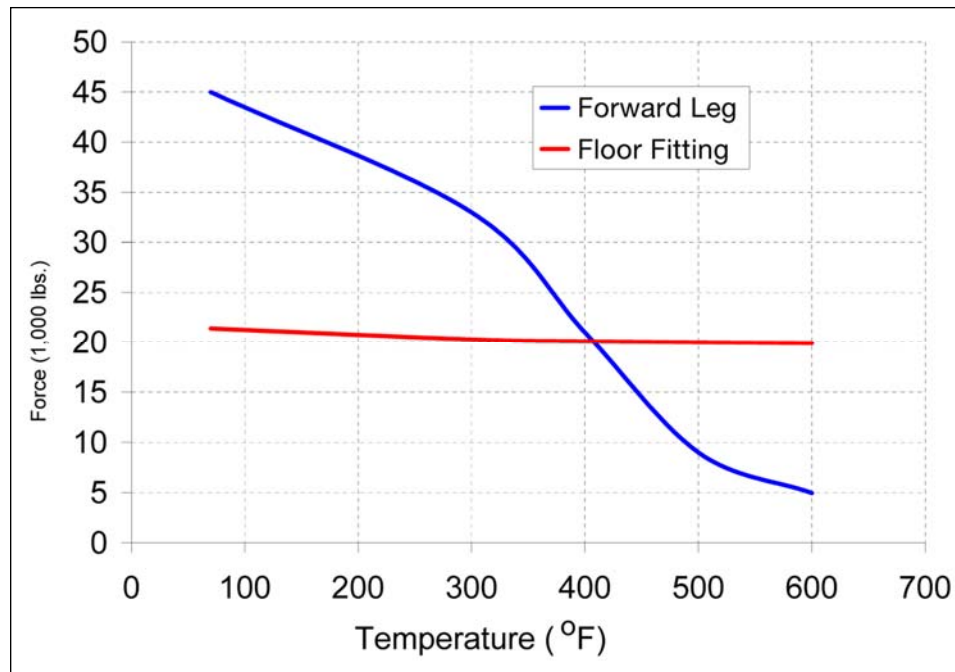


Figure 3.1-15. Failure force of seat forward leg and floor fitting vs. temperature.

This plot reveals that heating greater than 400°F (204°C) is needed to weaken the materials such that the leg failure would occur at the mid-leg location. Otherwise, the forward legs should have failed at the floor fitting, which did not occur.

The nylon material used for the seatbelts will lose strength as the temperature increases above 250°F (121°C), and will melt at approximately 400°F (204°C). Therefore, the same heating event that caused material properties changes in the metallic components of the seat structure also resulted in a complete loss of the nylon seat restraints.

<sup>7</sup>The locking collar is used to lock the seat leg to the floor fitting.

Inspection of the seat structure fracture surfaces revealed a “delamination” fracture pattern that is consistent throughout the seat debris items. The most drastic of the fractures makes it appear almost as if the 7075 aluminum material is constructed of a laminate material (figure 3.1-16). This phenomenon is termed a “broom-straw” fracture.

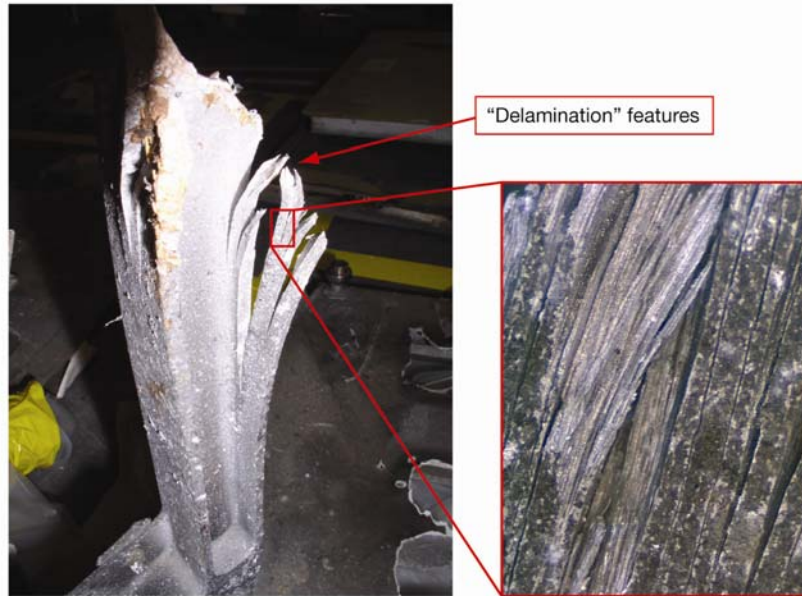


Figure 3.1-16. Example of a “broom-straw” fracture on a Columbia seat leg.

Scanning electron microscope analysis of the seat broom-straw fracture surface cross sections revealed fully intergranular fractures and equiaxed grain<sup>8</sup> microstructure. This finding is consistent with exposure to elevated temperatures and high strain rates. Equiaxed grains were discovered both along and away from the crack surfaces (figure 3.1-17).

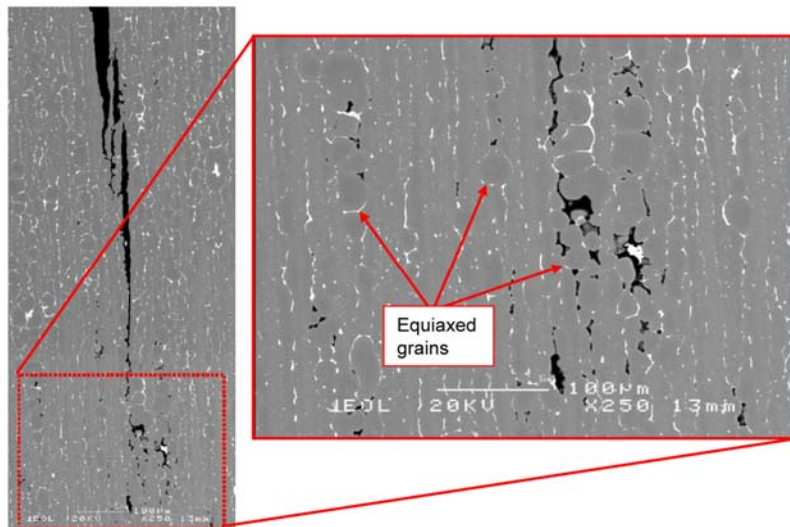


Figure 3.1-17. Scanning electron microscope image of broom-straw fracture surface cross sections.

<sup>8</sup>A grain of approximately the same size in all three dimensions; characteristic of a recrystallized microstructure.

Metallurgical evaluation was completed in proximity to, and away from, the crack surfaces using energy dispersive X-ray spectroscopy. This revealed heavy grain boundary precipitation that is consistent with the aluminum alloy experiencing temperatures greater than 900°F (482°C).

All of these features are consistent with material that is exposed to high temperatures. Significant lack of ductility surrounding the fracture areas indicates that the failures occurred at relatively high strain rates.

In all cases, seat failure occurred as a result of thermal exposure (resulting in material property degradation) followed by mechanical overload. The additional thermal degradation on the flight deck seat components is accounted for by a longer period of heating as a result of the higher ballistic number associated with an intact, free-flying flight deck.

Analysis of the debris led the CAIB to conclusions<sup>9</sup> regarding the method of seat failure (i.e., thermal exposure followed by mechanical loading), but left one question unanswered: “Why did the seats fragment so much?” As was the case with much of the *Columbia* debris, many tiny debris impact craters and/or material deposits were found on the seat debris. However, very few witness marks (dents, scrapes, divots, etc.) were found, indicating little or no impacts with debris items larger than roughly 0.25 in. Therefore, debris-debris collisions are probably not a factor in the fragmentation of the seat structure. Because the failure mechanism involved heating of the structure to temperatures exceeding 400°F (204°C) (and probably exceeding 900°F (482°C)), the nylon seat restraint material was not present as the seat structure was breaking. This led the Spacecraft Crew Survival Integrated Investigation Team (SCSIIT) to conclude that the seat was unoccupied at the time it was breaking up. No other conclusion can be made because the thermal and aerodynamic mechanisms in the high-altitude, hypersonic flight regime are not well understood.

### 3.1.4 Upper seatbacks/inertial reels

Six out of the seven upper seatback items (all but seat 5) were recovered. Each item was positively identified to a seat position. Each recovered upper seatback debris item contained the inertial reel/recoil mechanism and some amount of strap material, which recoiled into the inertial reel housing following strap failure. This strap material amounted to the only significant nylon webbing recovered from each of the seatbelt restraint systems. Figure 3.1-18 shows the location of the upper seatback/inertial reel.

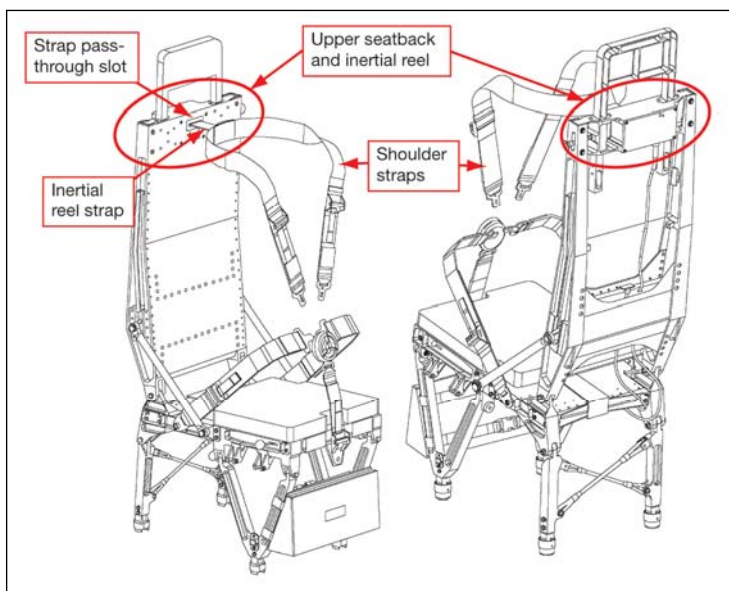


Figure 3.1-18. *Upper seatback debris item location.* [Adapted from the Space Shuttle Systems Handbook]

<sup>9</sup>*Columbia* Accident Investigation Board Report, Volume V, Appendix G.12, Crew Survivability Report, October 2003, p. 364.

As with the general seat failures that were described previously, all of the fractures at the upper seatback location occurred at the minimum thermal cross section, away from heat sinks on either side. Fracture surfaces did not exhibit melting or materials deposition, indicating that the upper seatback fractures occurred near the end of the period of heating and material deposition. Figure 3.1-19 shows all six recovered upper seatback items. Table 3.1-1 summarizes the upper seatback findings.

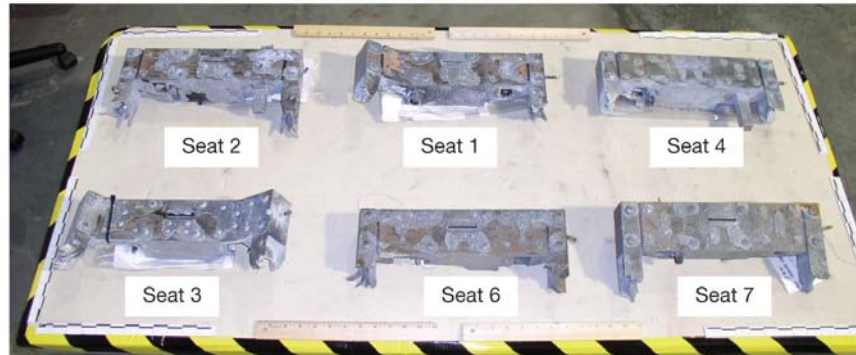


Figure 3.1-19. Upper seatbacks (front view).

Table 3.1-1. Upper Seatback Comparisons

Seat	Deformation	Fractures	Thermal Effects
Seat 1	Right frame member is bent forward, about the headrest bushing.	Tensile/bending fractures (with “broom-straw” features) are present on both the left and the right seatback frame members, just below the lower surface of the upper seatback/inertial reel assembly.	A moderate amount of splattered aluminum is present throughout, primarily deposited on the upper and lower surfaces (the upper surfaces more than the lower). No melting of fracture surfaces is noted.
Seat 2	Deformation is limited to the areas local to the fractures.	Tensile/bending fractures (with “broom-straw” features) are present on both the left and the right seatback frame members, just below the lower surface of the upper seatback/inertial reel assembly.	A moderate amount of splattered aluminum is present throughout, primarily deposited on the upper and lower surfaces (the upper surfaces more than the lower). No melting of fracture surfaces is noted.
Seat 3	Left and right frame members bent forward. Left side is bent about the headrest bushing; right side is bent just out-board of the bushing.	Tensile/bending fractures (with “broom-straw” features) are present on both the left and the right seatback frame members, just below the lower surface of the upper seatback/inertial reel assembly.	A large amount of splattered aluminum is present throughout, primarily deposited on the upper and lower surfaces. Noted the absence of deposited material on the portside bushing. No melting of fracture surfaces is noted.
Seat 4	Deformation is limited to the areas local to the fractures.	Tensile/bending fractures (with “broom-straw” features) are present on both the left and the right seatback frame members, just below the lower surface of the upper seatback/inertial reel assembly.	A large amount of splattered aluminum is present throughout, primarily deposited on the upper and lower surfaces. No melting of fracture surfaces is noted.
Seat 6	Slight deformation in the right frame member, bent about the headrest bushing.	Tensile/bending fractures (with “broom-straw” features) are present on both the left and the right seatback frame members, just below the lower surface of the upper seatback/inertial reel assembly.	A large amount of splattered aluminum material is deposited primarily on the lower surface. Noted a near complete absence of deposition on the upper surface. No melting of fracture surfaces is noted.

Table 3.1-1. *Upper Seatback Comparisons (Continued)*

Seat	Deformation	Fractures	Thermal Effects
Seat 7	Deformation is limited to the areas local to the fractures.	Tensile/bending fractures (with “broom-straw” features) are present on both the left and the right seatback frame members, just below the lower surface of the upper seatback/inertial reel assembly.	A large amount of splattered aluminum material is deposited on the lower surface. Noted a complete absence of deposition on the upper surface. No melting of fracture surfaces is noted.
Interpretations		Seat fractures occur at minimum thermal cross section, away from heat sinks on either side.	Middeck items appear to have experienced significant splatter initiating from below. Flight deck items appear to have experienced significant splatter initiating from above and below. Lack of melting on the fracture surfaces indicates that the fractures occurred after the period of heating.
Conclusions	Observed deformations are affiliated with seat breakup fractures.	Fractures are consistent with general seat failure mechanism (thermal heating followed by mechanical overload).	Flight deck items experienced significant splattering initiating from above and below. Middeck items experienced significant splattering initiating from below <i>only</i> . Upper seatback fractures occurred after the period of heating.

For each seat, the inertial reel housing was removed from the upper seatback inertial reel cavity (figure 3.1-20). The cavity, housing, and mounting hardware were inspected for deformation, witness marks, debris impacts, and material deposition. Results for each seat position are generalized below.



Upper seatback (rear view).

Inertial rear cavity (rear view of intact seat).

Figure 3.1-20. *Inertial reel mounting location.*

Only seat 3 showed deformation of the inertial reel housing mounting hardware. All four mounting bolts were bent slightly. One inertial reel housing mounting lug was broken with melted metal deposits on both fracture surfaces; i.e., the fracture surface of the lug and the fracture surface of the inertial reel housing (figure 3.1-21). The inertial reel mounting hardware for the other five recovered upper seatbacks exhibited no deformations.

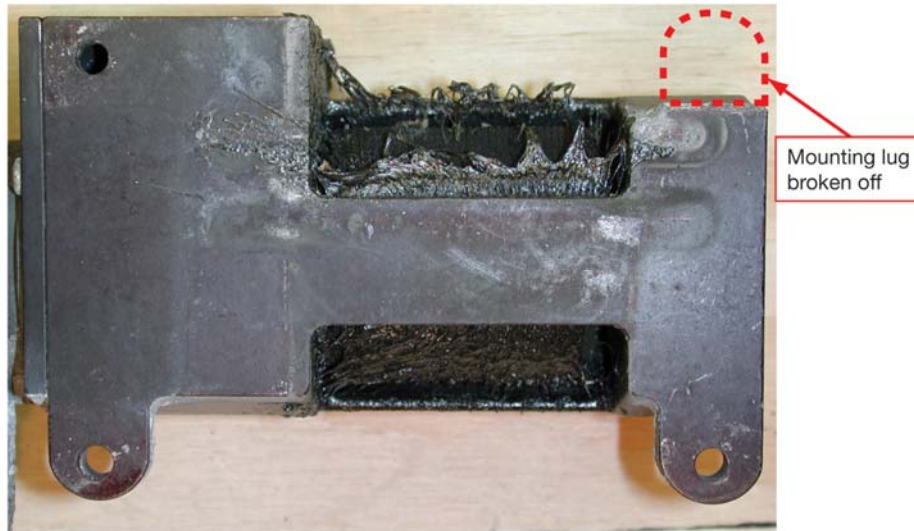
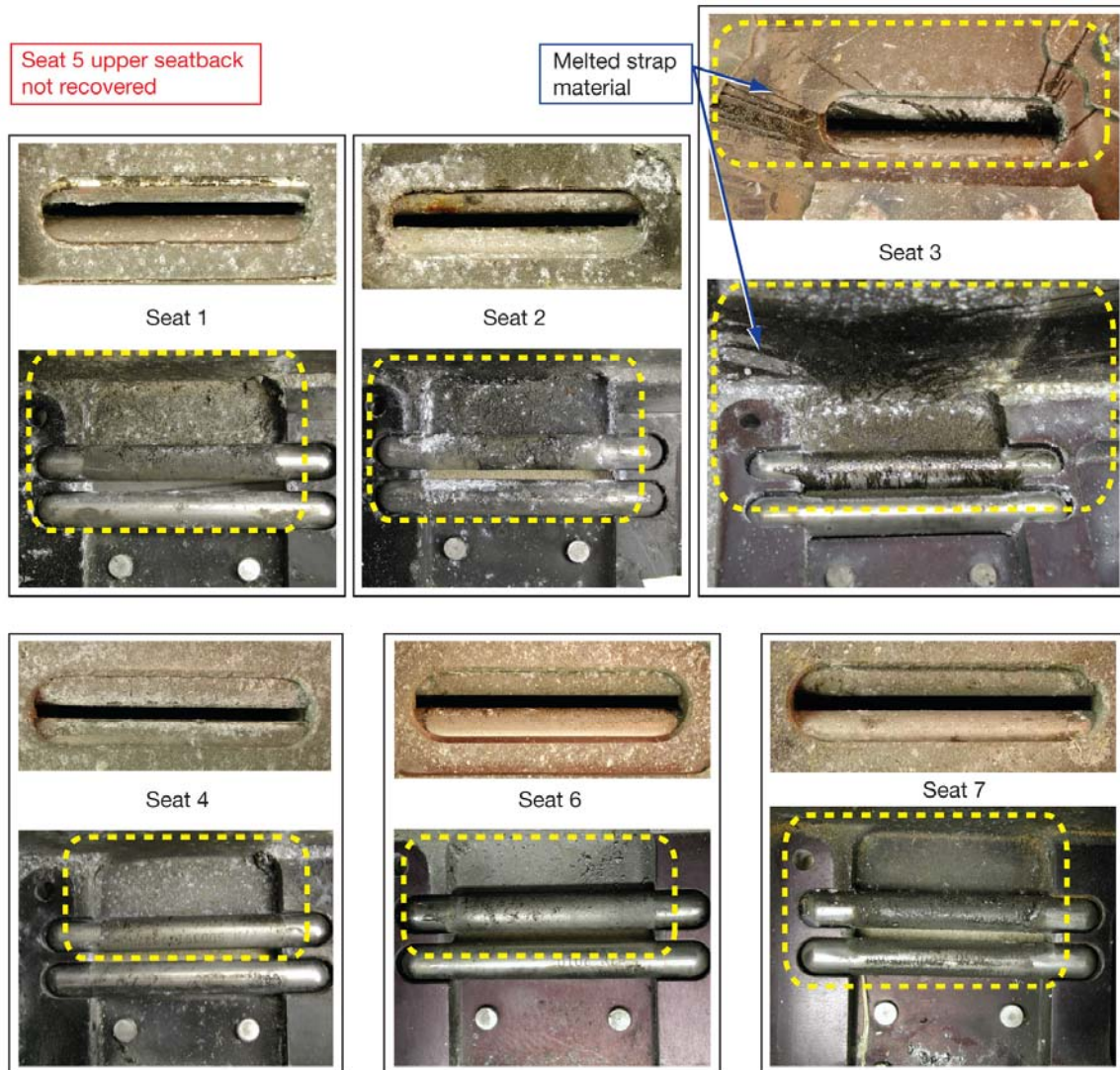


Figure 3.1-21. Seat 3 inertial reel, looking aft.

In all cases, melted strap material (nylon) was discovered inside the upper seatback inertial reel cavity, including on the strap rollers (figure 3.1-22). Only seat 3 had melted strap material on the external surface of the upper seatback. In this instance, the melted strap material flowed out of and away from the inertial reel strap pass-through slot, indicating that the melted material originated from inside the upper seatback inertial reel cavity. The lack of melted strap material on the outside of the seatbacks indicates that the torso restraint system failure occurred at the inertial reel strap and the remaining inertial reel strap retracted completely into the seatback, leaving no material to be melted and deposited on the external surfaces of the seats.



**Figure 3.1-22. Upper seatback inertial reel strap pass-through slots – external (top)/internal (bottom); melted strap material areas outlined in yellow.**

For all cases except seat 3, the melting and flow patterns of melted strap material are consistent with airflow entering the inertial reel lead-in strap pass-through slot in the upper seatback (forward-to-aft flow with respect to the seat). The melting and interior flow patterns of seat 3 are consistent with airflow entering the pass-through slot for the majority of the time that the seat was exposed to heating. Melted strap material on the exterior of the upper seatback indicates that airflow forced melted material out of the pass-through slot (aft-to-forward flow) for some period(s) of time. However, the radial flow pattern on the exterior surfaces indicates forward-to-aft airflow on the upper seatback once the melted material exited the slot. These melting and flow patterns could indicate that the upper seatback item was tumbling as it experienced heating.

In all cases, the inertial reel straps were melted only in areas that were immediately adjacent to the strap pass-through openings and along the lateral edges of the strap (figure 3.1-23). The strap material in other areas was not melted and appears normal.

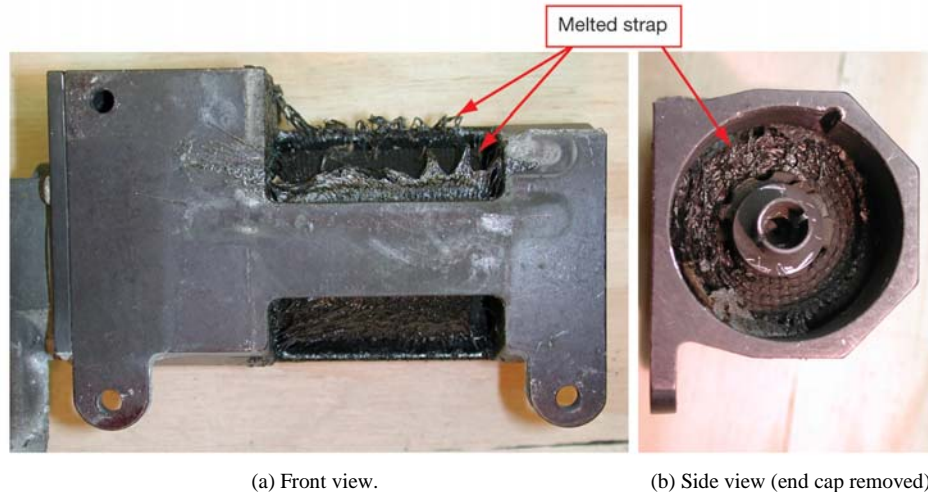


Figure 3.1-23. *Inertial reel melted strap material.*

### 3.1.5 Inertial reel straps

Each recovered inertial reel mechanism was disassembled to inspect the inertial reel strap and the inertial reel locking mechanism. This inspection revealed that strap failures occurred at various locations along the strap length.<sup>10</sup>

Five of the six recovered strap ends terminated along a straight line. The exception was the strap for seat 2, which terminated in a jagged line. Away from, but in close proximity to, the melted areas, the residual strap material remains flexible. This is consistent with melting that occurred after the strap recoiled into the housing (the straight lines correspond to where the straps were exposed at the pass-through slot). If the whole strap was exposed to significant heating/melting, a definite thermal gradient (varying degrees of melting) and some melting and “pulling” at the broken end of the strap would be seen. However, none of the straps exhibited a thermal gradient along the strap or melting and pulling at the broken end. The demarcation between melted and non-melted areas is very distinct (figure 3.1-24), indicating that the straps were protected inside the inertial reel housings during the period of high heating.



Figure 3.1-24. *Close-up of strap melt pattern.*

<sup>10</sup>The seats normally have 22 in. of inertial reel strap when measured from the reel to the shoulder harness y-split attachment.

The inertial reel straps failed primarily due to mechanical overload. Limited melting of the straps (and only in distinct areas that were unprotected by the inertial reel housing) indicates that melting was not a significant factor in the inertial reel strap failure. The mechanical overload may have been affected by elevated temperatures that weakened the straps, but these temperatures were not sufficient to cause obvious thermal damage to the strap. Significant strap melting occurred after the inertial reel straps failed and recoiled into the housing. Therefore, the inertial reel straps failed (and the *Columbia* crew members were, at most, partially restrained in their seats) prior to the end of the period of thermal exposure.

Metallic material was discovered on upper and lower strap surfaces when the straps were extended for inspection. Melted aluminum material was deposited on the straps for four of the six recovered inertial reels. The two exceptions were seats 1 and 2, both of which had strap failures at or near the inertial reel end of the straps. The deposition differed in character from the top-level depositions seen on the windows, which were more diffuse and uniform. Seat strap deposition consisted of globules or spheroids of metallic material (> 1/32 in.) that are widely scattered across the strap. Generally, there were no more than three or four deposited globules of metal per strap. Deposits on seats 4, 6, and 7 straps were close to the inertial reel end of the straps – areas of the straps that would not be exposed when the crew members were sitting upright in their seats. For material deposition to occur in these areas, the crew members had to be leaning to the side or leaning forward (or a combination of both), thereby extending the straps out of the inertial reel housing. The deposition of these material globules on the straps occurred before crew separation from the seats, yet after the CM pressure shell had been breached and the CM had been depressurized.

Evidence from the inertial reel straps indicates that the seats 1, 2, and 3 straps were mostly extended at the time of strap failure. The seats 4, 6, and 7 straps were extended during a material deposition period (seat 4 at least 8 in., or ~36% extended; seat 6 at least 21.25 in., or ~96% extended; and seat 7 at least 21.5 in., or ~98% extended). This indicates that the crew members were in seats 1 through 4 and seats 6 and 7 with at least the shoulder belts attached to the seatbelt buckle (the seat 5 upper seatback was not recovered). It is concluded that the inertial reels did not lock.<sup>11</sup>

**Finding.** Evidence from the inertial reel straps indicates that the seats 1, 2, and 3 straps were mostly extended at the time of strap failure. The seats 4, 6, and 7 straps were extended during a material deposition period (seat 4 at least 8 in., or ~36% extended; seat 6 at least 21.25 in., or ~96% extended; and seat 7 at least 21.5 in., or ~98% extended). Medical evidence (see Section 3.4) indicates that some of the crew members received injuries consistent with insufficient upper body restraint.

**Conclusion L2-2.** The seat inertial reels did not lock.

**Conclusion L2-3.** Lethal injuries resulted from inadequate upper body restraint and protection during rotational motion.

**Recommendation L1-3/L5-1.** Future spacecraft crew survival systems should not rely on manual activation to protect the crew.

**Recommendation L2-4/L3-4.** Future spacecraft suits and seat restraints should use state-of-the-art technology in an integrated solution to minimize crew injury and maximize crew survival in off-nominal acceleration environments.

<sup>11</sup>This conclusion is consistent with the entry simulation X-axis loads (discussed in Section 2.1.3 and shown in figure 2.1-16) remaining below the inertial reel auto-lock threshold of 1.78 G. Additionally, this conclusion is consistent with findings described in the Department of Defense Joint Service Specification Guide JSSG-2010-7, Crash Protection Handbook. The handbook describes a failure mode of MA-6 type inertial reels in which the reels failed to lock in crashes involving X-axis loads below the auto-lock threshold and subsequent Z-axis loads forcing the seat occupant down and forward, resulting in the occupant's torso being unrestrained during the crash dynamics. The handbook states that the "MA-6/MA-8 units were shown to be deficient in design and proven to be unreliable in survivable crash conditions." This precipitated a revision to MIL-R-8236, which is the military specification governing performance criteria for inertial reels used in military aircraft. The update to the military specification and the publication of the crash protection handbook occurred after the shuttle seats were designed.

**Recommendation L2-8.** The current shuttle inertial reels should be manually locked at the first sign of an off-nominal situation.

Indentations matching the linear ridges on the inertial reel spool were observed 0 to 4 in. from the strap attach location (figure 3.1-25). These linear indentations near the inertial reel, were present on all the straps (except the seat 1 strap, which failed next to the inertial reel attachment). Inertial reel straps for 11 other shuttle flight seats in inventory (not *Columbia* debris) and training seats were inspected for similar linear features. The inertial reel straps for all seats exhibited the same waves that were found on the *Columbia* inertial reel straps. Therefore, the waves are a result of strap stowage, not an indication of loading on the strap.

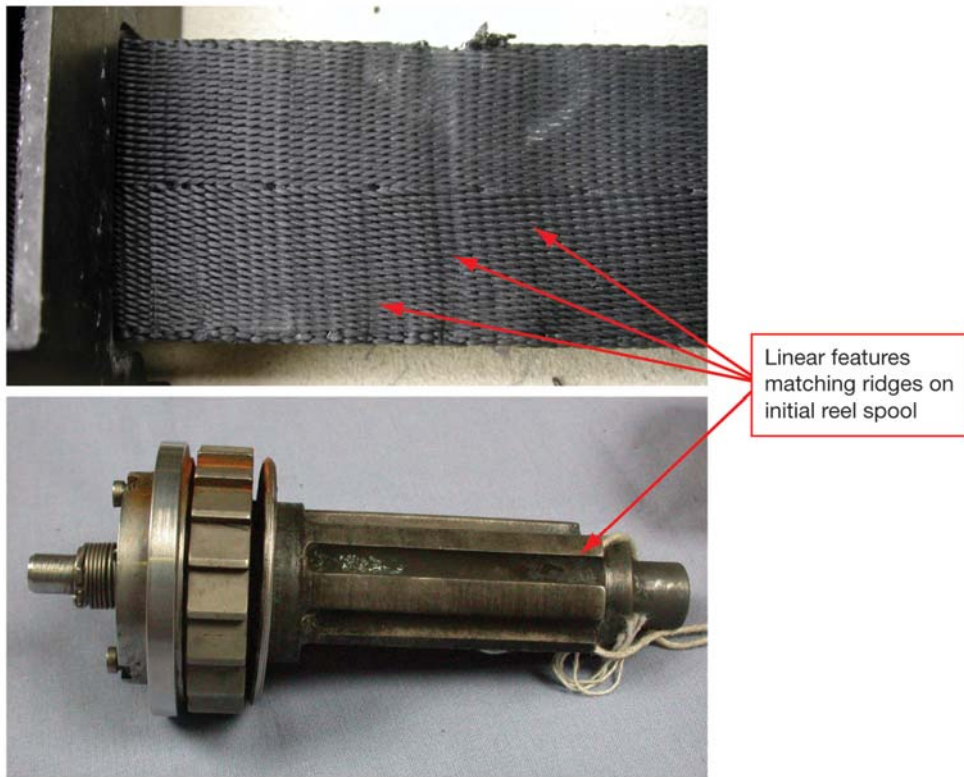


**Figure 3.1-25.** Example of linear waves on inertial reel straps.

The inertial reel strap findings for each upper seatback are summarized below. Table 3.1-2 compares the inertial reel strap findings.

Table 3.1-2. *Inertial Reel Strap Comparisons*

Seat	Strap Failure Location	Extent of Melting/Condition of Residual Strap Material
<b>Seat 1</b>	The strap failed at approximately 2% of the extended length, in proximity to the attachment to the inertial reel (< 1/2 in. away from the inertial reel, out of the original 22 in. of strap).	Residual strap material exists only at the end of the strap still attached to the inertial reel spool.
<b>Seat 2</b>	The strap failed at approximately 20% of the extended length, in proximity to the attachment to the inertial reel (~4.5–5 in. away from the inertial reel, out of the original 22 in. of strap). The strap failed at an approximately 45-degree angle, over a 1- to 2-in. length.	The strap melted only at the exposed strap pass-through areas and the lateral edges of the inertial reel housing. The strap material that was shielded by the inertial reel housing did not melt. This suggests that mechanical failure occurred before significant thermal exposure.
<b>Seat 3</b>	The strap failed at approximately 90% of the extended length, in proximity to the attachment to the shoulder harness y-split (~20 in. away from the inertial reel, out of the original 22 in. of strap). Strap failure appears to have occurred in close proximity to the shoulder split attachment, probably at the stitch stress concentration. Two raised sections at a slight angle (~20 degrees) from perpendicular to the strap axis, observed 2 to 4 in. from the strap attach location. Marks are similar to “bird-caging” features found in dynamic failures of cable/cord. Approximately 10 small metallic bits of debris, largest approximately 1/8 in. in diameter located approximately 16.5 to 18 in. away from reel attachment.	The strap melted only at the exposed strap pass-through areas and the lateral edges of the inertial reel housing. The strap is melted completely through one layer near the upper pass-through. The strap material that was shielded by the inertial reel housing is not melted. This suggests mechanical failure before significant thermal exposure.
<b>Seat 4</b>	The strap failed at approximately 80% of the extended length, in proximity to the attachment at the shoulder harness y-split (~18 in. away from the inertial reel, out of the original 22 in. of strap). One very small ball (< 1/16 in.) of melted metallic material was located approximately 14 in. from the reel attachment, on the lateral edge of the upper strap surface. (Note that the debris came off during inspection.)	The strap melted only at the exposed strap pass-through areas and the lateral edges of the inertial reel housing. The strap is melted completely through one layer near the upper pass-through. The strap material that was shielded by the inertial reel housing is not melted. This suggests mechanical failure before significant thermal exposure.
<b>Seat 6</b>	The strap failed at approximately 90% of the extended length, in proximity to the attachment at the shoulder harness y-split (~20 in. away from the inertial reel, out of the original 22 in. of strap). Strap failure appears to have occurred in close proximity to the shoulder split attachment, probably at the stitch stress concentration. Three pieces of metallic debris were deposited on the strap surfaces: 1. A small ball of melted material (< 1/32-in. dia.) deposited on the upper surface, located approximately 16 in. from the reel attachment. (Note that described debris came off during inspection.) 2. A small fragment of melted material (< 1/32-in. dia.) deposited on the lateral strap edge, located approximately 13 in. from the reel attachment. 3. A small fragment of melted material (< 1/32-in. dia.) deposited on the lateral strap edge, located approximately 1.75 in. from the reel attachment.	The strap melted only at the exposed strap pass-through areas and the lateral edges of the inertial reel housing. The strap is melted completely through one layer near the upper pass-through. The strap material that was shielded by the inertial reel housing is not melted. This suggests that mechanical failure occurred before significant thermal exposure.

Table 3.1-2. *Inertial Reel Strap Comparisons (Continued)*

Seat	Strap Failure Location	Extent of Melting/Condition of Residual Strap Material
<b>Seat 7</b>	<p>The strap failed at approximately 50% of the extended length (~11 in. away from the inertial reel, out of the original 22 in. of strap).</p> <p>Three pieces of metallic debris were deposited on the strap:</p> <ol style="list-style-type: none"> <li>1. One approximately 1/10-in. diameter, roughly spherical piece of metal debris is stuck to the edge (the right side of seat) of the lower surface of the strap, approximately 1.5 in. from the inertial reel.</li> <li>2. One 0.5 in. × 0.3 in. roughly triangular (~0.05-in.-thick) piece of metal debris is stuck to the lower surface of the strap, approximately 8 in. from the inertial reel.</li> <li>3. Several small, roughly spherical metal debris items are stuck to the upper side of the strap fragment, along the edge, approximately 2 in. from the end.</li> </ol>	<p>The strap melted only at the exposed strap pass-through areas and the lateral edges of the inertial reel housing. The strap is melted completely through one layer near the upper pass-through. The strap material that was shielded by the inertial reel housing is not melted. This suggests that mechanical failure occurred before significant thermal exposure.</p>
<b>Interpretations</b>	<p>Seats 1 and 2 straps failed at or near the end of the strap at the inertial reel (the belt was almost fully extended). The seat 3 strap shows evidence (“birdcage” witness marks near the inertial reel) suggesting that the belt was almost fully extended at the time of failure.</p> <p>The seat 4 strap shows evidence (melted material deposited approximately 14 in. from inertial reel) indicating that the belt was partially (~8 in. or ~36%) extended during the period of material deposition.</p> <p>The seat 6 strap shows evidence (melted material deposited approximately 1.75 in. from the inertial reel) indicating that the belt was mostly (~21.25 in. or ~96%) extended during the period of material deposition.</p> <p>The seat 7 strap shows evidence (melted material deposited approximately 1.5 in. from the inertial reel) indicating that the belt was mostly (~21.5 in. or ~97%) extended during the period of material deposition.</p>	<p>The straps exhibit areas of flexible strap material right next to areas of melted strap. The “border” between the areas is defined by the presence of the inertial reel housing shielding portions of the strap.</p> <p>If thermal exposure (significant strap melting) was a major factor in the failure of the strap, a thermal exposure gradient over some finite length should be present on the straps. The lack of a thermal exposure gradient, and the presence of evidence indicating drastic differences in thermal exposure, point to the strap failure mode as being primarily mechanical in nature.</p>
<b>Conclusions</b>	<p>The seats 1, 2, and 3 straps were mostly extended at the time of strap failure.</p> <p>All others straps failed at locations ranging from 50 to 90% of strap length (away from recoil attach point). The seats 4, 6, and 7 straps were extended during the material globule deposition period: The seat 4 strap was at least 8 in. extended; the seat 6 strap was at least 21.25 in. extended; and the seat 7 strap was at least 21.5 in. extended.</p> <p>The presence of melted metal globules deposited on several of the straps indicates that the mechanical overload of the straps occurred after exposure to a thermal environment resulting in globule deposition. This evidence confirms crew members were in seats 1, 2, 3, 4, 6, and 7 at the time of inertial reel strap failure, and the inertial reels did not lock.</p>	<p>In all cases, mechanical overload of the inertial reel strap occurred independent from significant thermal degradation. Note that the failure of the inertial reel strap may have been affected by material property degradation due to elevated temperatures.</p>

Seat 1 experienced strap failure at the end of the strap next to the inertial reel, and seat 2 experienced strap failure near the end of the strap next to the inertial reel. The seat 1 strap failure (figure 3.1-26) occurred in a straight line along the strap attach point shear plane (the expected failure point if the strap is fully extended).

The seat 2 strap failed at an approximate 45-degree angle, over a 1- to 2-in. length, approximately 4.5 in. from the inertial reel (figure 3.1-26). The way in which the seat 2 belt failed is unique among the

six recovered inertial reel straps. This failure is similar to a failure mode known as strap “dumping.”<sup>12</sup> It is theorized that loading of the inertial reel strap laterally against the pass-through slot (figure 3.1-27) resulted in damage to the strap and, eventually, strap failure.

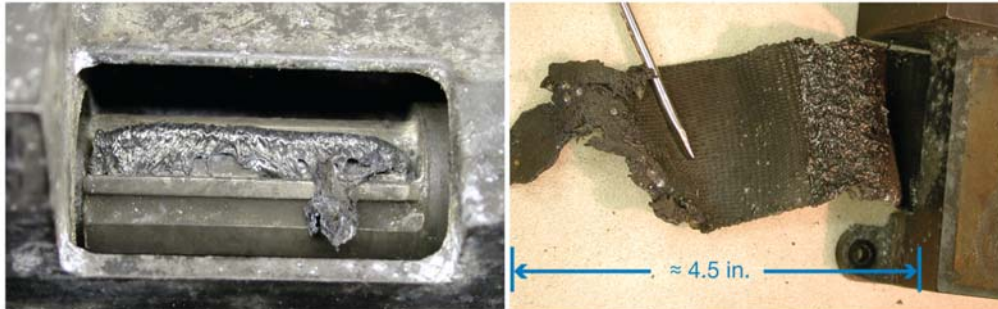


Figure 3.1-26. Seat strap failures: seat 1 (left) and seat 2 (right).

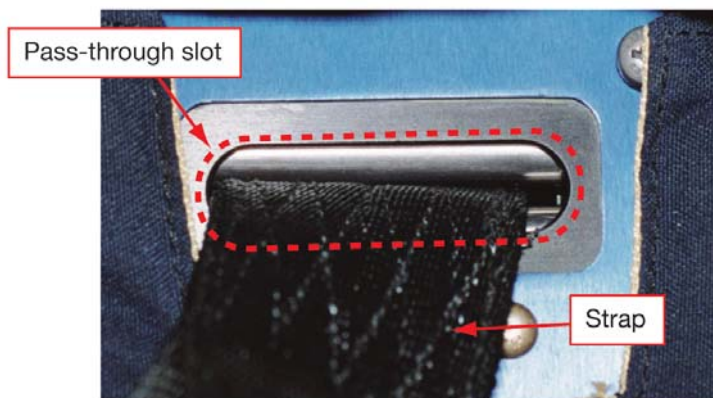


Figure 3.1-27. Seat strap pass-through slot (intact seat shown). [Picture from a shuttle training mockup in the JSC Space Vehicle Mockup Facility]

**Finding.** The seat 2 inertial reel strap exhibits “strap dumping” failure features. The strap failed progressively, possibly due to damage to the lateral edge of the strap from contact with the sharp edge of the strap pass-through slot.

**Recommendation L2-5.** Incorporate features into the pass-through slots on the seats such that the slot will not damage the strap.

The seat 3 inertial reel strap (figure 3.1-28) failed at approximately 90% of the extended length (~20 in. away from the inertial reel). This strap failure occurred in close proximity to the shoulder harness y-split attachment, which is the expected failure point if a strap is not fully extended (the inertial reel strap will fail at around 5,200 to 5,300 lbs.). Wave features, which were observed approximately 2 to 4 in. from the strap attach location at a slight angle (~20 degrees) from perpendicular to the strap axis, were similar to the “birdcaging”<sup>13</sup> features found in dynamic failures of cable/cord. Because these birdcage features are close to the inertial reel end of the strap, the strap failure occurred with the strap mostly extended (retracted only 2 to 4 in.). Approximately 10 small metallic bits of debris, the larger of which are approximately 1/8 in. in diameter, were located approximately 16.5 to 18 in. away from the inertial reel attachment.

<sup>12</sup>Dumping is a strap failure mode caused by progressive strap failure that can be preceded by damage to the lateral edge of a strap.

<sup>13</sup>Describes the appearance of a multistranded rope or strap that has been subjected to compression or a sudden release of tension load. The outer strands are displaced outward, forming a cage-like appearance.



Figure 3.1-28. Seat 3 inertial reel strap.

The seat 4 inertial reel strap (figure 3.1-29) failed at approximately 80% of the extended length, which is in proximity to the attachment at the shoulder harness y-split (~18 in. away from the inertial reel). One very small ball of melted metallic material (< 1/16 in.) was located approximately 14 in. from the inertial reel attachment on the lateral edge of the upper strap surface (the debris came off during inspection.). No witness marks were observed along the entire strap length.

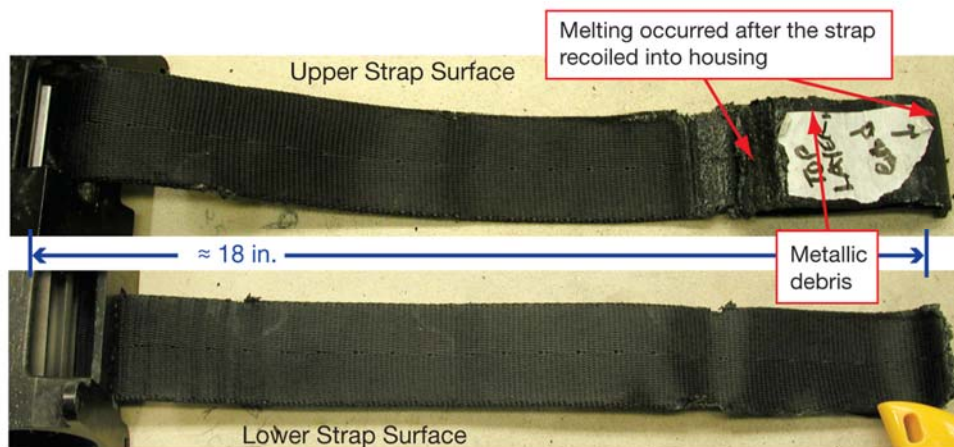


Figure 3.1-29. Seat 4 inertial reel strap.

The seat 6 inertial reel strap (figure 3.1-30) failed at approximately 90% of the extended length (~20 in. away from the inertial reel). Strap failure occurred in close proximity to the shoulder harness y-split attachment (the expected failure point if the strap was not fully extended). No witness marks were observed along the entire strap length. Three pieces of metallic debris were deposited on the strap surfaces: a small ball of melted material (< 1/32-in. dia.) deposited on the upper surface, approximately 16 in. from the reel

attachment (debris came off during inspection); a small fragment of melted material (< 1/32-in. dia.) deposited on the lateral strap edge located approximately 13 in. from the reel attachment; and a small fragment of melted material (< 1/32 in. dia.), which was deposited on the lateral strap edge located approximately 1.75 in. from the reel attachment. The strap was melted completely through one layer near the strap pass-through opening.

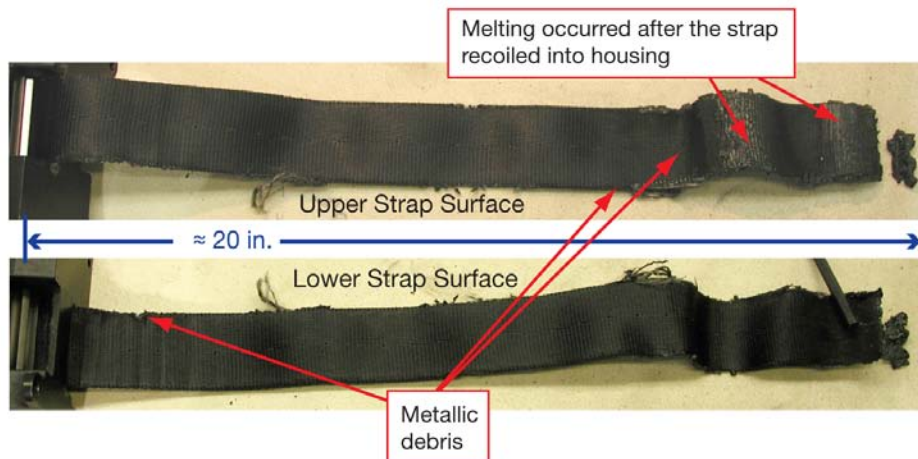


Figure 3.1-30. Seat 6 inertial reel strap.

The seat 7 inertial reel strap (figure 3.1-31) failed at approximately 50% of its length (~11 in. away from the inertial reel). No witness marks were observed along the entire strap length. Three areas of metallic debris deposits were noted on the strap: one approximately 1/10-in.-diameter, roughly spherical piece of metal debris stuck to the edge (the right side of seat) of the lower surface of the strap, approximately 1.5 in. from the inertial reel; one 0.5-by-0.3-in. roughly triangular (~0.05-in.-thick) piece of metal debris stuck to the lower surface of the strap, approximately 8 in. from the inertial reel; and several small, roughly spherical metal debris items stuck to the upper side of the strap fragment, along the edge, approximately 2 in. from the end. Localized melting caused the strap to separate into two pieces after the strap had recoiled into the housing.

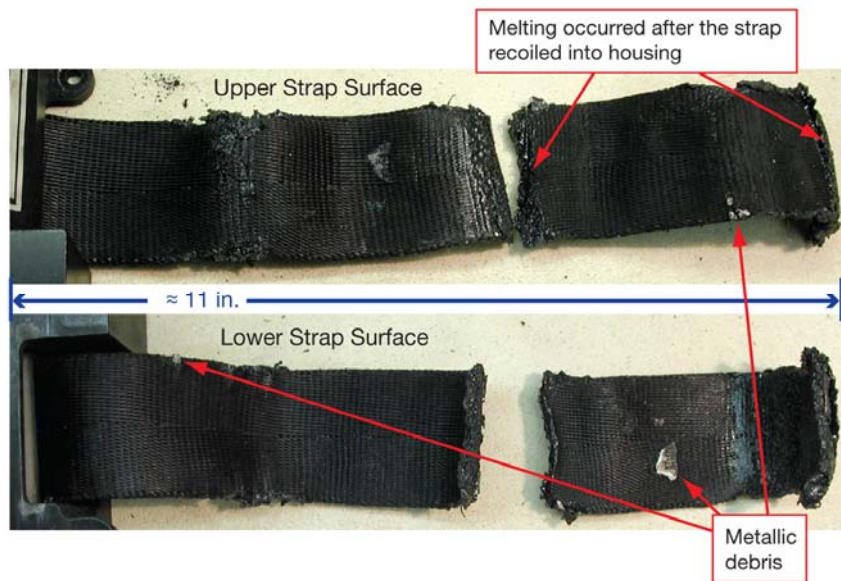


Figure 3.1-31. Seat 7 inertial reel strap.

The inertial reel straps are certified to sustain at least 5,000 lbs. of load (at least 2,500 lbs. of load when the strap is fully extended). Vendor testing indicates that the straps fail at approximately 5,200 lbs. (or at ~3,500 lbs. if the strap is fully extended). These values are for straps tested statically at room temperature; the loads required to fail the straps at elevated temperatures are unknown. Additionally, the material properties (combustion vs. chemical degradation vs. melting) in a high-temperature/low-O<sub>2</sub>/low-pressure environment are not known, neither are the strap properties in highly dynamic loading situations (high loads over very short time periods). Therefore, the inertial reel straps alone could not provide sufficient evidence for determining the loads at which the straps failed.

**Finding.** All inertial reel straps are tested with static loads at room temperature. Load testing has not been conducted to determine the loads required to fail the straps at elevated temperatures or under dynamic loads. Testing has not been conducted to determine the material properties (combustion vs. chemical degradation vs. melting) in a high-temperature/low-O<sub>2</sub>/low-pressure environment.

**Recommendation L2-6.** Perform dynamic testing of straps and testing of straps at elevated temperatures to determine load-carrying capabilities under these conditions. Perform testing of strap materials in high-temperature/low-oxygen/low-pressure environments to determine materials properties under these conditions.

### 3.1.6 Inertial reel locking mechanisms

After inspection of the inertial reel straps was completed, each of the inertial reel/recoil mechanisms was disassembled (figure 3.1-32).

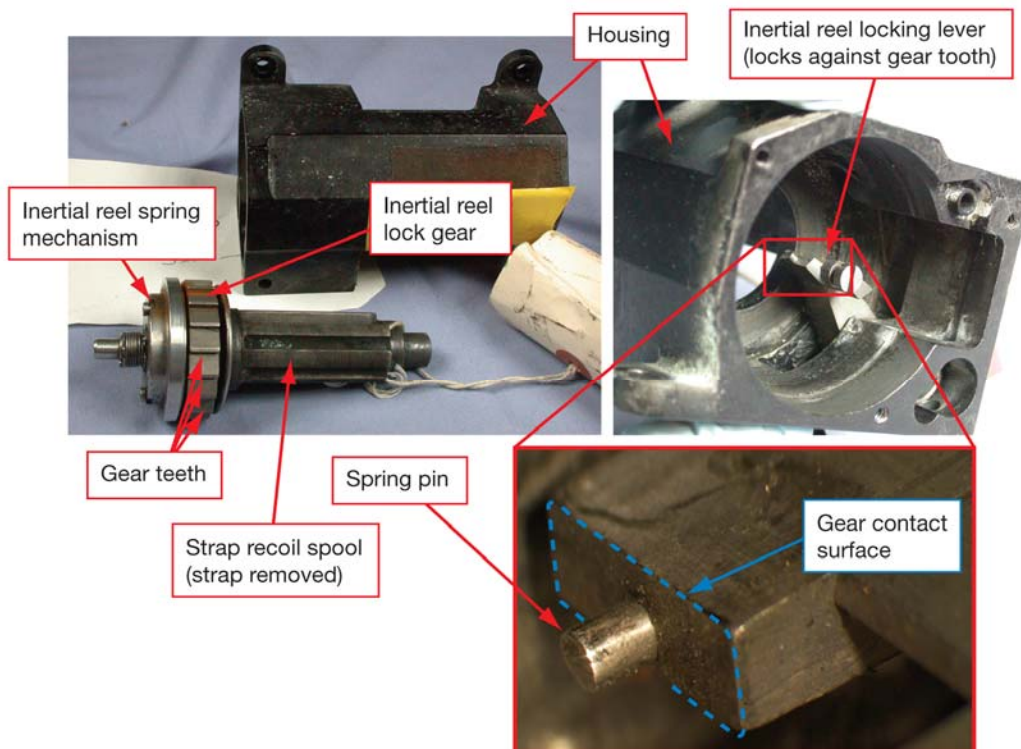
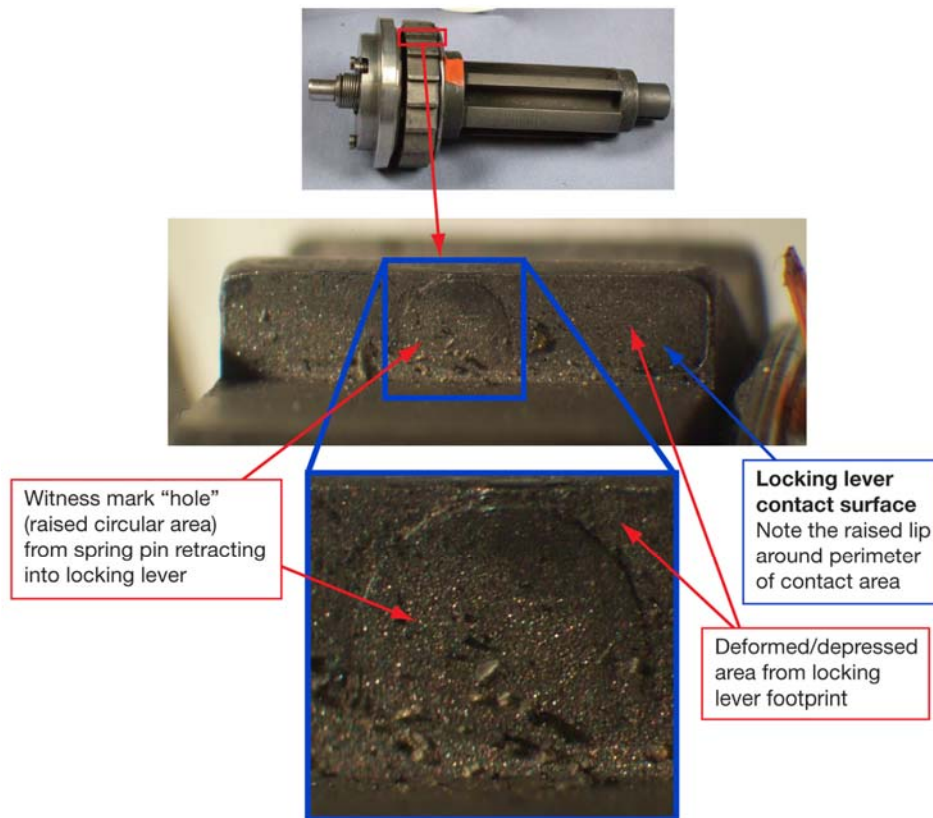


Figure 3.1-32. *Inertial reel mechanism.*

The shuttle inertial reel can be locked manually; it also has an auto-locking feature that will lock with a strap acceleration of 1.78 G to 2 G (accelerations pulling the strap out at ~57 to 64 ft/sec<sup>2</sup>). The automatic lock functions when the inertial reel spring mechanism engages the inertial reel locking lever against the corresponding inertial reel locking gear tooth surface. The strap is prevented from further extension, although recoil is possible. A spring pin is in the center of the locking lever contact surface.

All six of the recovered inertial reel mechanism gears and locking levers were inspected under stereomicroscope for evidence of mechanical loading, impact, adhesive wear, cracking, and plastic deformation. The results were consistent in all cases: the gear contact surface of the inertial reel locking lever showed no obvious witness marks; and only one tooth on *each* of the six mechanisms on the inertial reel locking gear showed evidence of witness marks (figure 3.1-33).



**Figure 3.1-33. Inertial reel locking gear witness mark.**

The witness marks can be explained by a significant loading event causing force translation through the functional strap restraint system and the inertial reel locking lever, and finally to the corresponding locking gear tooth surface. This force caused plastic deformation of the locking gear tooth, embossing the locking lever contact area on the gear tooth surface. The raised lip around the perimeter of the contact surface (figure 3.1-33) represents the outer edge of the locking lever contact area. The raised circular feature seen in this figure is caused by the spring pin retracting into the locking lever (below the contact surface of the locking lever). This feature is an area where the locking gear is *not* deformed by the locking lever.

It was initially thought that the witness marks were an indication of inertial reel strap loading during the accident. However, extensive investigation of inertial reels from training seats and other flown shuttle seats as well as a new inertial reel revealed identical circular witness marks (figure 3.1-34).

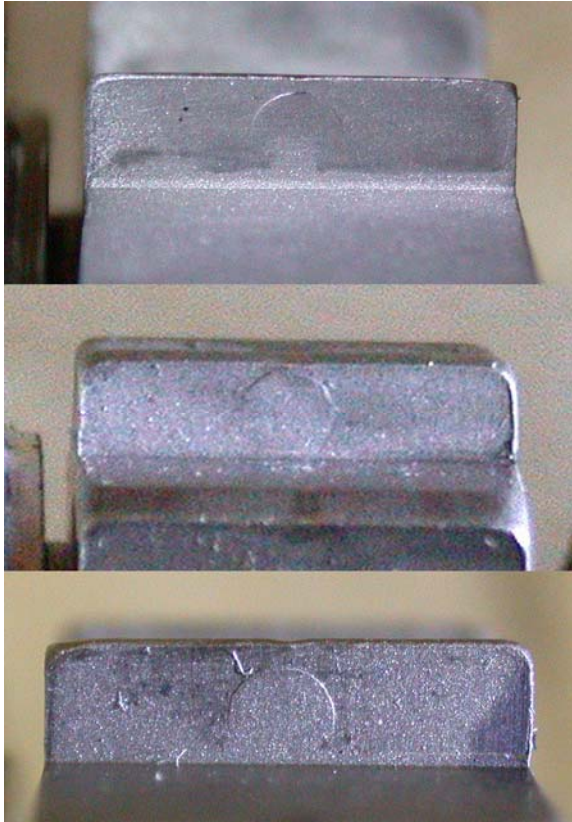


Figure 3.1-34. Circular witness marks on inertial reels from a training seat (top), a flight (non-Columbia) seat (middle), and a new (unused) flight-qualified inertial reel (bottom).

All inertial reels/straps of this type are proof-tested by the manufacturer with a 3,350-lb. static load prior to delivery to the customer. Because these inertial reels (and the *Columbia* inertial reels) were proof-tested, the investigation concluded that the witness marks on all of the inertial reels are a result of proof-testing. The absence of a second witness mark on the inertial reel led to the conclusion that the inertial reel straps failed at forces below the equivalent of a 3,350-lb. static load. However, it is probable that the straps failed under dynamic loading. As discussed above, the straps' load-carrying capabilities under dynamic loading are unknown.

A relatively large gap was discovered between the inertial locking mechanism and the lock gear on the seat 4 inertial reel (figure 3.1-35).



Figure 3.1-35. Separation gap on the seat 4 inertial reel.

Upon further inspection, it was noted that the locking mechanism had permanently “jumped” out of the normal track position, creating a gap between the inertial mechanism and the locking gear. Because this configuration would not function nominally, it is concluded that this “jump” occurred during the accident.

The observed gap between the inertial reel locking mechanism and the locking gear on seat 4 is consistent with information in the manufacturer’s experience base and occurs in crash events resulting in accelerations above 100 G at the strap input. However, the inertial reel locking mechanism can also be moved away from the locking gear by an impact along the axis of the inertial reel spool. Therefore, the observed failure (and resulting gap) could have been caused by impacts during the breakup dynamics, ground impact, or actual loads on the inertial reel strap. Because the cause of failure cannot be determined positively, no conclusions are possible regarding seat 4 inertial reel strap loads/accelerations.

### 3.1.7 Belt adjusters

Each seat restraint system includes five seatbelt adjusters (figure 3.1-36). Four of the seatbelt adjusters (out of the 35 that were on *Columbia*) were recovered. All of the belts are the same width and all of the adjusters are identical, so determination of the origin (which seat or which belt) was not possible. The findings are described below.

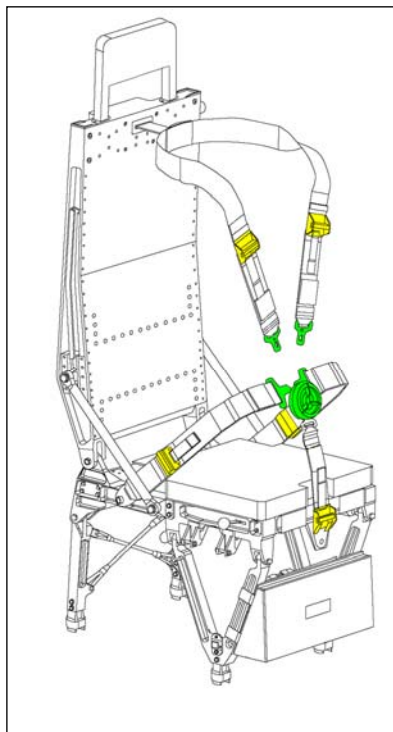


**Figure 3.1-36. Seat belt adjusters (yellow) and restraint buckle (green).** [Adapted from the Space Shuttle Systems Handbook]

The belt adjusters exhibited evidence of exposure to material deposition and heating. Molten metal debris impacts were observed in varying degrees (with no apparent directionality). Miniscule amounts of residual melted nylon belt material were observed on the adjusters.

Three of the four adjusters exhibited witness marks within the slider bar slot surface (figure 3.1-37). Tension on the belt will cause the slider bar to contact the slider bar slot as the bar rotates and slides within the slot. The witness marks in the adjusters are a result of significant loading on an intact restraint belt.

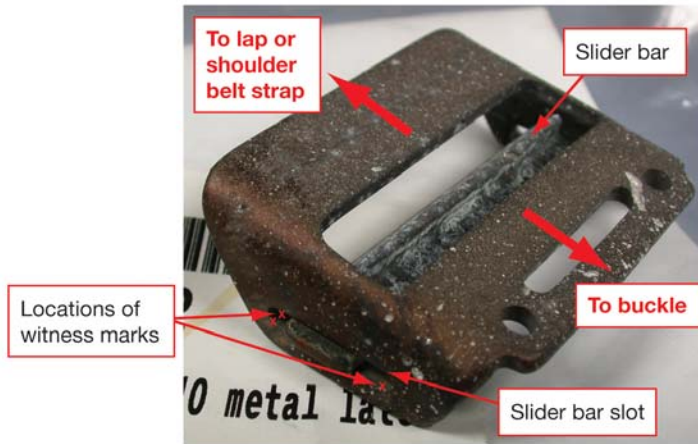


Figure 3.1-37. Recovered belt adjuster rear view.

The fourth adjuster was missing the slider bar, and experienced fractures on both the left and the right slider bar slots. These fractures were apparently caused by the slider bar “blowing out” away from the body surface (figure 3.1-38).

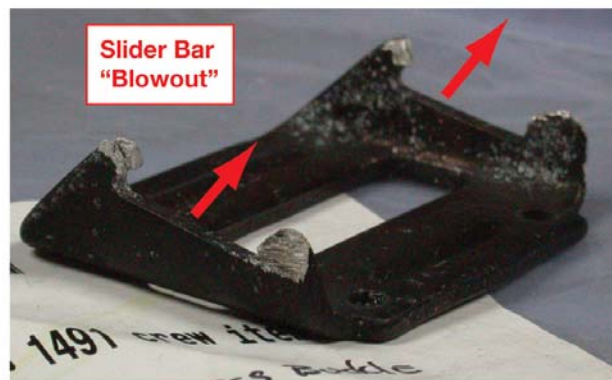


Figure 3.1-38. Fractured belt adjuster.

The fracture surfaces exhibited delamination fractures (the “broom-straw” fractures described in section 3.1.3), indicating material property degradation due to elevated temperature exposure combined with high strain rate loading. The heating occurred quickly and allowed material degradation of the metallic belt adjuster to occur without compromising the material properties of the nylon restraint belt to the point that the belt could not transmit forces to the adjuster.

The slider bar “blowout” on one of the four strap adjusters was the result of significant loading on an intact restraint belt. It cannot be determined positively when this strap adjuster failure occurred.

The witness marks and the slider bar “blowout” fracture are indicative of significant loading events causing force translation through the intact belt restraint system, resulting in the impact of the slider bar against the corresponding slot surface within the belt adjuster housing.

### 3.1.8 Restraint buckle (figures 3.1-36 and 3.1-39)

One of the seven 5-point seatbelt buckles on board *Columbia* was recovered (figure 3.1-40). Positive identification to a seat position was not possible. Although the buckle experienced significant entry heating, resulting in substantial melting of the outer plastic housing, the structure remained intact with all five belt tongues still in place.



Figure 3.1-39. *Demonstration of the five-point seatbelt buckle.*

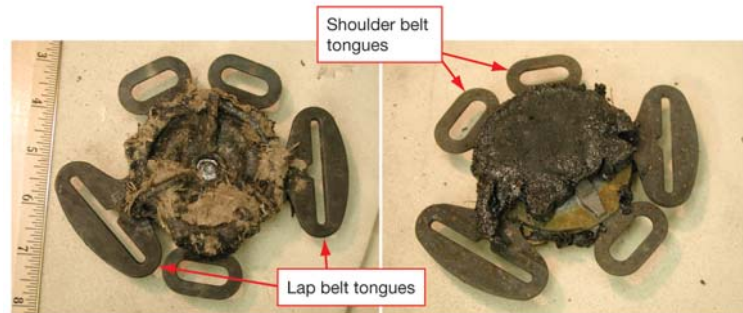


Figure 3.1-40. *Recovered five-point seatbelt buckle (front and back).*

The buckle assembly was disassembled for analysis. The two shoulder belt tongues and the two lap belt tongues were bent outward slightly (i.e., away from the crew member). Both of the shoulder belt tongue latching pins had very shallow linear features corresponding to the mating surfaces of the belt tongue (figure 3.1-41). These features may be witness marks as a result of dynamic loading events that were experienced in flight by the restraint system or of forces imparted to the five-point attach buckle during disassembly by the CAIB investigation team. A definitive conclusion cannot be made based on these witness marks alone. The other latching pins did not exhibit any noticeable marks or deformations.

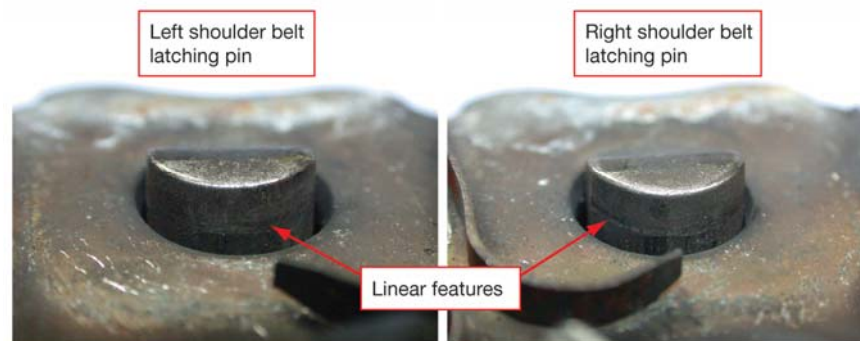


Figure 3.1-41. *Indentations on latching pins, looking from center of buckle towards outer edge.*

Shadowing<sup>14</sup> on the belt tongues indicates that the belt tongues were in the position shown in figure 3.1-42(b). These positions, when compared to the positions of the tongues being straight out from center of buckle (radially, figure 3.1-42(a)), are: the shoulder belt tongues are moved toward the centerline (medially), the crotch belt tongue is moved toward the right side of the seat, and the lap belt tongues are moved down. It cannot be determined positively when the deposition (and shadowing) occurred, so no conclusions can be made relative to timing.



**Figure 3.1-42. Belt tongue positions.**

Because all of the seats use a common seat restraint design, none of these pieces could be positively identified as being from a specific seat. This means that the belt adjusters and the restraint buckle could be from any of the seven seats on *Columbia*. It is even possible that the items were from the same seat. However, because the items vary in condition (different amounts of heating and debris impacts) and were found in widely spread locations (> a 14-mile spread), it is unlikely that these items originated from the same seat.

Significant forces caused witness marks on the seat restraint buckle tongues and the belt adjusters. Witness marks on the belt adjusters were caused by force transmission through intact functional belts. In the case of the fractured belt adjuster, forces on the belt were sufficient to cause the adjuster slider bar to “rupture” out of the slot. Fracture surfaces indicate that this rupture occurred at an elevated temperature. However, the heating occurred quickly, allowing material property degradation of the metallic belt adjuster without compromising material properties of the nylon restraint belt to the point that the belt could not transmit forces to the adjuster.

<sup>14</sup>An area that lacks or has less material deposition when compared to an adjacent area. Shadowing indicates that another item covered the shadowed area, preventing deposition.

### 3.1.9 Sequence

From the evidence and conclusions described above, the SCSIIT was able to develop the following sequence of events related to the seats:

- All of the seats were installed.
- Crew members were at least partially strapped into seats 1, 2, 3, 4, 6, and 7.
- During vehicle loss of control (LOC), the dynamics caused the crew members to be pulled forward and/or side-to-side. If the component of the acceleration pulling the inertial reel out of the seat (forward) was less than 1.78 G to 2 G, the inertial reels would *not* lock and the straps could be going in and out as the loads vary in magnitude and direction.
- Cabin breach and depressurization occurred.
- During the period of material deposition (when the cabin was depressurized and molten metal globules were floating around in the vicinity of the seats), the inertial reel straps were extended (the crew members were still in their seats) and the straps received molten material deposits.
- The inertial reel straps failed (predominantly due to mechanical overload, but below the equivalent of a 3,350-lb. static load) and the straps retracted into the seatbacks.
- The remaining shoulder harness belts and crotch and lap belts eventually melted/burned away.
- The seats experienced heating and high strain rates, and broke up due to thermal and then mechanical effects.

### 3.1.10 Lesson learned – equipment serialization and marking

One of the most useful tools in investigating an aviation accident is reconstructing the vehicle, either physically or virtually, from the recovered debris. Being able to identify the original location within the vehicle of debris items is of utmost importance in achieving an accurate reconstruction. Identifying the origins of debris items is made possible by serializing individual piece parts and subassemblies, and keeping accurate records of the piece part/subassembly serial numbers at the assembly and, ultimately, the vehicle level. This is especially useful when there are multiple units of identical or similar components, such as crew equipment, seats, engines, or structural members.

As discussed above, there are two different types of seats – Pilot seats, which are used by the CDR and the PLT, and Mission Specialists seats. The main difference between these types of seats is the design of the seat pan and the legs. The seatbacks and seat restraints are identical in design and construction for both types of seat. When the seats were manufactured, individual seat components were ink-stamped with individual part numbers and serial numbers. Configuration management records for seat components<sup>15</sup> were not accurately maintained, however, so identifying component locations by any surviving piece-part serial number was futile. The exceptions to this were the components associated with the inertial reels; all six recovered upper seatbacks were identified to specific seat locations.

Initially in the *Columbia* investigation, the only seat debris pieces that could be positively identified to a specific seat location were the upper seatbacks, which contain the inertial reels, and any pieces that remained attached to identifiable floor pieces. For the remaining seat debris items, reconstruction and location identification was a time-consuming, laborious process of matching pieces with the upper seatbacks and those pieces that were attached to floor panels. Eventually, 31 pieces of seat structure debris were positively identified to specific seat locations. However, almost 60 pieces of seat structure debris remained unidentified along with numerous fragments of seat soft goods. Had the individual seat components been permanently marked with serial numbers and those serial numbers tracked to the assembled seats, reconstruction and identification would have been much easier and a higher percentage of pieces could have been identified to

<sup>15</sup>Tracking the serial numbers for seat components to the top-level seat assembly's serial number.

specific seats. Therefore, space flight programs should develop failure investigation marking (“fingerprinting”) requirements and policies. Equipment fingerprinting requires three aspects to be effective: component serialization, marking, and tracking to the assembly level. Marking by electronic means, metal stamping, or etching is preferable to labels or ink stamping because labels and ink stamps are not as durable in catastrophic failure scenarios. Marking in multiple locations, and on as many piece-parts in a major assembly as practical, is recommended.

**Finding.** While all seat piece-parts include serial numbers, only the serial numbers of the inertial reels were recorded and tracked to a specific seat assembly. The lack of configuration management documentation hindered the process of ascribing the seat debris items to specific seat locations.

**Recommendation A5.** Develop equipment failure investigation marking (“fingerprinting”) requirements and policies for space flight programs. Equipment fingerprinting requires three aspects to be effective: component serialization, marking, and tracking to the lowest assembly level practical.

## 3.2 Crew Worn Equipment

Because the crew worn equipment is the hardware that is closest to the crew members, it provides a source of data for the mechanical and thermal environments that the crew members experienced. This section provides background information on crew worn equipment and describes its configuration on STS-107. A brief review of the different types of shuttle suits is presented. Crew worn equipment, which includes the advanced crew escape suit (ACES), the personal parachute assembly (PPA), and the parachute harness, is described. The *Columbia* crew worn configuration is addressed. In addition, some aircraft in-flight breakup case studies are also considered to draw parallels between those mishaps and that of *Columbia*. Finally, *Columbia*-specific topics are addressed: the general, thermal, and mechanical conditions of the helmets and suit neck rings; the glove disconnects; the dual suit controllers (DSCs); the boots; the Emergency Oxygen System (EOS); the Seawater Activated Release System (SEAWARS); the Telonics Satellite Uplink Beacon-A (TSUB-A) search and rescue satellite-aided tracking (SARSAT) beacon; the Army/Navy personal radio communications (A/N PRC)-112 radio; and the ground plot analysis.

The following is a summary of findings, conclusions, and recommendations from this section.

**Finding.** The current ACES was added after the shuttle cockpit was designed and built. In many cases, the operations that the crew must perform are difficult to perform while wearing the suit. Some crew members choose between not wearing portions of the suit (gloves) to perform nominal tasks efficiently, or wearing their gloves to protect against off-nominal atmospheric situations at the expense of nominal operations or other off-nominal situation responses needing more dexterity.

**Finding.** Breathing 100% O<sub>2</sub> results in O<sub>2</sub>-enriched air being exhaled into the shuttle cabin. Over time, this increases the O<sub>2</sub> concentration in the cabin, amplifying the potential for fire. Therefore, the amount of time that crew members have their visors down and are breathing 100% O<sub>2</sub> is limited operationally to reduce this hazard.

**Finding.** One crew member did not have the helmet donned at the time of the Crew Module Catastrophic Event (CMCE). Three of the seven crew members did not complete glove donning for entry. The deorbit preparation period of shuttle missions is so busy that crew members frequently do not have enough time to complete the deorbit preparation tasks (suit donning, seat ingress, strap-in, etc.) prior to the deorbit burn.

**Recommendation L1-2.** Future spacecraft and crew survival systems should be designed such that the equipment and procedures provided to protect the crew in emergency situations are compatible with nominal operations. Future spacecraft vehicles, equipment, and mission timelines should be designed such that a suited crew member can perform all operations without compromising the configuration of the survival suit during critical phases of flight.

**Finding.** Inspection of all seven recovered helmets confirmed that none of the crew members lowered and locked their visors.

**Conclusion L5-1.** The current parachute system requires manual action by a crew member to activate the opening sequence.

**Recommendation L1-3/L5-1.** Future spacecraft crew survival systems should not rely on manual activation to protect the crew.

**Conclusion L4-1.** Although the advanced crew escape suit (ACES) system is certified to operate at a maximum altitude of 100,000 feet and to survive exposure to a maximum velocity of 560 knots equivalent air speed, the actual maximum protection environment for the ACES is not known.

**Recommendation L3-5/L4-1.** Evaluate crew survival suits as an integrated system that includes boots, helmet, and other elements to determine the weak points, such as thermal, pressure, windblast, or chemical exposure. Once identified, alternatives should be explored to strengthen the weak areas. Materials with low resistance to chemicals, heat, and flames should not be used on equipment that is intended to protect the wearer from such hostile environments.

**Finding.** The current ACES helmets are nonconformal and do not provide adequate head protection or neck restraint for dynamic loading situations.

**Recommendation L2-4/L3-4.** Future spacecraft suits and seat restraints should use state-of-the-art technology in an integrated solution to minimize crew injury and maximize crew survival in off-nominal acceleration environments.

**Recommendation L2-7.** Design suit helmets with head protection as a functional requirement, not just as a portion of the pressure garment. Suits should incorporate conformal helmets with head and neck restraint devices, similar to helmet/head restraint techniques used in professional automobile racing.

**Finding.** Most of the suit components and subcomponents include serial numbers that are recorded and tracked to a specific crew member. This configuration management documentation aided greatly in the process of ascribing the debris items to specific crew members.

**Recommendation A5.** Develop equipment failure investigation marking (“fingerprinting”) requirements and policies for space flight programs. Equipment fingerprinting requires three aspects to be effective: component serialization, marking, and tracking to the lowest assembly level practical.

**Finding.** The ACES had no performance requirements for occupant protection from elevated temperatures or fire. The ensemble includes nylon on the parachute harness straps and the boots. The ACES may not provide adequate protection to crew members in emergency egress scenarios involving exposure to heat and flames.

**Recommendation L3-5/L4-1.** Evaluate crew survival suits as an integrated system that includes boots, helmet, and other elements to determine the weak points, such as thermal, pressure, windblast, or chemical exposure. Once identified, alternatives should be explored to strengthen the weak areas. Materials with low resistance to chemicals, heat, and flames should not be used on equipment that is intended to protect the wearer from such hostile environments.

Crew escape equipment (CEE) enhances the crew members’ capability to escape safely from a disabled orbiter on the launch pad, in atmospheric flight, or following landing.<sup>1</sup> This equipment includes the crew worn equipment and the crew escape pole.<sup>2</sup> For in-flight bailout scenarios, the CEE is designed for use during controlled subsonic gliding flight conditions.

---

<sup>1</sup>Program Requirements Document for Crew Escape Equipment, NSTS-22377, Revision B, October 1994.

<sup>2</sup>The crew escape pole is discussed in Section 2.4.

### 3.2.1 Shuttle suits

The shuttle was originally designed to be operated in a shirtsleeve (bare-hands) environment for all phases of flight, including launch and landing. The U.S. Air Force SR-71 pressure suit was worn for the first four shuttle missions (STS-1 through STS-4), which were considered test flights. Following these first four missions, the shuttle was declared fully operational and shuttle crews wore standard flight suits (light-weight fabric coveralls) with a helmet and a portable air supply that was intended principally for ground egress and cabin smoke protection. After the *Challenger* accident in January 1986, NASA started to use the launch and entry suit, beginning with STS-26 in 1988, and later phased in the more capable ACES beginning in 1994. This addition of pressure suits to a vehicle that was designed for shirtsleeve operations resulted in human/machine interface incompatibilities, especially with switches and other hand-operated controls. Because of this, some crew members decide between wearing gloves for full protection in emergency scenarios or not wearing gloves to be able to perform nominal tasks (keyboard entries, manipulating displays and controls, etc.) efficiently.

**Finding.** The current ACES was added after the shuttle cockpit was designed and built. In many cases, the operations that the crew must perform are difficult to perform while wearing the suit. Some crew members choose between not wearing portions of the suit (gloves) to perform nominal tasks efficiently, or wearing their gloves to protect against off-nominal atmospheric situations at the expense of nominal operations or other off-nominal situation responses needing more dexterity.

**Recommendation L1-2.** Future spacecraft and crew survival systems should be designed such that the equipment and procedures provided to protect the crew in emergency situations are compatible with nominal operations. Future spacecraft vehicles, equipment, and mission timelines should be designed such that a suited crew member can perform all operations without compromising the configuration of the survival suit during critical phases of flight.

Crew worn equipment (figure 3.2-1), which is used by shuttle crew members during launch and entry, provides the necessary protection and survival equipment to sustain the crew below 100,000 feet and ensures

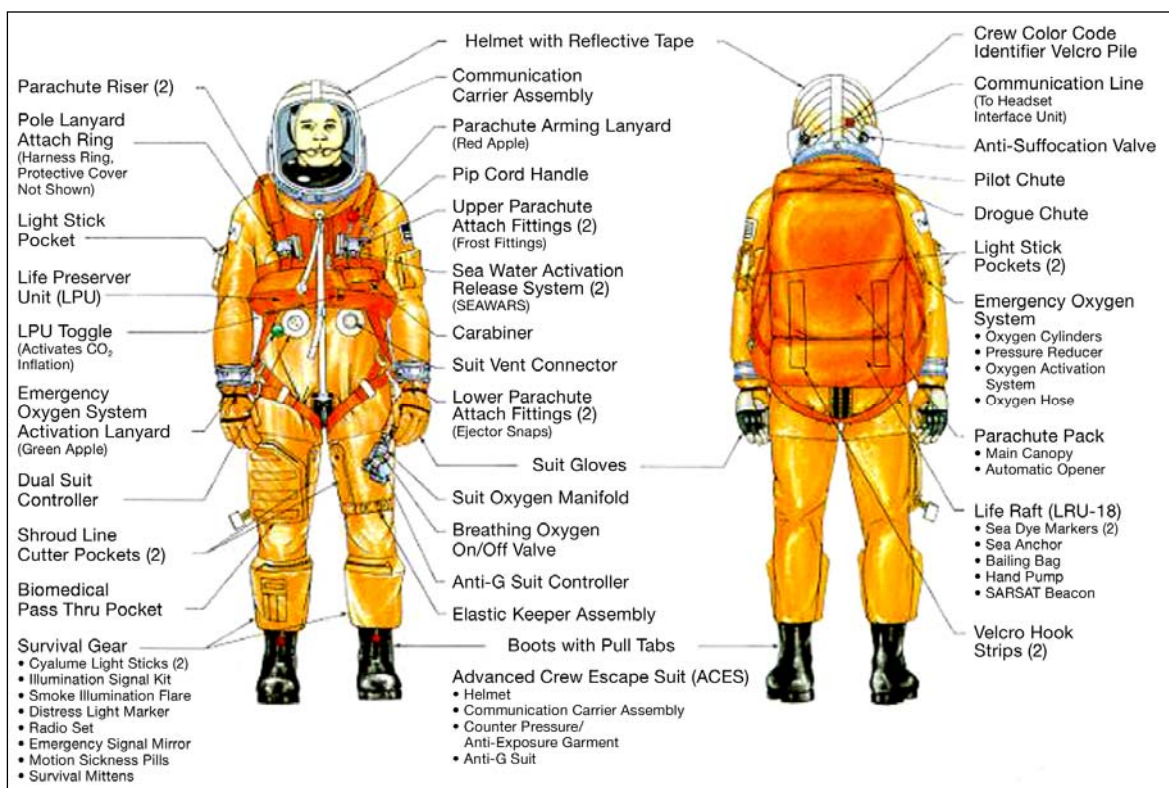


Figure 3.2-1. Crew worn equipment: advanced crew escape suit, harness, parachute, and survival gear.